

AD-A155 730

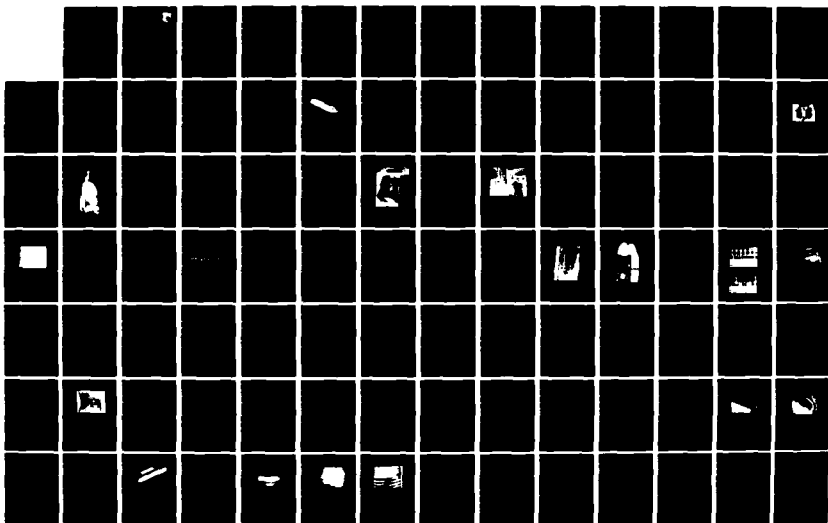
STRIATION FREE DOPED SILICON(U) HUGHES RESEARCH LABS
MALIBU CA G D ROBERTSON DEC 84 AFMAL-TR-84-4156
F33615-81-C-5065

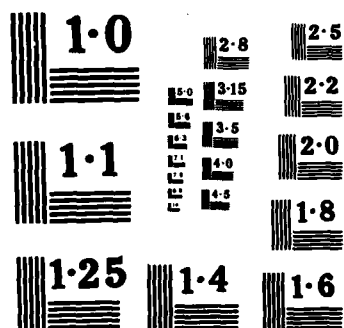
172

UNCLASSIFIED

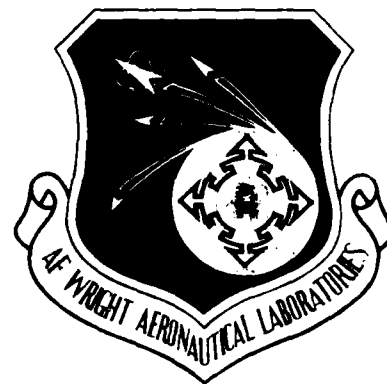
F/G 20/2

NL





NATIONAL BUREAU OF STANDARDS
MICROCOPY RESOLUTION TEST CHART



STRIATION FREE DOPED SILICON

G.D. Robertson

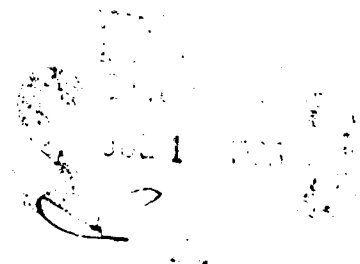
Hughes Research Laboratories
3011 Malibu Canyon Road
Malibu, CA 90265

December 1984

Final Report for Period September 1981 through September 1984

Approved for public release; distribution unlimited

MATERIALS LABORATORY
AIR FORCE WRIGHT AERONAUTICAL LABORATORIES
AIR FORCE SYSTEMS COMMAND
WRIGHT-PATTERSON AIR FORCE BASE, OH 45433



AD-A155 730

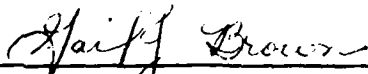
DTIC FILE COPY

NOTICE

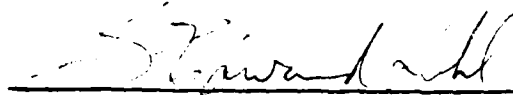
When Government drawings, specifications, or other data are used for any purpose other than in connection with a definitely related Government procurement operation, the United States Government thereby incurs no responsibility nor any obligation whatsoever; and the fact that the government may have formulated, furnished, or in any way supplied the said drawings, specifications, or other data, is not to be regarded by implication or otherwise as in any manner licensing the holder or any other person or corporation, or conveying any rights or permission to manufacture use, or sell any patented invention that may in any way be related thereto.

This report has been reviewed by the Office of Public Affairs (ASD/PA) and is releasable to the National Technical Information Service (NTIS). At NTIS, it will be available to the general public, including foreign nations.

This technical report has been reviewed and is approved for publication.



GAIL J. BROWN
Project Monitor
Laser & Optical Materials Branch



G. EDWARD KUHL, Chief
Laser & Optical Materials Branch
Electromagnetic Materials Division

FOR THE COMMANDER



MERRILL L. MINGES, Chief
Electromagnetic Materials Division
Materials Laboratory

"If your address has changed, if you wish to be removed from our mailing list, or if the addressee is no longer employed by your organization please notify AFMAL/MLPO, W-PAFB, OH 45433 to help us maintain a current mailing list".

Copies of this report should not be returned unless return is required by security considerations, contractual obligations, or notice on a specific document.

UNCLASSIFIED

AD-A155730

SECURITY CLASSIFICATION OF THIS PAGE

REPORT DOCUMENTATION PAGE

1a. REPORT SECURITY CLASSIFICATION UNCLASSIFIED			1b. RESTRICTIVE MARKINGS NONE		
2a. SECURITY CLASSIFICATION AUTHORITY			3. DISTRIBUTION/AVAILABILITY OF REPORT Approval for public release; distribution unlimited.		
2b. DECLASSIFICATION/DOWNGRADING SCHEDULE					
4. PERFORMING ORGANIZATION REPORT NUMBER(S)			5. MONITORING ORGANIZATION REPORT NUMBER(S) AFWAL-TR-84-4156		
6a. NAME OF PERFORMING ORGANIZATION Hughes Aircraft Company, Research Laboratories Division		6b. OFFICE SYMBOL (If applicable)	7a. NAME OF MONITORING ORGANIZATION Air Force Wright Aeronautical Laboratories Materials Laboratory		
6c. ADDRESS (City, State and ZIP Code) 3011 Malibu Canyon Road Malibu, CA 90265		7b. ADDRESS (City, State and ZIP Code) Air Force Systems Command Wright-Patterson AFB, OH 45433			
8a. NAME OF FUNDING/SPONSORING ORGANIZATION Air Force Wright Aeronautical Laboratories, Materials Laboratory		8b. OFFICE SYMBOL (If applicable) AFWAL/MLPO	9. PROCUREMENT INSTRUMENT IDENTIFICATION NUMBER F33615-81-C-5065		
8c. ADDRESS (City, State and ZIP Code) Wright-Patterson AFB, Ohio 45433		10. SOURCE OF FUNDING NOS.			
		PROGRAM ELEMENT NO.	PROJECT NO.	TASK NO.	WORK UNIT NO.
			2423	02	18
11. TITLE (Include Security Classification) Striation Free Doped Silicon					
12. PERSONAL AUTHOR(S) G. Robertson					
13a. TYPE OF REPORT Final Report		13b. TIME COVERED FROM 9-81 to 9-84	14. DATE OF REPORT (Yr., Mo., Day) December 1984		15. PAGE COUNT 153
16. SUPPLEMENTARY NOTATION					
17. COSATI CODES			18. SUBJECT TERMS (Continue on reverse if necessary and identify by block number)		
FIELD	GROUP	SUB. GR.			
			Silicon Crystals		
			Si:Ga		
			Magnetic Field Effects		
19. ABSTRACT (Continue on reverse if necessary and identify by block number) The growth of float zone doped silicon crystals in the presence of strong magnetic fields has been investigated. Fields of 5000 G, oriented both transverse to and along the growth axis, have produced dopant distributions in Ga-doped Si that have not been observed previously. Reductions of dopant concentration fluctuations by factors of three have been seen for strong axial fields. In the transverse fields, the dopant distributions are quite different from those obtained in normal growth, but the fluctuations are not appreciably reduced. However, the growth of crystals without rotation is stabilized by the transverse field and this stabilization makes possible the study of fine striae in the absence of rotational striae. Such studies promise to provide insight into the physics of the float zone process. On the other hand, the axial field appears to destabilize growth, especially at low rotation rates. Further work with the					
20. DISTRIBUTION/AVAILABILITY OF ABSTRACT UNCLASSIFIED/UNLIMITED <input checked="" type="checkbox"/> SAME AS RPT <input type="checkbox"/> DTIC USERS <input type="checkbox"/>			21. ABSTRACT SECURITY CLASSIFICATION UNCLASSIFIED		
22a. NAME OF RESPONSIBLE INDIVIDUAL Gail J. Brown		22b. TELEPHONE NUMBER (Include Area Code) (513) 255-4474	22c. OFFICE SYMBOL AFWAL/MLPO		

DD FORM 1473, 83 APR

EDITION OF 1 JAN 73 IS OBSOLETE.

UNCLASSIFIED

SECURITY CLASSIFICATION OF THIS PAGE

UNCLASSIFIED

SECURITY CLASSIFICATION OF THIS PAGE

19 ABSTRACT

axial field is needed to develop growth techniques which will allow us to capitalize on the uniform dopant distributions that it provides.

UNCLASSIFIED

SECURITY CLASSIFICATION OF THIS PAGE

PREFACE

This technical report was prepared by Glenn D. Robertson of the Chemical Physics Department of Hughes Research Laboratories. Key participants in the technical effort included Dennis J. O'Connor, Harold M. Olsen, Hiroshi Kimura, Robert Baron, James K. Neeland, George C. Valley, and Ogden J. Marsh. The work was initiated under Project No. FY1457-81-03052 by the Materials Laboratory of the Air Force Systems Command (AFWAL/MLPO). The Project Engineer was originally Capt. Richard Gassman, who was succeeded about midway in the program by Ms. Gail J. Brown.

The work was conducted at Hughes Research Laboratories, Malibu, CA during the period from 1 September 1981 to 1 September 1984.

The encouragement and support of Drs. Melvin Ohmer, Gordon Griffith, and Patrick Hemenger of the Materials Laboratory during this time was greatly appreciated.



A-1

TABLE OF CONTENTS

SECTION		PAGE
	SUMMARY.....	1
I	INTRODUCTION.....	9
II	BACKGROUND INFORMATION.....	13
III	EXPERIMENTAL PROCEDURES.....	15
	A. Float Zone Growth with a Magnetic Field.....	15
	B. Crystal Evaluation Techniques.....	27
IV	DISCUSSION OF EXPERIMENTAL RESULTS.....	37
	A. Rotating Crystals in a Transverse Field.....	39
	B. Non-Rotating Crystals in a Transverse Field..	74
	C. Crystals Grown in an Axial Field.....	97
V	CONCLUSIONS.....	121
VI	RECOMMENDATIONS FOR FUTURE WORK.....	123
	REFERENCES.....	127
APPENDICES		
A	MAGNETIC FIELD INTERACTIONS.....	A-1
B	DATA PROCESSING PROCEDURES.....	B-1

LIST OF ILLUSTRATIONS

FIGURE		PAGE
1	Spreading resistance for crystals prepared with various growth conditions.....	3
2	Radial spreading resistance scans for crystals grown in an axial field.....	5
3	Morphology of crystal Z321 grown without rotation in a 5500 G transverse field.....	6
4	Electromagnet mounted in the float-zone furnace.....	16
5	Photograph of tilted solenoid magnet.....	18
6	Growth region in tilted solenoid magnet.....	19
7	Field configuration for tilted solenoid magnet...	20
8	Modified float zone furnace with 5 kG magnet in transverse field configuration.....	23
9	Calibration curve for transverse field magnet....	24
10	External magnet in the axial field configuration.	25
11	Calibration curve for axial field configuration..	26
12	Spreading resistance data for crystal Z285.....	29
13	Original spreading resistance data plot for the 2000 to 0 gauss transition in crystal Z285 seen in Figure 12.....	30
14	Striation etch pattern for the region of crystal Z285 in which the field was removed, see Figure 12.....	31
15	Power spectral densities for crystal Z285.....	32
16	Spreading resistance data for the non-rotating section of crystal Z292.....	34
17	Power spectral densities for the non-rotating section of crystal Z292.....	35

FIGURE		PAGE
18	Matrix of growth conditions explored with early magnets.....	38
19	Striation etch pattern for the 6 rpm section of crystal Z309, grown in a 5000 gauss transverse magnetic field.....	41
20	Striation etch pattern for the 12 rpm section of crystal Z309 grown in a 5000 gauss transverse magnetic field.....	42
21	Diameter changes for crystal Z323 at 13 rpm.....	44
22	Striation etch pattern for crystal Z323 in the region where the magnet was ON for 30 sec and OFF for 30 sec.....	45
23	Spreading resistance data for the 12 rpm section of crystal Z309.....	53
24	Power spectral densities for magnet-on and -off regions of the 12 rpm section of the 12 rpm section of crystal Z309.....	54
25	Spreading resistance data for the 6 rpm section of crystal Z309.....	55
26	Power spectral densities for the magnet-on and -off regions of the 6 rpm section of crystal Z309.....	56
27	Spreading resistance data for the 3 rpm section of crystal Z316.....	57
28	Power spectral densities of the magnet-on and -off regions of the 3 rpm section of crystal Z316.....	58
29	Spreading resistance for the 6 rpm section of crystal Z328 <111>.....	59
30	Power spectral densities for the magnet-on and -off regions of the 6 rpm section of crystal Z328 <111>.....	60
31	Striation etch pattern of the 6 rpm section of crystal Z328 <111> from which the data of Figure 29 and 30 were obtained.....	61
32	High frequency range of power spectral densities for the 12 rpm section of crystal Z309.....	64

FIGURE		PAGE
33	High frequency range of power spectral densities for the 6 rpm section of crystal Z309.....	65
34	High frequency range of power spectral densities for the 3 rpm section of crystal Z316.....	66
35	Spreading resistance data from on-axis scans of the 6 rpm section of crystal Z309.....	67
36	Power spectral densities for on-axis scans of the 6 rpm section of crystal Z309.....	68
37	High frequency range of the power spectral densities of the on-axis scans in the 6 rpm section of crystal Z309.....	69
38	High frequency range of the power spectral densities of the on-axis scans in the 6 rpm region of crystal Z328 <111>.....	70
39	Striation etch pattern on an end surface from the 4 rpm section of crystal Z319, grown with the magnet off.....	72
40	Striation etch pattern on an end surface of the 4 rpm section for crystal Z319 grown in a 3100 G transverse field.....	73
41	Crystal Z322 grown with no rotation in a 5500 G transverse field.....	76
42	Striation etch pattern for non-rotating section of crystal Z322 showing the transition from 0 to 5500 gauss at 0 rpm.....	78
43	Striation etch pattern of the 90-degree rotation for crystal Z322 grown at 5500 G without rotation.....	79
44	Striation etch pattern at the 90-degree rotation for crystal Z328 <111> grown at 5500 G without rotation.....	80
45	Striation etch pattern for non-rotating section of crystal Z322 grown with magnet off.....	82
46	Striation etch pattern for non-rotating section of crystal Z322 grown in a 5500 G transverse field.....	83
47	Spreading resistance data for various regions of crystal Z322.....	84

FIGURE		PAGE
48	Power spectral densities for the non-rotating section of crystal Z322, low frequency range.....	85
49	Power spectral densities for the non-rotating section of crystal Z322, high frequency range....	86
50	Striation etch pattern of an end surface from a non-rotating section of crystal Z322 grown with a 5500 G transverse field.....	88
51	Spreading resistance data for the non-rotating section of crystal Z322 for different feed rod rotations.....	89
52	Power spectral densities for the non-rotating section of crystal Z322 with different feed rod rotations.....	91
53	Spreading resistance data along the axis of the non-rotating section of crystal Z322 for different feed rod rotations.....	92
54	Low frequency range power spectral density for the on-axis scan of crystal Z322 for different feed rod rotations.....	93
55	High frequency range of power spectral densities for the on-axis scan of crystal Z322 for different feed rod rotations.....	94
56	Spreading resistance across the diameter of crystal sections grown at 12 rpm with different axial field strengths.....	99
57	Radial spreading resistance scans for non-rotating crystals in an axial field.....	100
58	Striation etch pattern for the 12 rpm sections of crystal Z331.....	102
59	Striation etch pattern of the 12 rpm sections of crystals grown in an axial magnetic field.....	103
60	Striation etch pattern of the non-rotating sections of crystal Z334.....	104
61	On-axis spreading resistance fluctuations for non-rotating crystal section.....	106
62	Striation etch pattern for the 3 rpm section of crystal Z331 showing the transition from magnet off to a 3700 G axial field.....	109

FIGURE		PAGE
63	Striation etch pattern for the 3 rpm section of crystal Z332 grown in a 4000 G axial field.....	110
64	Striation etch pattern of the 3 rpm section of crystal Z333 grown in a 5000 G axial field....	111
65	Spreading resistance for on-axis scans of the 3 rpm section of crystal Z331.....	112
66	Power spectral densities for the on-axis scans of the 3 rpm section of crystal Z331.....	113
67	Spreading resistance across the diameter of a section grown at 12 rpm in a 4000 G axial field..	115
68	Spreading resistance for an on-axis scan of the 12 rpm region of crystal Z332 grown with a 4000 G axial field.....	116
69	Crystals grown in a strong axial field showing severe wandering about the growth axis.....	118

LIST OF TABLES

TABLE		PAGE
1	Growth Conditions for Crystals Grown in Strong Magnetic Fields.....	40
2	Resistance Levels and Fluctuation Intensities for Comparable Crystal Regions with Magnetic Fields On and Off.....	47
3	Processed Data for Scans Used in Table 2.....	48
4	Resistance Levels and Fluctuation In Intensities for Comparable Regions Grown With and Without a Strong Transverse Field.....	49
5	Processed Data for Scans Used in Table 4.....	51
6	Resistance and Fluctuation Level Changes for the Section of Crystal Z322.....	96
7	Fluctuation Levels for Recent Crystals.....	108

SUMMARY

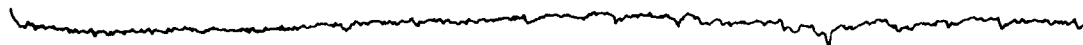
The objective of this program has been to explore a novel method for reducing the dopant concentration fluctuations in detector-grade silicon grown by float zoning. The approach employed has been the incorporation of a magnetic field into the growth process and the study of its effects on the striations produced by nonuniform doping levels. This work has extended over a three-year period, roughly divided into three phases by the availability of the magnet systems used. The first two systems fit within the growth furnace and were limited in field strength to less than 2000 G. Because the results obtained with these two systems were only suggestive of the important results that have come later, we have concentrated the discussions in this report on the findings resulting from the use of an external magnet system that produces field strengths of 5000 G. Major discoveries have been made that promise to provide a meaningful improvement in the spatial uniformity of the dopants in detector-grade silicon. In this summary we will review these new results and their implications for future activity. Experimental details can be found in Sections III and IV of this report.

The use of magnetic fields at strengths above 3000 G has produced significant effects on the character of float zone crystals. When the field is transverse to the growth axis, the striation patterns seen in the gallium-doped silicon crystals are altered in a major way. However, the fluctuations of the dopant concentration do not appear to be significantly reduced. If the field is oriented along the growth axis, then a major alteration of the flow within the melt zone occurs, with the formation of a "stagnation" region centered on the growth axis. In this region, the boundary layer appears to be considerably thickened, thus shielding the growth interface from most of the turbulence in the melt volume. The result is a "core" in which

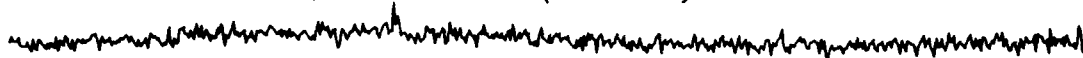
the dopant concentration in the crystal is increased considerably and fine scale fluctuations are greatly reduced. If, in addition, the crystal is not rotated during growth, the dopant concentration in the core region attains a uniformity never before observed in float zone silicon. These results with the strong axial field have occurred within the final month of the contract effort and thus have not yet been investigated to the detail necessary to define all of the important parameters contributing to the exceptional dopant uniformity.

To assess the dopant uniformity in the core region, we have used spreading resistance scans along the growth axis and also across the diameter of the crystal. Spreading resistance is the most quantitative means of characterizing dopant fluctuations; the dopant distributions displayed agree qualitatively with those revealed by the striation etch patterns formed when a polished crystal surface is given a stain etch that is sensitive to dopant concentration. Later in this report there are many examples given of these two types of characterization. Here we will show only two examples to illustrate the relative reduction in fluctuation levels produced by the strong axial field. In Figure 1 are shown several spreading resistance scans taken along the growth axis for sections of crystals grown under differing conditions. The best standard of uniformity that we have is neutron transmutation doped silicon in which the dopant is added isotropically after the crystal is grown. In addition to the scan from this "standard", we show data that represent typical fluctuation levels obtained under a variety of growth conditions, as indicated on each curve. The amplitude of the resistance fluctuations is plotted on a common logarithmic scale to permit comparison of relative magnitudes. The curves have been arbitrarily displaced vertically from one another to avoid overlap. It is apparent that the fluctuations for the core of the crystal grown with no rotation in the 5000 G field are

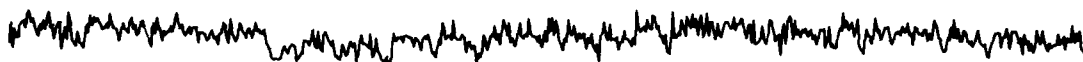
NTD STANDARD SAMPLE (SR486SP.NTD)



CORE REGION, 0 RPM, 5000 G AXIAL FIELD (SR344SP.AC1)



TYPICAL DETECTOR GRADE CRYSTAL, 12 RPM, MAGNET OFF (SR322SP.AC1)



CENTER OF CRYSTAL, 0 RPM, 5500 G TRANSVERSE FIELD (SR322SP.AC3)

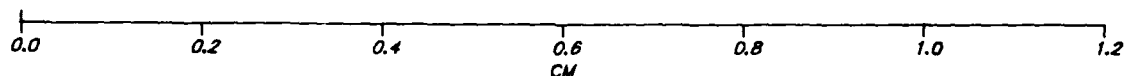


Figure 1. Spreading resistance for crystals prepared with various growth conditions. The fluctuation level for the core region of the 0 rpm, 5000 G crystal is the lowest we have ever obtained for float zone silica.

considerably lower than those of normal detector grade crystals as well as all other specimens grown in the presence of a magnetic field. Figure 2 shows spreading resistance scans taken across a diameter of some specimens that illustrate the formation of the core in the stronger axial fields. At present, the diameter of this core region is about 8 mm in a crystal with an overall diameter of 24 mm. The discovery of this uniform core in a non-rotating crystal is a finding of major importance to the eventual production of detector-grade doped silicon of superior uniformity. As the sophistication of focal plane arrays increases, the need for better material uniformity will assume even greater importance than it has now. We believe that the results of this program, if properly exploited, will lead to the exceptional uniformity needed in future detector systems.

Another discovery of potential importance to the understanding of the float zone process is the effect of a strong transverse field on the morphology of a non-rotating crystal. In normal float zone growth, the crystal must be rotated to minimize the effects of a nonsymmetric addition of energy from the asymmetric rf heating field. This rotation results in a growth interface which approximates axial symmetry and is usually concave to the melt, often giving a nearly spherically shaped interface and a circular cross section to the crystal. Several examples can be found in the body of the report. When a crystal was grown without rotation in a strong field of 5500 G, the cross section of the crystal became elliptical and the growth interface became cylindrical in contrast to the normal spherical shape. The generatrix of the cylinder was aligned with the field and, if the seed was rotated to another stationary orientation in the field, the cylindrical surface immediately realigned itself to the new field direction. Figure 3 shows a crystal grown under these conditions. About halfway along the crystal, the seed was rotated through an angle

RADIAL SPREADING RESISTANCE SCANS FOR AXIAL FIELD CRYSTALS

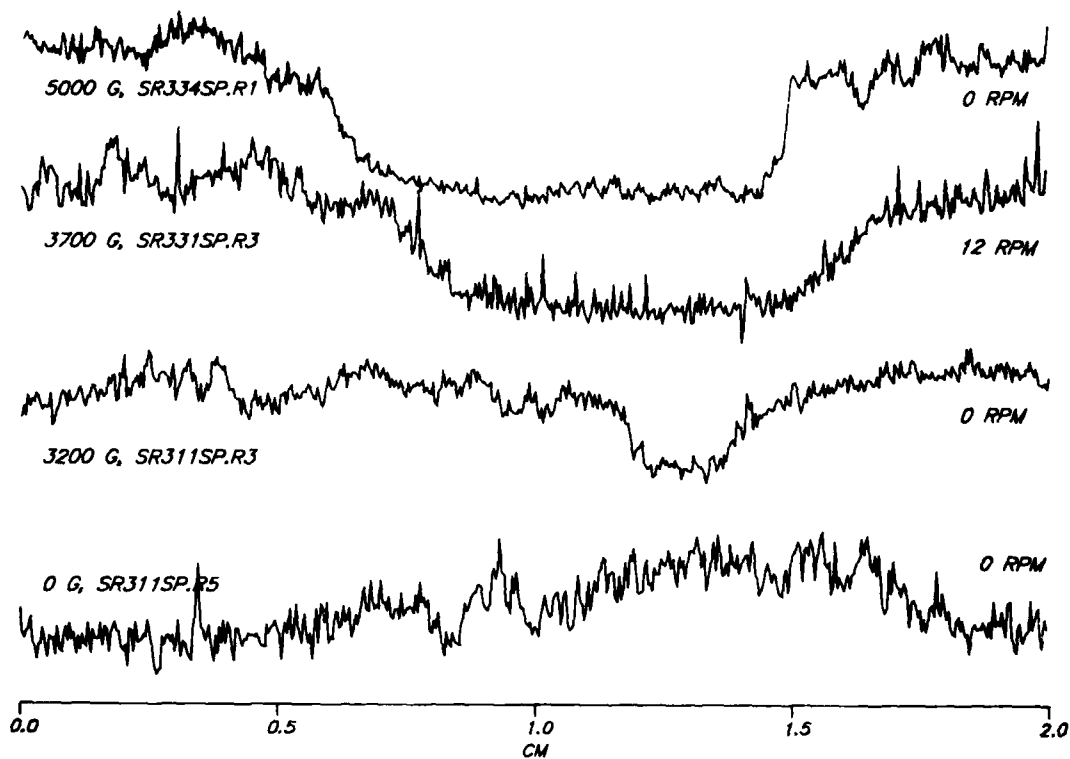


Figure 2. Radial spreading resistance scans for crystals grown in an axial field. The core region is only well developed for fields above 3200 G.

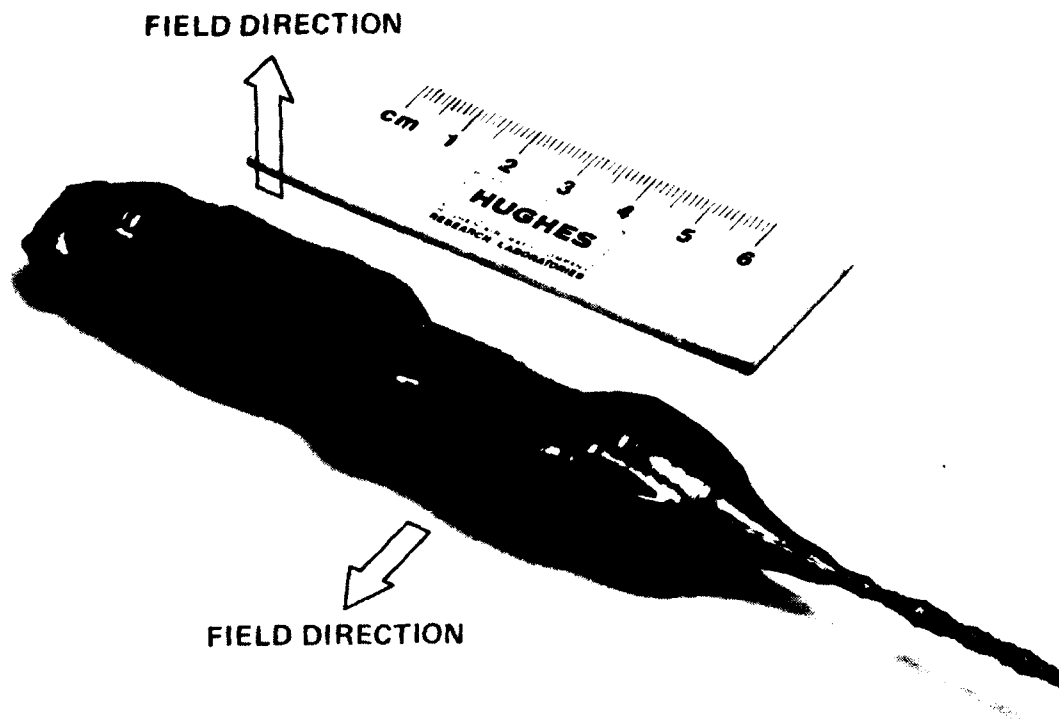


Figure 3. Morphology of crystal Z321 grown without rotation in a 5500 G transverse field. The seed was rotated by 90 degrees halfway through growth and the elliptical cross section reoriented itself in the field.

of 90 degrees and the realignment of the elliptically shaped crystal is apparent. It is significant that the location of the non-rotating sections of the crystal was quite stable with respect to the growth axis, a condition not usually observed in the absence of the magnetic field. Striation etch patterns of the non-rotating sections reveal very unusual patterns that are not yet fully understood, but which apparently are the result of forced oscillations of low frequency in the melt volume. A study of these flow patterns, which occur in the absence of crystal rotation, may reveal details of turbulent flow in the melt which have thus far eluded experimentalists.

Unfortunately, the added stability of non-rotating sections observed with the strong transverse fields has not been seen with an axial field. Rather, there is a strong possibility that the axial field destabilizes the non-rotating crystal. More work is needed to properly characterize the growth parameters that will eventually lead to useful volumes of homogeneous core material for use in detector fabrication. Future work should be concentrated in four areas: (1) application of modeling theory to the present results and the performance of new experiments to increase our understanding of the physics of mass and energy transport in the float zone process; (2) development of techniques for controlling the stability of crystals grown without rotation in an axial field; (3) establishment of the growth parameters that control the homogeneity and doping levels in the core region of non-rotating crystals; and (4) Extension of the present results to crystals of larger diameter. We believe that coordinated efforts in these four areas will lead to a level of quality for detector grade silicon that has never before been attained.

SECTION I

INTRODUCTION

Uniform IR responsivity is a desired feature of extrinsic silicon detector focal plane arrays. This uniformity of responsivity requires that the Si material from which the arrays are fabricated must possess uniformly distributed dopants. Previous work on the LADIR Materials Program [1] examined the causes of dopant non-uniformity in float zone Si crystals and related these to the conditions existing during growth of the crystal. Non-uniform doping causes striation patterns that are revealed by selective etching or that can be detected by resistivity measurements. In the previous work, fluctuations in the concentration of both minor and major dopant species could not be completely eliminated by using only the normal set of growth parameters available to the crystal grower. Therefore, preliminary experiments [2] were conducted to determine if the incorporation of a transverse magnetic field into the float zone process could provide an additional growth parameter that would allow further reduction of dopant fluctuations. The apparent success of these early experiments led to the initiation of the present program in which a more thorough investigation has been conducted.

In the first phase of this program, the preliminary experiments were expanded to include as broad a range of conditions as was possible with a small permanent magnet located within the growth furnace. This magnet was limited to a fixed field strength of about 1800 G and was not practical for conducting experiments with varying field strengths. The next step in the program was the construction of a simple electromagnet that would fit within the furnace and provide a range of field strengths. Because of space limitations, this first electromagnet was capable of reaching a field strength of only 1600 G. The results from crystals grown with both the

permanent magnet and the electromagnet were presented in the first interim report [3]. It was concluded at that time that higher magnetic field strengths must be investigated if we were to realize any real benefit from a magnetic field.

The second interim report [4] of this program presented the results obtained with an electromagnet that was specially designed to fit within the growth furnace and provide a field strength of 3000 G. Because of the severe configurational constraints, this magnet required several compromises in its design to achieve the desired field strength. In particular, it produced a solenoidal field that was inclined at an angle of about 40 degrees to the growth axis. It was given the name "tilted solenoid" magnet because of its physical configuration and the resulting field direction. This field orientation, consisting of both axial and transverse components, complicates analysis of the interactions of the magnetic field with the molten zone above the growing crystal. Nevertheless, the experience gained both with the use of this magnet and also with the means for evaluating the striation patterns of crystals grown in its fields has proved invaluable in defining the equipment and techniques which have made possible the results which constitute the bulk of this Final Report.

Not long after experiments began with the tilted solenoid magnet, it became apparent that its thermal design was grossly inadequate. Although the magnet was capable of producing the 3000-G magnetic field for which it was designed, the current required for this field strength resulted in heat losses within the magnet which were much larger than could be removed by the water cooling system internal to the magnet. Consequently, we were never able to operate this magnet at its full field strength for more than a few seconds. The highest field that could be sustained during crystal growth was 2000 G. Even at lower fields, the heat generated within the magnet over the

course of many experiments lead to the failure of the electrical insulation in the interior of the magnet. Although the crystals grown in the field of this magnet were limited by geometrical constraints to a diameter of 2 cm, the techniques developed to analyze them have proved very useful in subsequent work. The results, though taken to be of limited value at the time, are now seen as consistent with later results obtained under more carefully defined conditions. Moreover, the experience gained with the tilted solenoid magnet system led to the design of a markedly different growth procedure and an external magnet system with adequate cooling capacity to allow both axial and transverse magnetic field strengths up to 5000 G. Work with the strong fields of this new magnet system has led to observations of unique dopant distributions.

SECTION II

BACKGROUND INFORMATION

The use of magnetic fields during the growth of a variety of crystals has been the subject of several investigations in recent years [5 - 8]. The application of a magnetic field has resulted in improved material for both Si and GaAs crystals grown by the Czochralski (CZ) method [9 - 11]. The improvement is due to reduced temperature gradients in the melt as well as to a reduction of convection currents which normally enhance dissolution of the growth crucible with a consequent incorporation of contaminants into the crystal. The furnace configuration for CZ growth is well suited to the use of solenoidal superconducting magnets which provide axial or transverse fields of several kilogauss at reasonable power inputs.

For the float zone process, the circulation currents present in the molten zone are known to be more complex because of the peculiar configuration of the molten zone and because of the presence of several driving forces that can potentially contribute to convection. These driving forces are still not well characterized and the circulating flows that they produce are the subject of on-going research [12]. In Appendix A, these forces are discussed along with the Navier-Stokes equation, modified to include the Lorentz force resulting from the magnetic field interaction with the conductive silicon melt. As yet, analytic solutions to this equation are not worked out for boundary conditions corresponding to real growth configurations, but progress is being made with numerical approximation methods [13].

The overall objective of this program is the reduction of the spatial variation in dopant concentration brought about primarily by temporal variations in growth rate caused by temperature fluctuations near the growth interface. The

approach that has been followed was to use a magnetic field to alter the melt circulation currents with the expectation that dopant fluctuations could thereby be reduced. Because theory is not yet well enough developed to be of practical use in predicting the effects of the magnetic field, an empirical attack on the problem had to be made. Much has been learned about the effects of a magnetic field on dopant distribution, and the results promise to increase our understanding of the complex growth process and eventually to provide substantially improved detector grade silicon.

SECTION III

EXPERIMENTAL PROCEDURES

A. FLOAT ZONE GROWTH WITH A MAGNETIC FIELD

1. Exploratory Phases of Program

In the earliest part of this program, crystals were grown between the poles of a small electromagnet located in the ECCO ZP-7 float zone furnace so as to provide a transverse field in the region of the melt zone. Figure 4 shows the electromagnet positioned just below the growth coil. The diameter of the crystals was restricted to 2 cm by the pole separation of about 2.4 cm needed to achieve a field strength of 1600 gauss. Early visual analysis of striation etch patterns for the crystals grown at various field strengths in this magnet indicated that even higher field strengths should be investigated. Discussions with several magnet manufacturers about the design and construction of a magnet that would fit within the limited space available outside of the growth chamber had already shown that the emplacement of such a magnet would not be simple and that the degree of difficulty would increase with the maximum field strength desired. Because the internal placement of a magnet would not require extensive modification of the furnace, it was decided at that time to design a new internal magnet to give higher fields. The objective was to use the stronger internal magnet to determine if there existed a maximum field beyond which we did not need to go. It seemed desirable to look for the possible existence of a maximum field before committing resources to a large magnet and probably to a substantial modification of the furnace as well.

Continued discussions with magnet manufacturers soon revealed that the design of an internal magnet capable of providing 3000 gauss in a transverse field configuration was also beyond the design capability of those that we contacted.

11864-16

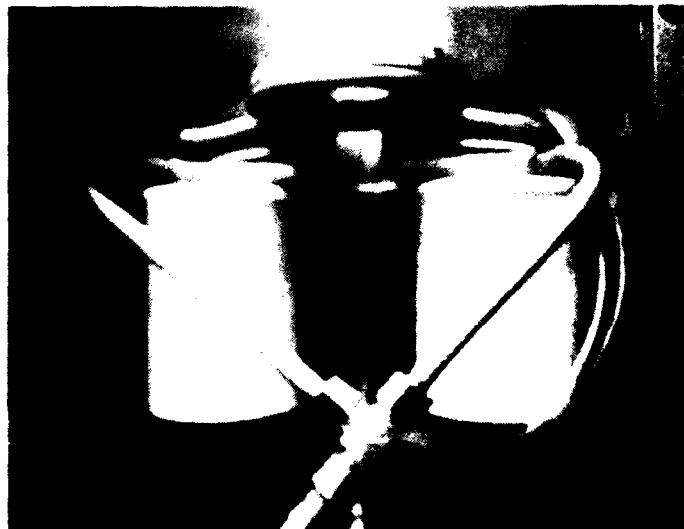


Figure 4. Electromagnet mounted in the float-zone furnace.

Through the efforts of the Program Sponsor we located a vendor willing to undertake the design and construction of an experimental magnet small enough to fit within the furnace and likely to give a field of 3000 gauss. The penalty that we had to accept to arrive at a workable design involved the location of the magnet concentrically around the rf growth coil and the acceptance of a field orientation that was a mixture of axial and transverse. With the help of a computer program available at no cost from Livermore Laboratories, the vendor arrived at a final design that appeared to be optimum for the severe geometrical constraints imposed both by the furnace configuration and by the need of the crystal grower to observe the melt zone. At that point the decision was made to proceed with this compromise design with the expectation that it would help resolve the question of the maximum field to be needed later for the growth of detector grade crystals. This magnet has been designated as the "tilted solenoid" because of its configuration and field orientation, as can be seen from Figures 5, 6 and 7. In its electrical design the magnet performed as expected, generating a field of 3000 gauss at the maximum design current of 80 A. However, its thermal design was grossly inadequate and the magnet was not capable of operating above 30 A for more than a few minutes without intense overheating. During the course of its use, the electrical insulation separating the coil windings gradually deteriorated until internal shorts developed. Because the magnet surrounded the growth region, the crystal grower was forced to use a relay mirror to gain visual access to the growth regions. This complicated the growth procedures and made it very difficult to preserve single crystal growth. Also, slow decomposition of the organic materials in the magnet contributed carbon to the furnace atmosphere and helped to discourage single crystal growth.



Figure 5. Photograph of tilted solenoid magnet.

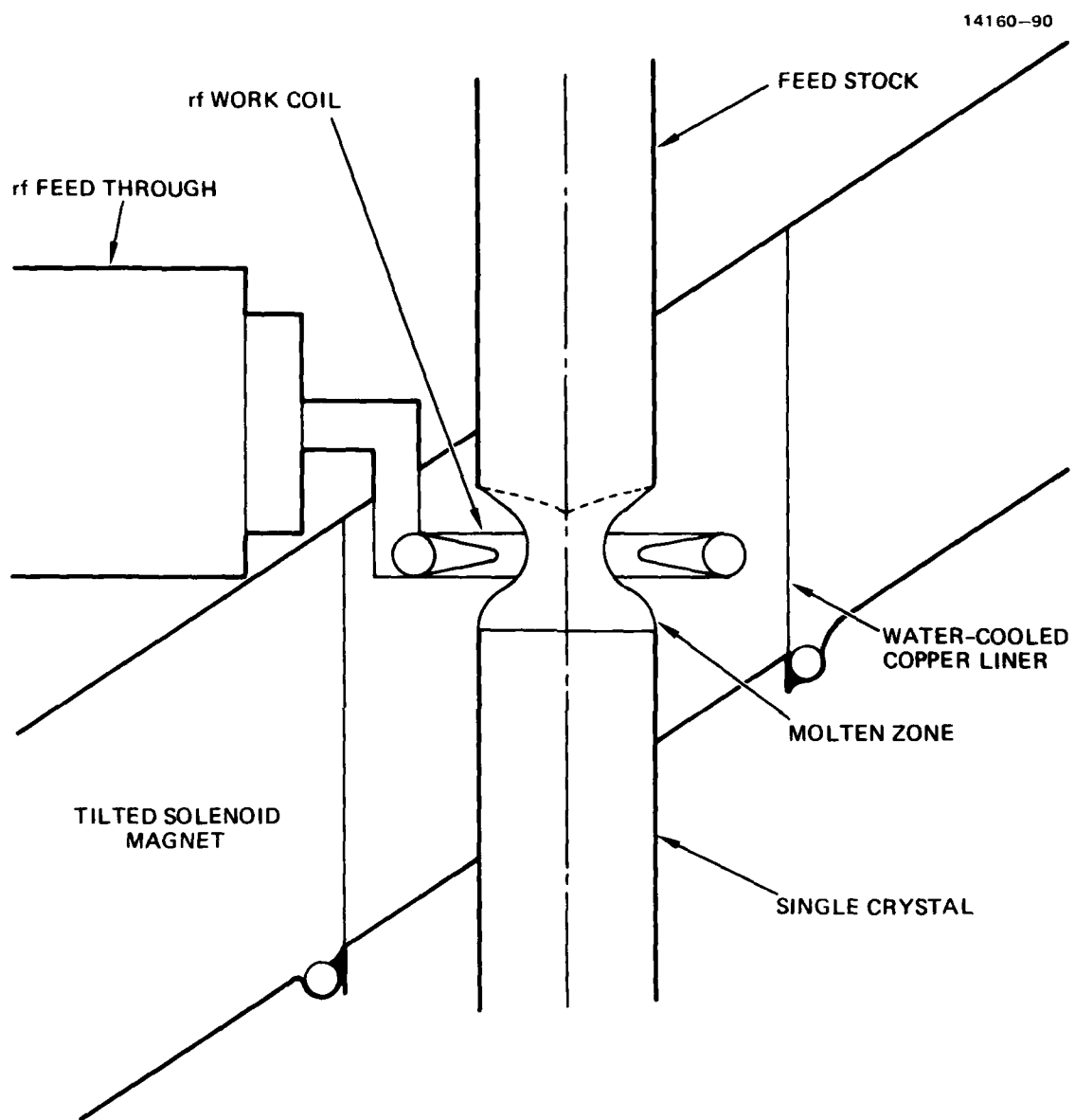


Figure 6. Growth region in tilted solenoid magnet.

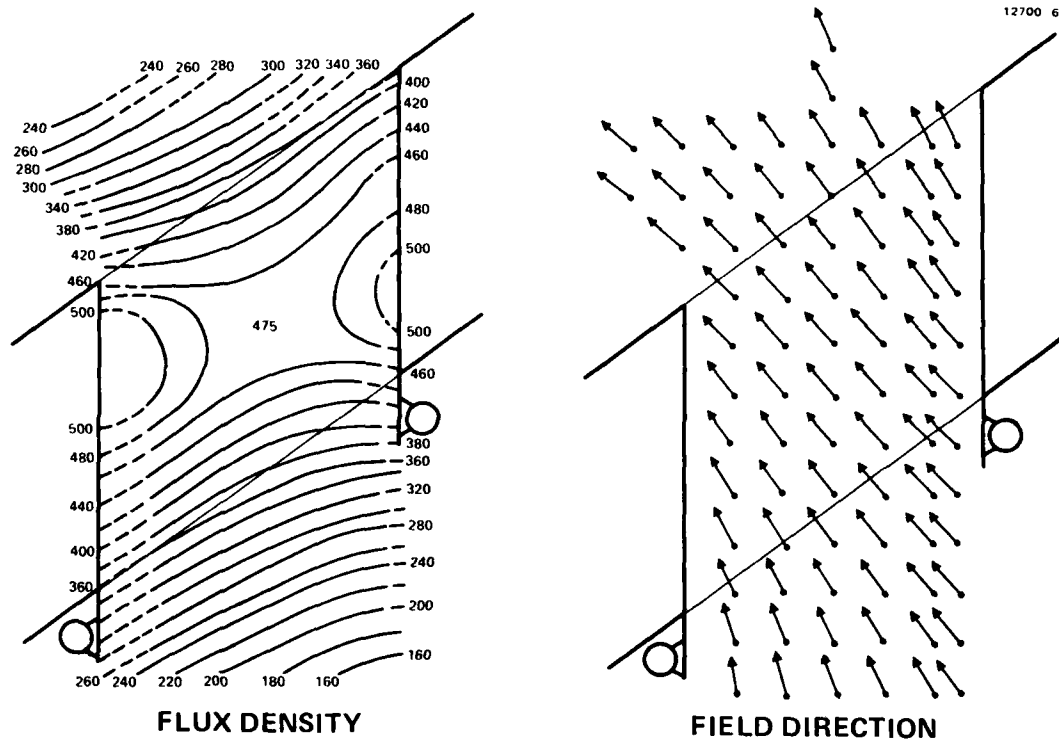


Figure 7. Field configuration for tilted solenoid magnet.

Detailed discussions of the crystals grown in the field of this magnet were given in the Second Interim Report [4]. Although the results of experiments conducted with this magnet left unresolved the determination of a maximum field strength, they did lead to the development of a method to proceed which has clear advantages over any originally envisioned. Analysis of crystals did not yield a consistent picture of the effects of the "tilted field" on the flow or circulation patterns in the molten silicon. However, the analysis efforts contributed to the evolutionary development of an evaluation method which has proved very useful in the remainder of the program. We now recognize that the results were giving "hints" of effects which became more obvious with the application of stronger fields.

2. Final Magnet System

The experiences described above with the tilted solenoid magnet established quite clearly that operation with a magnet inside of the furnace was not practical. Not only is there a serious constraint on the magnet volume, any outgassing or decomposition of the magnet structure is fatal to the growth of single crystals as well. As mentioned above, positioning of a magnet externally to the furnace did not seem any easier. If cost were no factor, the choice for an external magnet would probably be a superconducting magnet because of its relatively low power requirements. Discussions with American Magnetics, a major domestic source of such magnets, revealed that there is a practical lower limit to the size the superconducting magnet coil. Our ECCO furnaces are not large enough to accommodate even the smallest coil that is now commercially available.

We therefore redesigned the furnace to allow an external magnet of conventional design to be positioned close enough to the growth region to provide fields of at least 5000 gauss without requiring an abnormal power input. This was accomplished by moving the growth region from its normal

position at the same level as the rf coil feedthrough to a position several inches lower in the furnace. This repositioning allowed the substitution of a 4-inch diameter quartz tube for the steel furnace walls. The magnet could then be located around the quartz tube and oriented for either a transverse or an axial field direction. With a pair of coils, each consisting of 88 turns of water-cooled hollow core copper, and a total power input of 30 kW or less, we have readily generated fields of 5000 gauss with no heating problems. Location of the magnet coils outside the furnace allowed the use of conventional materials for construction and eliminated the volume-related constraints encountered previously with the electrical and thermal design of the tilted solenoid.

The new placement of the work coil has resulted in a reduced coupling efficiency in the rf circuit which has limited the maximum diameter of crystals to about 30 mm. With a better rf power supply, this limitation could be removed and crystals could be grown in this configuration at a diameter large enough to supply 2-inch wafers. The quartz tube and the magnet spacings allow the crystal grower a good view of the growth region. In Figure 8 the magnet is shown with an iron yoke and 4-inch pole pieces mounted just outside the quartz tube in the transverse field configuration. The rf coil is clearly visible to the grower and is located in a field region uniform to within a few percent. The magnetic field strength produced in this configuration is shown in Figure 9. For an axial field, the coils are mounted as shown in Figure 10 and the resulting field strength is given in Figure 11. This new magnet system has worked very well and constitutes an experimental tool with unique capabilities, as will be described later.

UPPER
FURNACE
CHAMBER

4 in.
QUARTZ
TUBE

RF WORK
COIL

MAGNET
COIL

4 in POLE
PIECE

IRON YOKE

ALUMINUM
SPACER

LOWER
FURNACE
CHAMBER



Figure 3. Modified float zone furnace with 5 kG magnet in transverse field configuration.

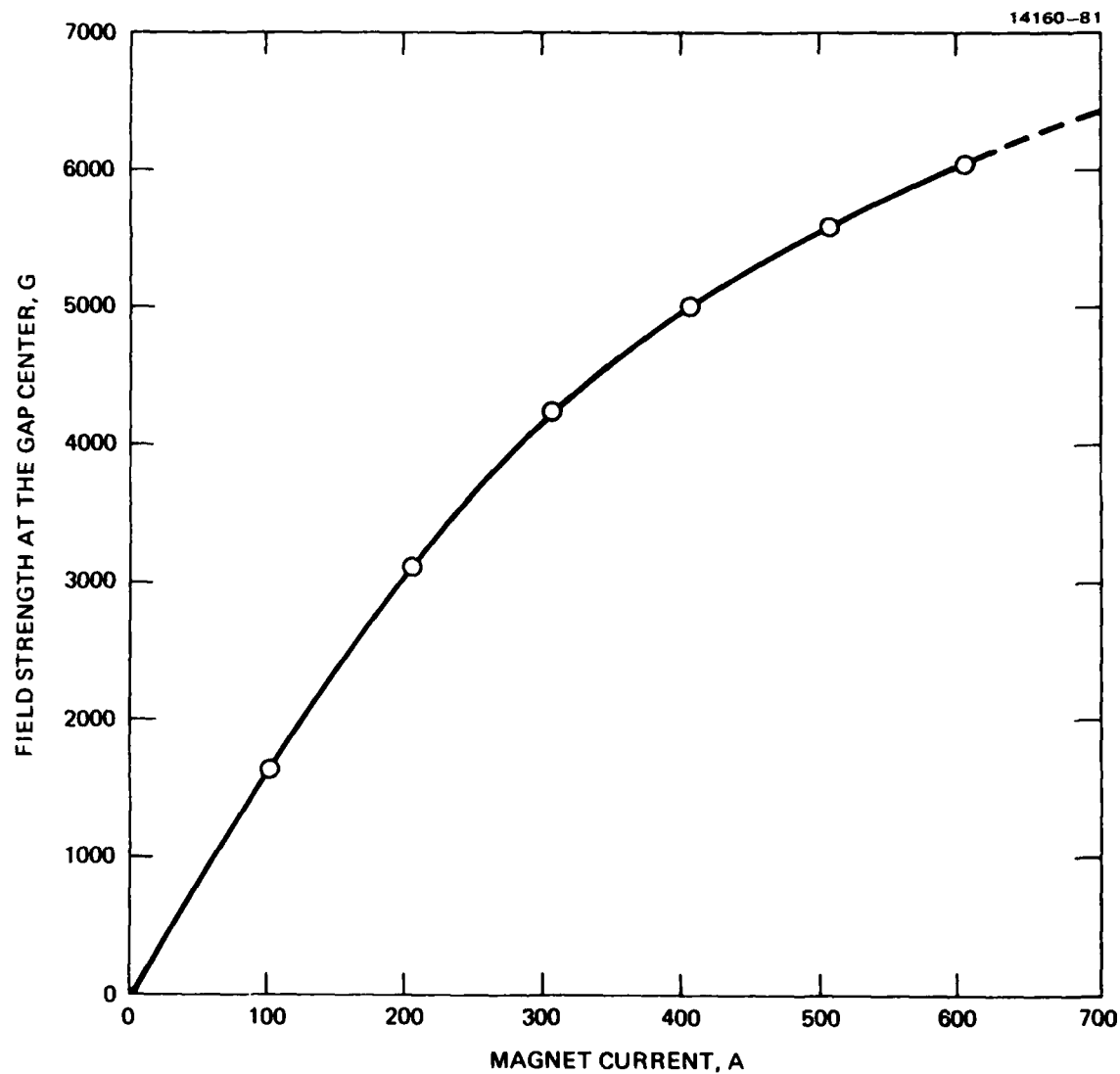


Figure 9. Calibration curve for transverse field magnet.

MC 16170



Figure 10. External magnet in the axial field configuration.

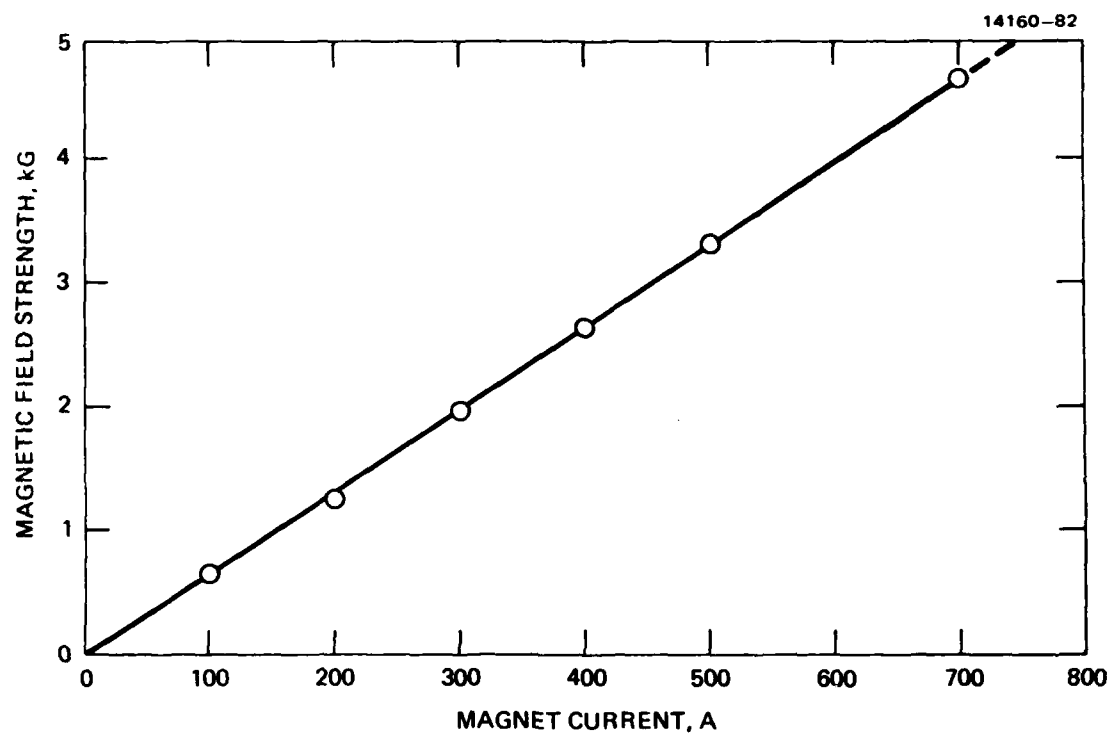


Figure 11. Calibration curve for axial field configuration.

B. Crystal Evaluation Techniques

In the past, the nature of the striations in float zone Si crystals has been determined by visual observation of the patterns revealed on a striation-etched wafer and by spreading resistance measurements on a polished surface. Both of these methods have proved useful in studying growth parameters and their effects on the magnitude of the striations. However, it would be helpful to have the quantitative data from the spreading resistance measurements in a more useful form and to have analytical options not previously available. For this reason, we have collected the spreading resistance data with a computer so that we may analyze the data in more sophisticated ways than is practical with data that is recorded only on graph paper, as was done earlier. In particular, one can readily generate power spectral density data by means of the fast Fourier transform (FFT) and thus be able to recognize spatial and temporal frequencies in the dopant concentration fluctuations that may be related to the growth parameters. In order to improve the spatial resolution so that we may see "high" frequency phenomena, we have adopted the use of a single point probe instead of the two-point probe that we used in the past. The single probe technique requires a low impedance contact to the back of the sample to complete the circuit. After some experimentation, we perfected an indium solder contact that works quite well with Si:Ga. With a carefully dressed probe it is possible to reduce the sample spacing to 5 μm and thus in principle to be able to detect higher spatial frequencies than was possible with the 20- μm spacing used earlier with the double point probe. After taking considerable data at the 5- μm spacing for crystals grown in the tilted solenoid, we discovered that the spreading resistance apparatus did not provide a uniform spacing at this separation and we have taken all subsequent data at a spacing of 10 μm for which the

spacing is quite uniform.

To illustrate the nature of the computer collected data, we will present first a specific example, typical of much of the data collected. This example is from crystal Z285 which was grown early in the life of the tilted solenoid magnet when it was still able to provide a field of 2000 gauss. For purposes of illustration, we will show the original spreading resistance data, the striation etch pattern, and corresponding FFT analyses for this region of the crystal, but will defer any discussion of the data until the next section. Both the spreading resistance data and the striation etch pattern for crystal Z285 show obvious differences between the regions with and without the field. Figure 12 is a computer drawn graph (file number SR285SP.AH1) of the spreading resistance data in the vicinity of the transition from the region with the magnet on at 2000 gauss to the following region in which the magnet had been turned off. In Appendix B, we explain the numbering system by which the data and FFT files are identified and also the meaning of the coordinate systems for their graphs. The original data plotted out by the spreading resistance apparatus for these same regions are given in Figure 13. In this and all following spreading resistance plots, the scanning direction is from the seed end toward the tang end of the specimen. Figure 14 shows a photograph of the striation etch patterns for this part of the crystal. The location of the point at which the magnet is turned off is not difficult to find from these records and one would presume that the analysis of such data by the FFT method would not add much new insight. This is indeed the case, as can be seen from the power spectral density curves given in Figure 15 in which the strong periodicity associated with the "magnet on" region corresponds to the the actual rotational frequency of 15 rpm.

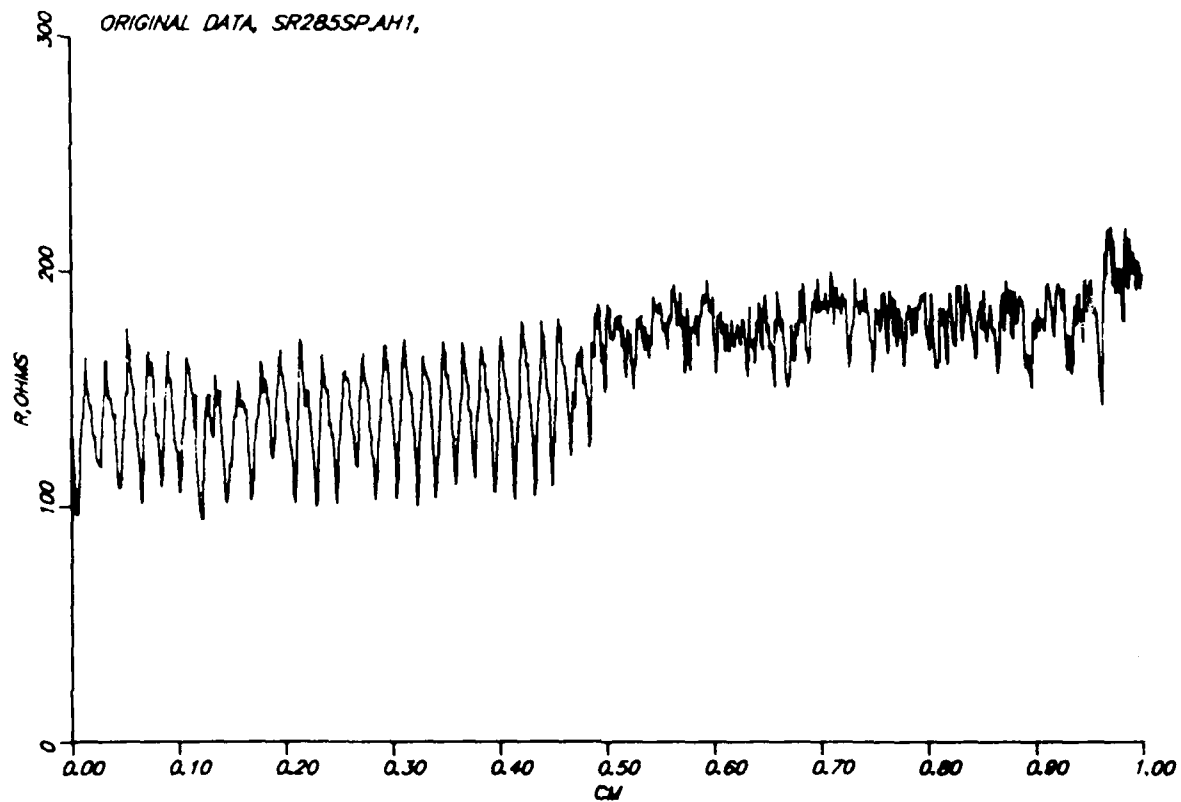


Figure 12. Spreading resistance data for crystal Z285.

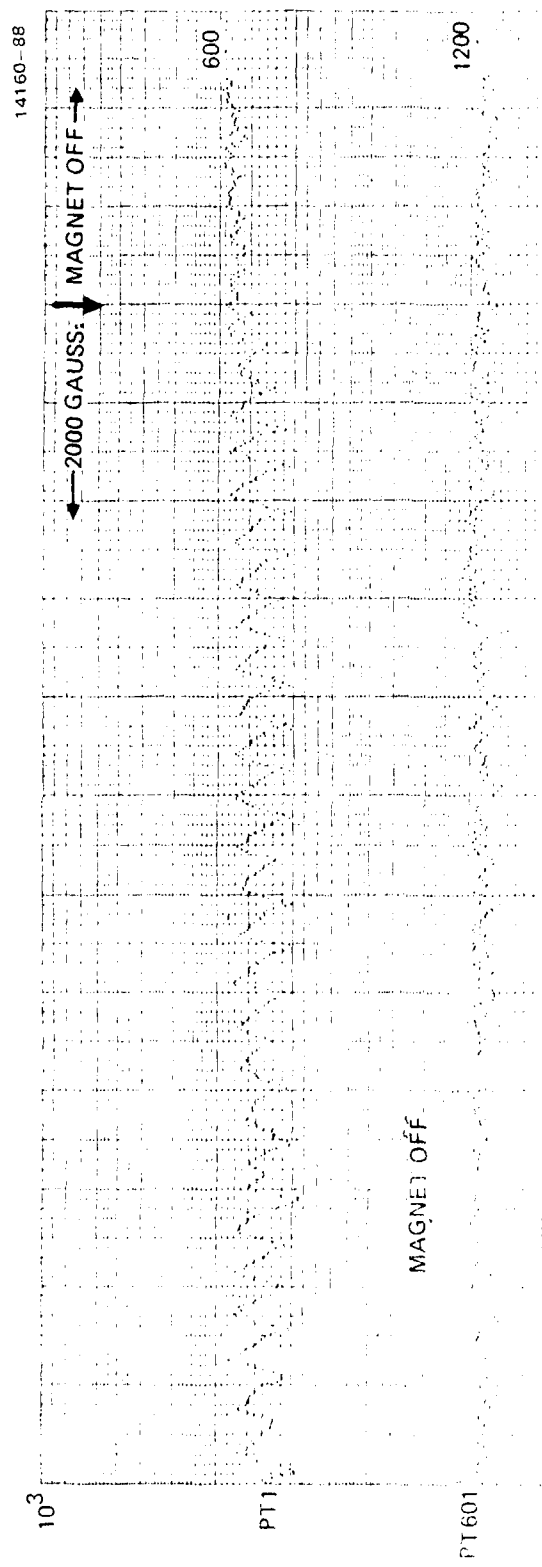


Figure 13. Original spreading resistance data plot for the 2000 to 0 gauss transition in crystal Z285 seen in Figure 4-9.

14160-86

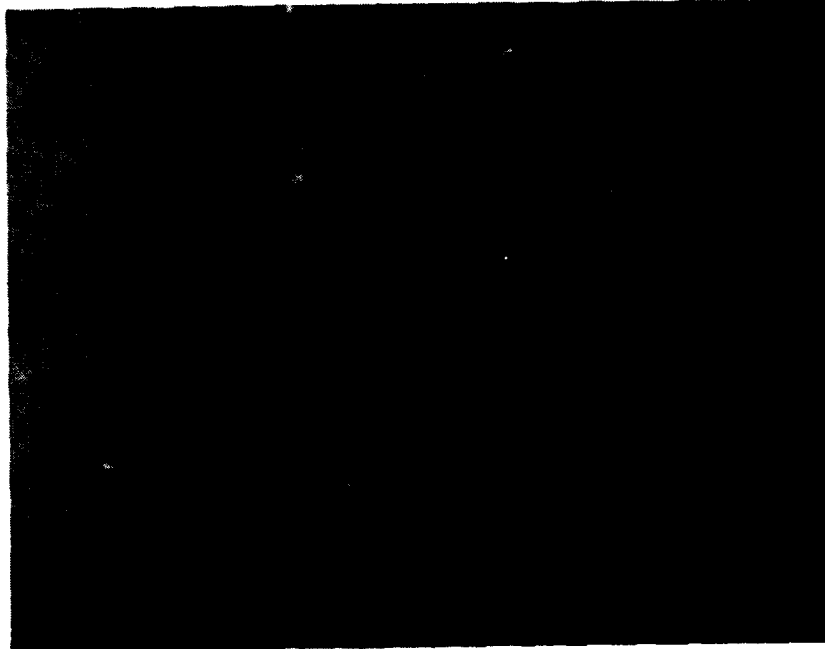


Figure 14. Striation etch pattern for the region of crystal Z285 in which the field was removed, see Figure 4-9.

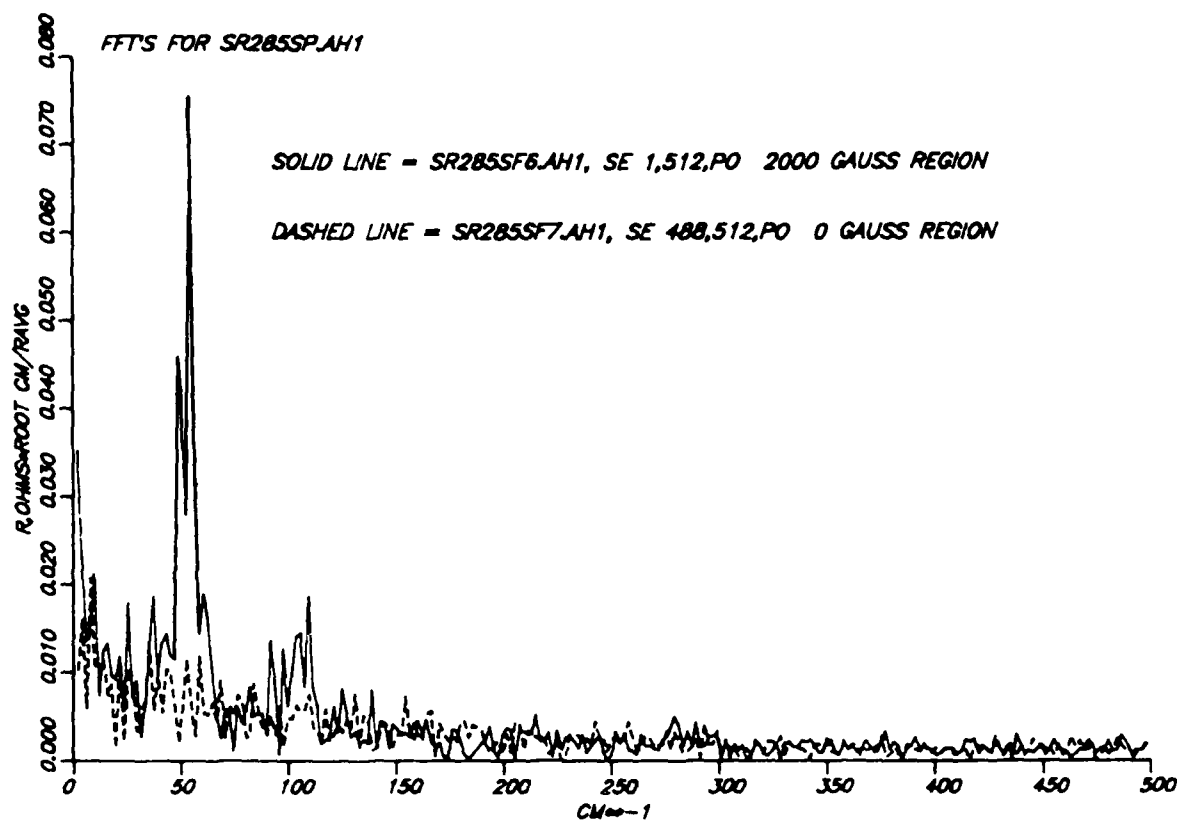


Figure 15. Power spectral densities for crystal Z285.

In contrast to the data from crystal Z285 is that from crystal Z292 which was grown under lower magnetic fields and contains a region in which the crystal was grown without any rotation. This zero-rotation condition is not typical of the 2-in. crystals grown for detector applications. However, it may present an opportunity to study high frequency circulation currents in the silicon melt in the absence of a masking influence caused by rotational effects. In the non-rotating region, the magnetic field, at a strength of about 900 gauss was turned off. When one looks at the spreading resistance data around this transition from on to off, it is not obvious where the transition actually occurs. In Figure 16, the pattern of resistance fluctuations does not show a distinct character change as was seen in the earlier data of Figure 12 for a similar transition in crystal Z285 at a higher field strength. The striation etch pattern should show a change when the magnetic field was removed; however, we were unable to obtain good striation etch patterns of the crystal region represented in Figure 16, probably because of the relatively low Ga concentration. However, if one takes FFT's of the "early" and "late" regions of the data in Figure 16, corresponding, respectively, to magnet-on and magnet-off regions, then a distinct difference in the power spectral density occurs at some frequencies, as can be seen in Figure 17.

At the present we are still not sufficiently acquainted with this analysis method to be able to draw definite conclusions from such subtle differences as seen in Figure 17. However, we will discuss similar data in the next section and we believe that the power spectral density plots will prove very useful in the future for analyzing the fluctuation spectra of turbulent flows within the melt.

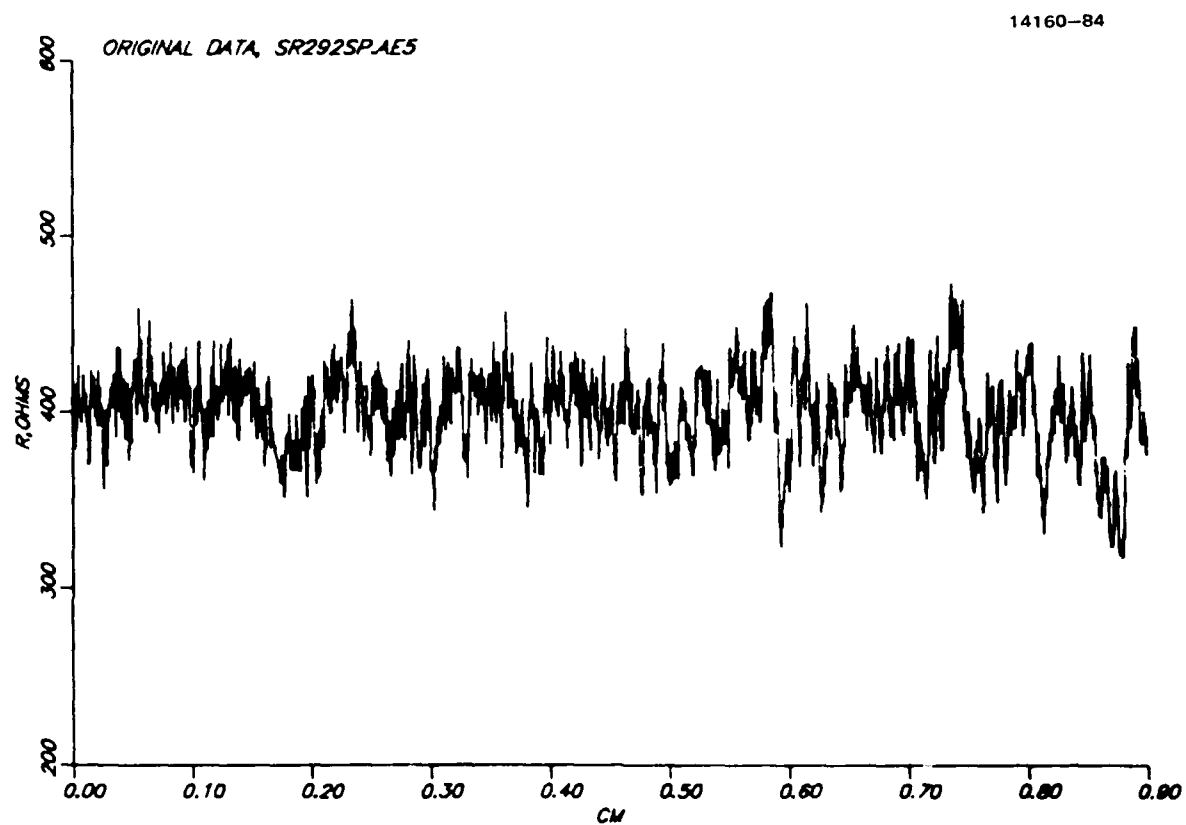


Figure 16. Spreading resistance data for the non-rotating section of crystal Z292.

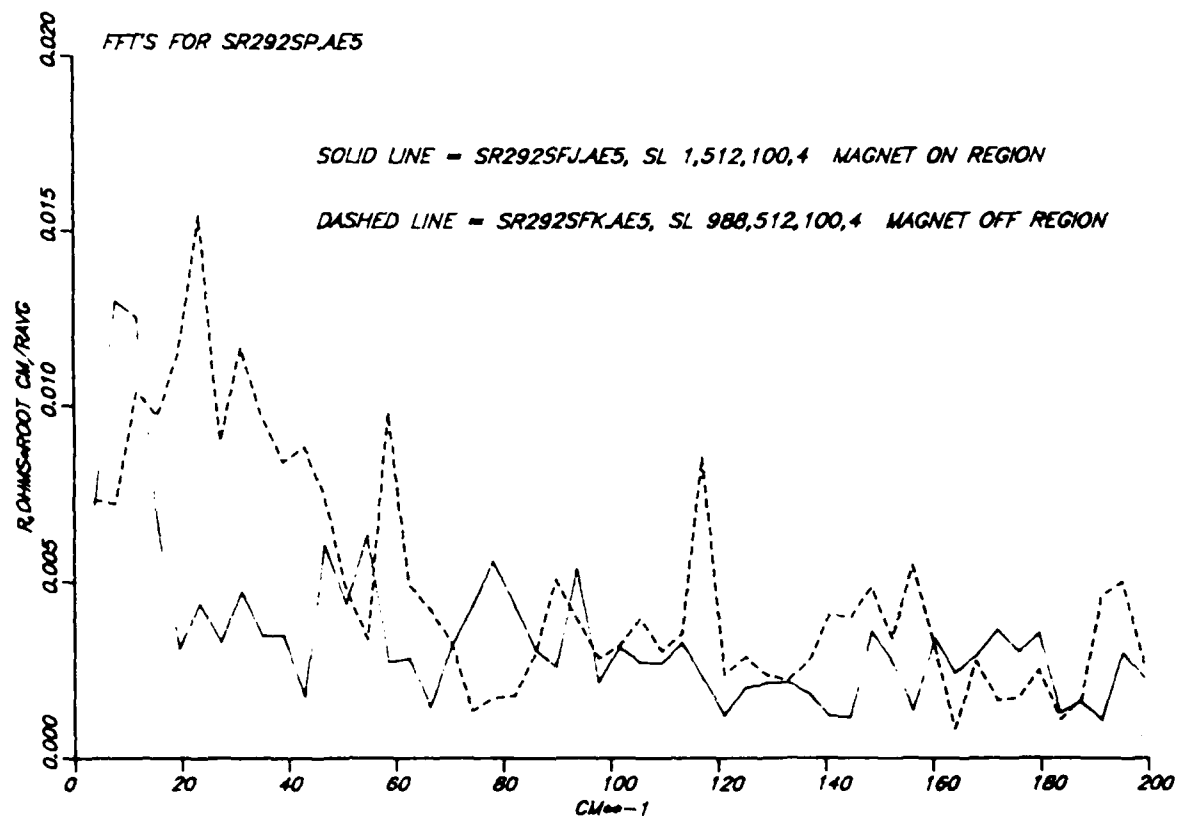


Figure 17. Power spectral densities for the non-rotating section of crystal Z292.

SECTION IV

DISCUSSION OF EXPERIMENTAL RESULTS

Experimental crystal growth has occurred primarily in three periods of concentrated activity, the nature of each being governed mainly by the magnet then available. These magnets were: (1) a small internal electromagnet, (2) the internal tilted solenoid magnet, and (3) the external two-coil magnet system. In the early work, time needed for sample preparation and analysis was too long to permit feedback in time to influence the growth of crystals under a given set of conditions. The long evaluation cycles required that we guess at the growth parameters to be investigated next, long before their relative importance had been clearly established. Thus we found ourselves choosing growth conditions for the newest magnet on the basis of results obtained from the previous magnet. The danger in this mode of operation is that, while some particular set of conditions might indeed bring about desirable results, that set might not be among those selected for investigation. The stability and good performance of the external magnet system now insure a workable long-term experimental set-up which will permit us avoid this mode of operation in any future work.

Because the results obtained for crystals grown with the first two magnets seem less definitive of the magnetic field effects than are those more recently obtained at higher field strengths, the earlier results will not be presented in any detail, but will be referred to only in the context of the later findings. Considerable evaluation data on 2 crystals from the first magnet and 7 from the tilted solenoid have already been presented in the Second Interim Report for this program [4]. Figure 18 summarizes the various sets of growth parameters covered in the crystals grown with the first two magnets. Particular effects observed in these crystals will be mentioned as we discuss results from the crystals grown at higher fields.

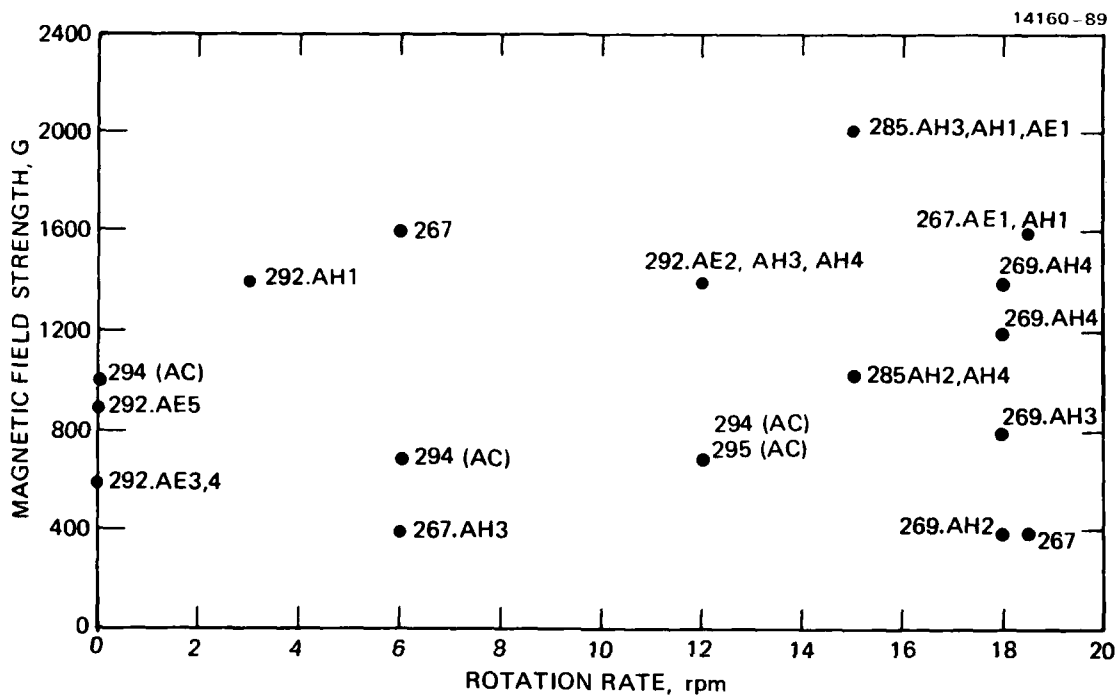


Figure 18. Matrix of growth conditions explored with early magnets.

For the newest magnet system, we have grown 17 crystals with the combination of parameters listed in Table 1. It is these that form the basis for most of the following discussion. In addition, three more crystals were grown in an axial field for delivery to the Sponsor.

For convenience of presentation, we have divided the discussion into three parts, the first dealing with rotating crystals of conventional character grown with a transverse magnetic field, the second describing crystals grown without rotation in a transverse field, and the third discussing the effects of an axial field orientation which shows some important differences from the transverse field. While crystals grown without rotation are not now used for device material, they may offer valuable insight into the physics of the float zone process and could eventually lead to the development of crystals with substantially reduced striations. The method of presentation will be to enumerate the various effects of the magnetic fields that have been observed, give specific examples, and where possible present explanations or hypotheses for the observed behavior.

A. ROTATING CRYSTALS IN A TRANSVERSE FIELD

1. Interface Shape Change

Perhaps the most obvious effect produced by the presence of a magnetic field is a change in the shape of the growth interface, as revealed by striation etch patterns. Generally this change is a reduction in the concavity of the growth interface when the field is turned on. In many cases, the interface becomes almost "flat" except for a small region at the outer diameter of the crystal. This is seen in crystal Z309 for both the 6 and 12 rpm regions shown in Figures 19 and 20. This reduction of curvature can also be seen for crystal Z285, already presented in Figure 14, although at the lower field

Table 1. Growth Conditions for Crystals
Grown in Strong Magnetic Fields.

Crystal No.	Growth Rate mm/min	Rotation Rate rpm	Magnetic Field Gauss
Z309	4	6,12	5500
Z311	4	6,0,6,12	3200 (Axial)
Z316	5,3	3,12	5500
Z317	5	3	5500
Z318	4	2,0	5500
Z319	4	4,12	5500,3200
Z321	4	12,0	5500
Z322	4	2,0,2.1	5500
Z323	4	13,3	5500 (Interrupted)
Z324<111>	4	13,0	5500,4200,3100
Z326	4	13,6,0,13	5500 (Interrupted) 1000
Z327	4	6	5500 (Interrupted) 1600,3100,4200
Z328<111>	4	13,6,0,6	5500
Z331	4	12,3	3700 (Axial)
Z332	4	12,3	4000 (Axial)
Z333	4	12,3,0	5000,3700 (Axial)
Z334	4	0	5000 (Axial)

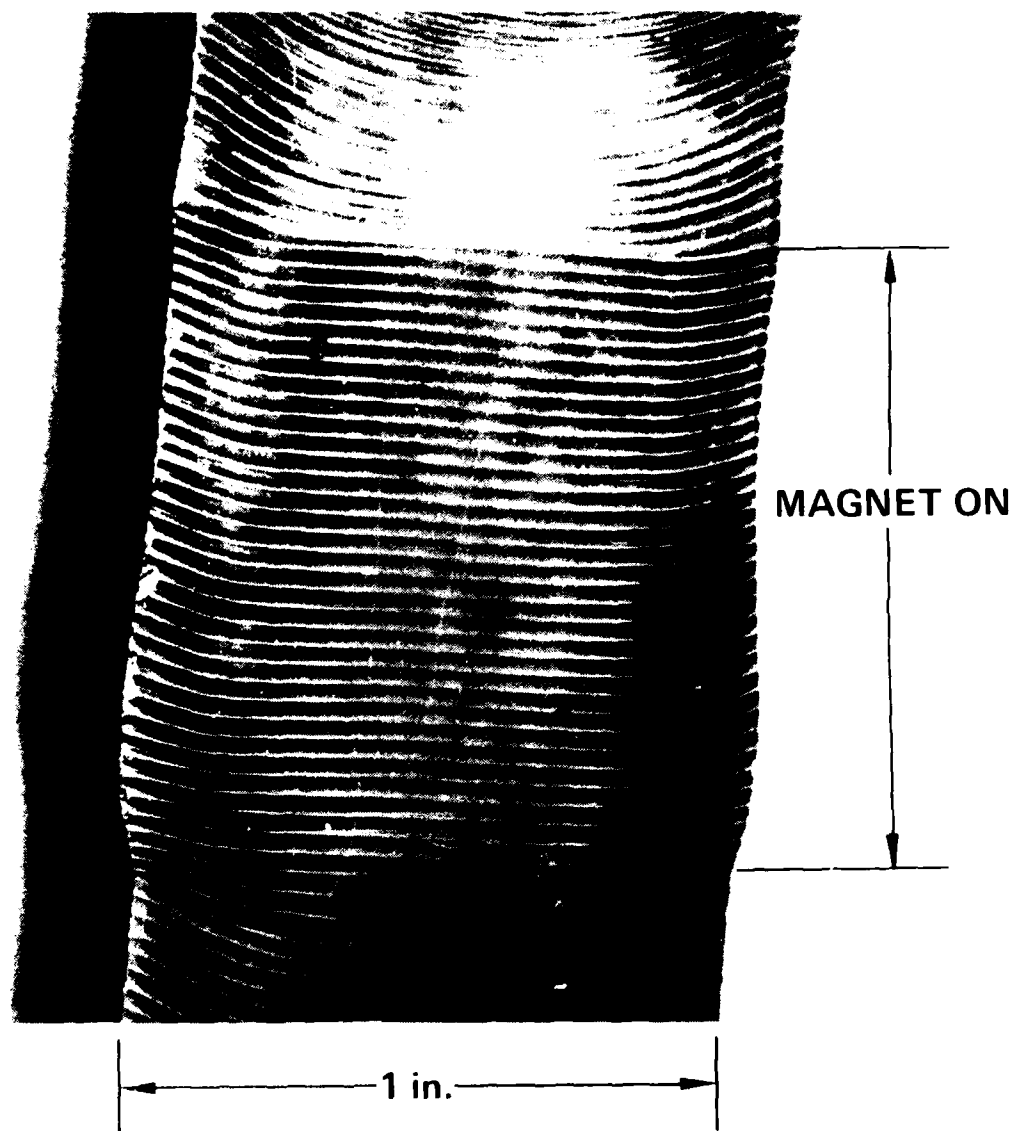


Figure 19. Striation etch pattern for the 6 rpm section of crystal Z309, grown in a 5000 gauss transverse magnetic field.

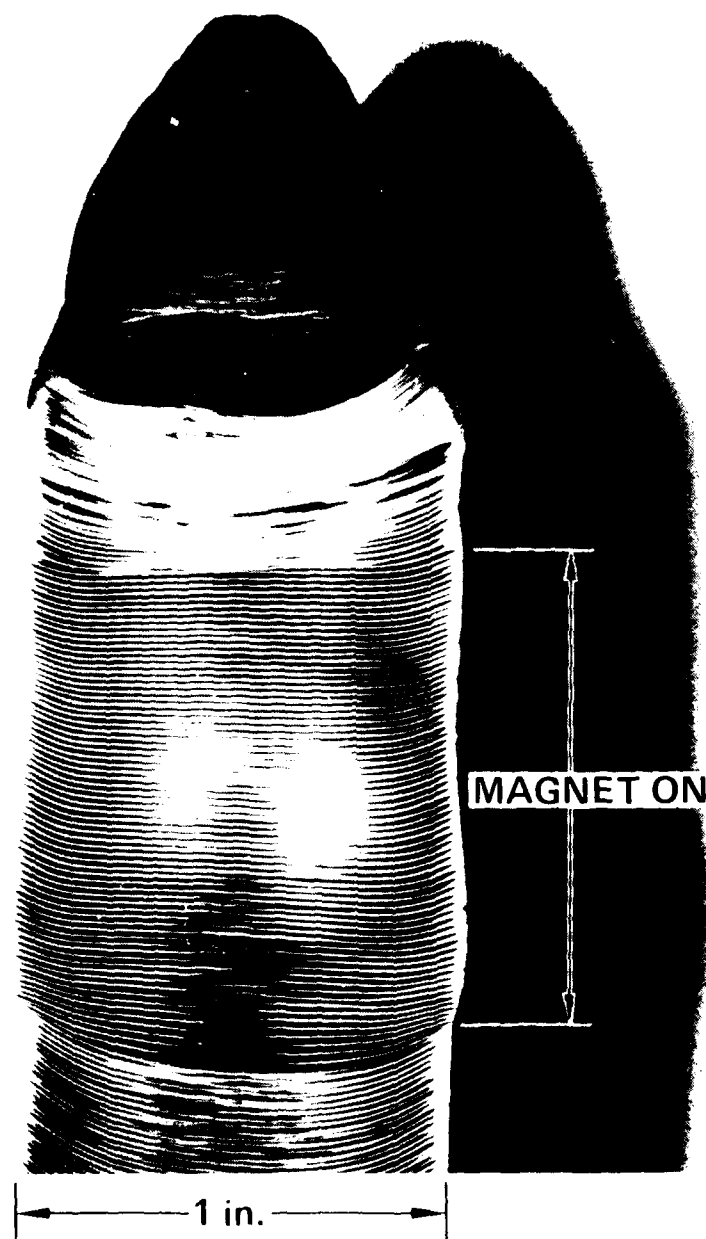


Figure 20. Striation etch pattern for the 12 rpm section of crystal Z309 grown in a 5000 gauss transverse magnetic field.

strength the interface does not become flat. Many other examples can be noted in later figures. This change in shape is reflecting changes in the energy transport to the growth interface. Later on we will discuss the flow patterns responsible for this morphological change.

2. Crystal Diameter Change

An immediate consequence of the flattening of the interface is an increase in the diameter of the growing crystal. When the magnetic field is removed, the interface resumes its former curvature. These shape changes occur rapidly without a corresponding change in the existing volume of molten silicon. Therefore the diameter of the melt expands or contracts in direct response to the curvature of the interface. This effect can be seen in crystal Z323, for which the magnet was cycled on and off at a strength of 5500 gauss while the crystal was rotating at 13 rpm. Figure 21 shows the exterior surface of this crystal in the two regions where the field was alternated between on and off at 30 and 60 second intervals. The changes in diameter can be seen in the pattern of light reflected from the outer surface of the crystal. In these cases, the crystal grower made no adjustments to either the rf energy level or the rates at which material was added to or withdrawn from the growth region. With other crystals we have observed that if no adjustments are made after the magnetic field is applied or removed, the crystal will return to its original diameter in about two or three minutes. This appears to represent the time of readjustment of the system to the new interface shape.

It is interesting to note in Figure 21 that the growth rings, each of which represents one revolution of the crystal, are not uniformly spaced but are farther apart when the magnet is off. This spacing is consistent with the change in interface curvature. Figure 22 shows a striation etch pattern for the region where the magnet was successively on for 30 sec and off

Figure 21. Diameter changes for crystal Z323 at 13 rpm.



Figure 22. Striation etch pattern for crystal Z323 in the region where the magnet was ON for 30 sec and OFF for 30 sec. This region corresponds to that of b) in Figure 5-4.

for 30 sec. When the magnet is on, the interface is growing much more quickly in the center of the crystal than it is at the edge and the interface is thereby being flattened. The reverse occurs when the magnet is off and the outer regions grow more quickly. These varying growth rates produce the different spacings of the growth rings at the perimeter .

3. Dopant Concentration Change

The spreading resistance values for several of the early crystals appeared to decrease slightly when the field was applied, suggesting that the dopant concentration had increased. The computer program enables us to calculate the average spreading resistance for any selected region of the data. For several of these early crystals there were comparable regions in which the only difference was the presence or absence of the field. The data already given in Figure 12 is a typical example. For these regions we have calculated the average resistances and listed the comparisons in Table 2. The terminology used in Table 2 to describe each comparison is, in the case of resistance (or dopant concentration level), a "Y" for decreased resistance (i.e. increased dopant concentration) when the field is on, an "N" for the reverse, and an "S" for the case in which they are so nearly the same as to be not clearly either a Y or an N. This table also contains a column showing comparisons of fluctuations which we will discuss later. A quick scan down the resistance comparison column indicates that in about two-thirds of the cases the dopant concentration increased when the field was applied, and, for field strengths above 1000 G, there was always an increase. The processed data on which Table 2 is based have been listed in Table 3.

Although we do not have, for recently grown crystals, as large a collection of spreading resistance data as given in Table 3, we see the same reduction in resistance level when the field is applied. Table 4 presents some recent data showing

Table 2. Resistance Levels and Fluctuation Intensities for Comparable Crystal Regions with Magnetic Fields On and Off.

14160-91

DATA FILE NAME	MAGNETIC FIELD INTENSITY G [†]	ROTATION RATE rpm	RESISTANCE LOWER WITH FIELD ON**	FLUCTUATIONS LESS WITH FIELD ON**
SR267S.AH1	1600 T	18.5	Y	Y
SR267S.AH3	400 T	6	N	N*
SR267D.AE1	1600 T	18.5	Y	S
SR267D.AE1	400 T	6	S	N*
SR269S.AH2	400 T	18	N	N*
SR269S.AH3	800 T	18	N	N*
SR269S.AH4	1200 T	18	Y	N*
SR269S.AH5	1400 T	18	Y	N*
SR285S.AH1	2000	15	Y	N*
SR285S.AH2	1000	15	Y	N*
SR285S.AH3	2000	15	Y	N*
SR285S.AH4	1000	15	Y	N*
SR285S.AE1	2000	15	Y	S
SR285S.AE2	1000	15	Y	Y
SR292S.AH5	650	0	Y	Y
SR292S.AH6	900	0	Y	Y
SR292S.AH7	900	0	N	S
SR292S.AE3	650	0	N	N
SR292S.AE4	650	0	Y	N
SR292S.AE5	900	0	S	Y
SR293S.AC1	1000 AC	12	Y	Y

†ALL FIELDS ARE FROM THE TILTED SOLENOID OPERATED IN THE DC MODE EXCEPT FOR "AC" = ALTERNATING CURRENT MODE, AND "T" = SMALL TRANSVERSE ELECTROMAGNET.

*FLUCTUATIONS DOMINATED BY ROTATIONAL STRIAE.

**SEE TEXT FOR MEANING OF SYMBOLS Y, N, AND S.

Table 3. Processed Data for Scans Used in Table 2

14160-92

SCAN NUMBER	ROTATION RATE rpm	MAGNETIC FIELD STRENGTH G	AVERAGE RESISTANCE Ω	STANDARD DEVIATION Ω	RELATIVE STANDARD DEVIATION %	DATA POINTS IN AVERAGE
SR267S.AH1	18.5	1600T	1410	117.9	8.36	1 - 600
	18.5	0	1514	149.9	9.90	1210 - 1800
SR267S.AH3	6	400T	1860	229.0	12.31	100 - 700
SR267S.AH2	6	0	1555	172.5	11.09	600 - 1400
SR267D.AE1	18.5	1600T	9855	1263	12.82	0 - 600
	18.5	0	11254	1375	12.22	1300 - 1800
SR267D.AE1	6	400T	12019	2495	20.76	3150 - 3250
	6	0	12713	2143	16.82	2450 - 3000
SR269S.AH2	18	400T	973	95.7	9.84	1 - 600
SR269S.AH1	18	0	895	77.5	8.66	401 - 600
SR269S.AH3	18	800T	1055	121.4	11.51	1 - 410
SR269S.AH1	18	0	1122	132.0	11.76	401 - 600
SR269S.AH4	18	1200T	698	95.3	13.70	1 - 500
SR269S.AH1	18	0	895	77.5	8.66	401 - 600
SR269S.AH5	18	1400T	701	81.3	11.60	700 - 1200
SR269S.AH1	18	0	895	77.5	8.66	401 - 600
SR285S.AH1	15	2000	137.0	18.16	13.26	1 - 400
SR285S.AH1	15	0	177.3	10.16	5.73	500 - 900
SR285S.AH2	15	1000	153.5	17.87	11.64	1200 - 2000
SR285S.AH2	15	0	171.3	15.78	9.21	2100 - 2700
SR285S.AH3	15	2000	153.1	23.84	15.57	0 - 400
SR285S.AH3	15	0	194.4	13.61	7.00	900 - 1400
SR285S.AH4	15	1000	150.1	18.38	12.25	400 - 800
SR285S.AH4	15	0	160.6	9.05	5.64	1 - 150
SR285S.AE1	15	2000	161.0	15.51	9.63	1 - 500
SR285S.AE1	15	0	197.3	18.32	9.29	500 - 1000
SR285S.AE2	15	1000	192.5	14.50	7.53	610 - 1180
SR285S.AE2	15	0	222.0	18.88	8.50	10 - 590
SR292S.AE3	0	650	420.5	28.02	6.66	1200 - 1800
SR292S.AE5	0	0	395.8	28.61	7.23	1200 - 1800
SR292S.AE4	0	650	344.7	31.87	9.25	1200 - 1800
SR292S.AE5	0	0	395.8	28.61	7.23	1200 - 1800
SR292S.AE5	0	900	404.1	19.93	4.93	1 - 600
SR292S.AE5	0	0	395.8	28.61	7.23	1200 - 1800
SR292S.AH5	0	650	352.4	23.56	6.69	1500 - 2000
SR292S.AH7	0	0	390.8	30.60	7.83	900 - 1800
SR293S.AH6	0	900	330.4	13.99	4.23	1 - 900
SR292S.AH7	0	0	390.8	30.60	7.83	900 - 1800
SR293.AC1	12	1000AC	156.3	12.82	8.22	1200 - 1800
SR293.AC2	12	0	185.0	18.93	10.23	1 - 1800

Table 4. Resistance Levels and Fluctuation In Intensities for Comparable Regions Grown With and Without a Strong Transverse Field

14312-50

DATA FILE NAME	MAGNETIC FIELD INTENSITY G	ROTATION RATE rpm	RESISTANCE LOWER WITH FIELD ON*	FLUCTUATIONS LESS WITH FIELD ON*
SR309S.AH3	0	12	Y	N
SR309S.AH4	5500	12	Y	N
SR309S.AH1	0	6	Y	N
SR309S.AH1	5500	6		
SR309S.AC1	0	6	Y	N
SR309S.AC2	5500	6		
SR328S.AC5<III>	0	6	Y	N
SR328S.AC4<III>	5500	6		
SR316S.AH2	0	3	Y	N
SR316S.AH3	5500			

*TERMINOLOGY SAME AS FOR TABLE 2, SEE TEXT FOR MEANING OF SYMBOLS.

this effect for every specimen pair thus far measured. The original data on which these comparisons are made is listed in Table 5. Similar effects are seen for non-rotating portions of crystals, as discussed later.

The increased dopant concentration is thought to be a consequence of a thickened diffusion boundary layer caused by the field. The Lorentz force produced by the field on the flowing silicon, which has about the same electrical conductivity at its melting point as mercury has at room temperature, results in a force that opposes the flow of the conductor in any direction perpendicular to the direction of the field. It is often convenient to think of this retarding force as having about the same physical effect as would an increase in viscosity of the fluid. For any flow component normal to the field, the melt will behave as if it were more viscous and thus the fluid layer next to the growth interface will be subjected to lower shear stresses. In effect this represents an increase in the thickness of the "boundary layer" through which the dopant being rejected at the interface must diffuse. Removal of dopant through a thicker boundary layer, at the "fixed" rate determined by the average growth rate, requires a larger concentration at the interface in order to maintain the same gradient. This increased interface concentration causes more dopant to be incorporated into the crystal.

4. Enhancement of Rotational Striae

As already seen in Figure 14, the appearance of the "field on" regions is distinctly different from that of the "field off" regions if the field strength is high enough. This is a general observation and the contrast in the striation etch pattern seems to increase as the field strength is increased. In Figures 19 and 20, we have already seen the enhanced regularity of the rotational striae when the field is applied. This same effect will be seen in later figures which have been chosen to

Table 5. Processed Data for Scans Used
in Table 4

14312-51

SCAN NUMBER	ROTATION RATE rpm	MAGNETIC FIELD STRENGTH G	AVERAGE RESISTANCE Ω	STANDARD DEVIATION Ω	RELATIVE STANDARD DEVIATION %	DATA POINTS IN AVERAGE
SR309S.AC1	6	0	99.1	8.07	8.14	1200 - 1600
SR309S.AC2	6	5500	81.9	8.39	10.24	1200 - 1600
SR309S.AH1	6	0	97.4	14.67	15.06	1 - 500
SR309S.AH1	6	5500	75.8	13.58	17.92	1000 - 1800
SR309S.AH3	12	0	99.8	13.14	13.17	100 - 600
SR309S.AH4	12	5500	91.4	15.86	17.35	100 - 600
SR316S.AH2	3	0	111.9	17.62	17.75	1 - 600
SR316S.AH3	3	5500	90.2	18.66	20.69	1 - 450
SR328S.AC5	6	0	105.5	11.48	10.88	1 - 400
SR328S.AC4	6	5500	76.1	9.25	12.15	1 - 600

illustrate some other effect. Spreading resistance data also show a distinct change in character, as has been pointed out for Figures 12 and 15. The same general effect can be seen in the spreading resistance data for the 12 rpm section of crystal Z309 grown in a strong transverse field. The original spreading resistance data shown in Figure 23 illustrate the change in dopant distribution within the striations that occurs in the strong magnetic field. The power spectral densities corresponding to the magnet on and off regions of Figure 23 are given in Figure 24. The sharpness of the magnet-on striations is seen in the additional power in the fundamental frequency as well as in the harmonic frequencies, which are missing when the magnet is off. The same characteristics are seen for the 6 rpm section of crystal Z309 in Figures 25 and 26. At lower rotation rates the magnetic field effect on dopant distributions is not quite so pronounced. This is evident in the 3 rpm data in Figure 27 for crystal Z316 which still show differences between the magnet on and off regions. But as the power spectral densities of Figure 28 indicate, the differences appear to be less dramatic than those at higher rotation rates.

We have grown only two crystals with the $\langle 111 \rangle$ orientation and their behavior appears different from crystals of the $\langle 100 \rangle$ orientation normally used for device fabrication. Figures 29 and 30 present data from the 6 rpm section of crystal Z328 $\langle 111 \rangle$ which show that the presence of the field makes a difference in the striations, but not to the extent already seen in the 6 rpm section of crystal Z309, Figures 25 and 26. The striation etch pattern for this region of crystal Z328 shows prominent rotational striae, Figure 31, but the main distinction between the magnet on and off regions is the shape of the interface rather than the appearance of the striae themselves. However, the magnet-off region of Figure 31 may not have yet reached a steady state, at which time the rotational striae might not show

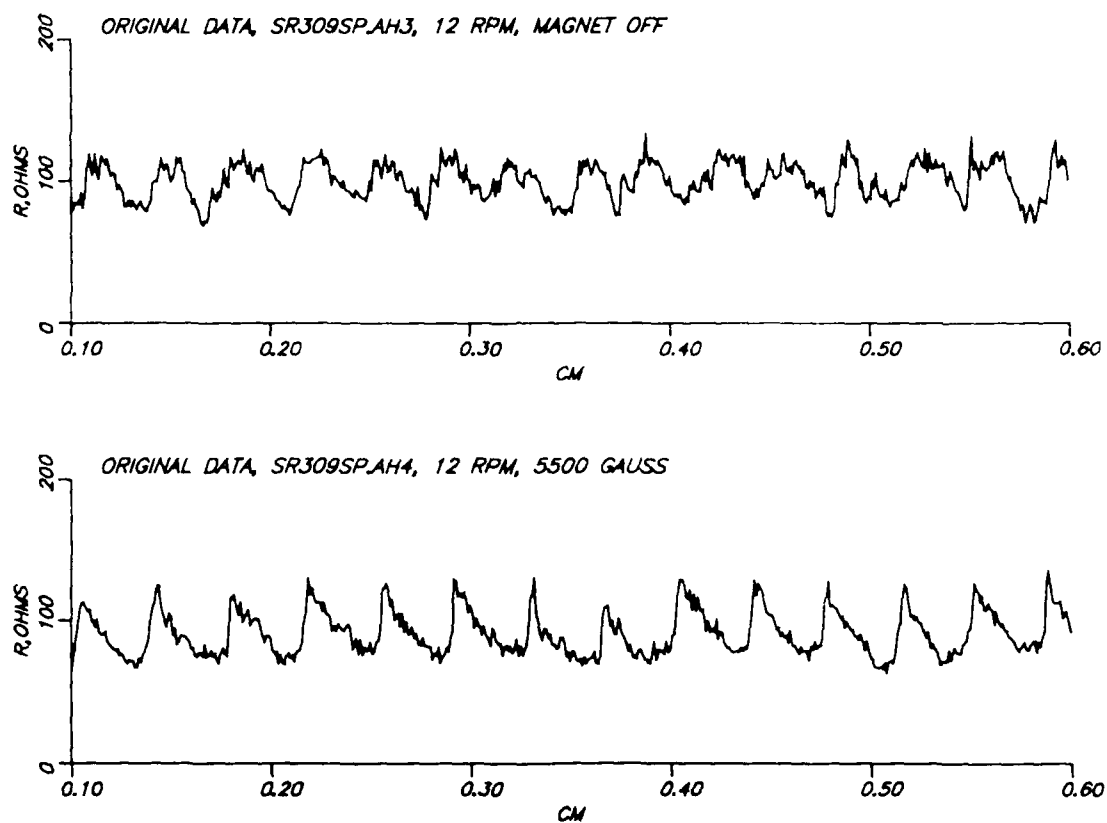


Figure 23. Spreading resistance data for the 12 rpm section of crystal Z309.

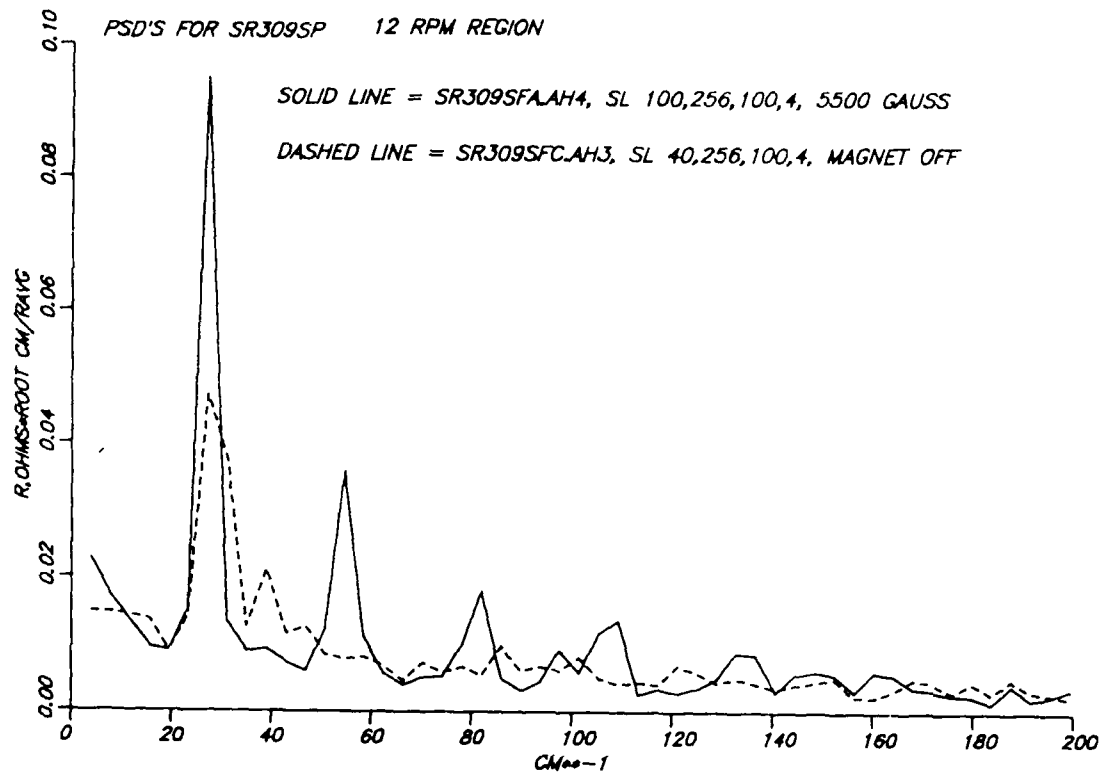


Figure 24. Power spectral densities for magnet-on and -off regions of the 12 rpm section of crystal Z309.

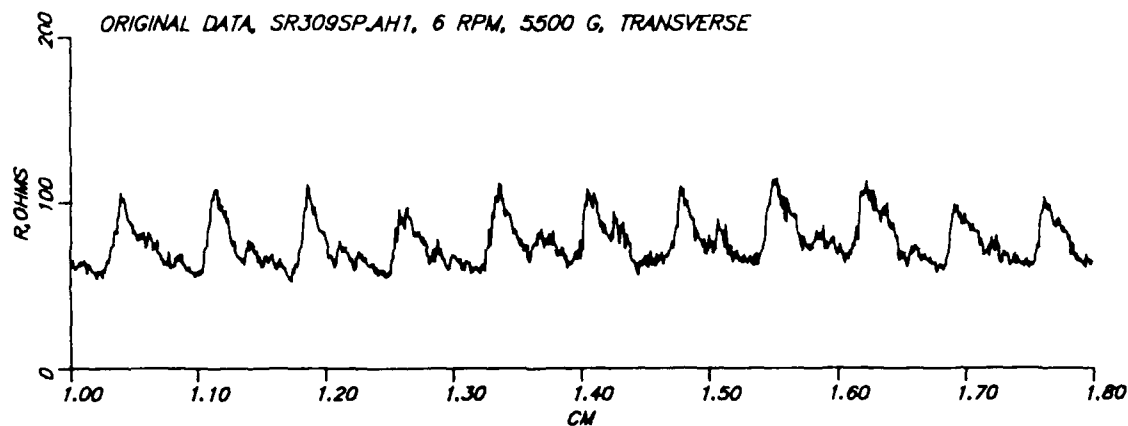
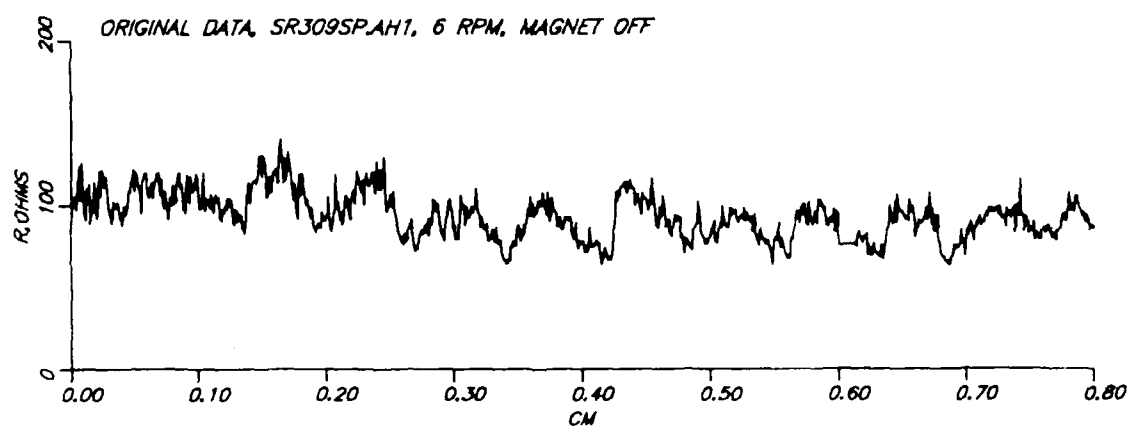


Figure 25. Spreading resistance data for the 6 rpm section of crystal Z309.

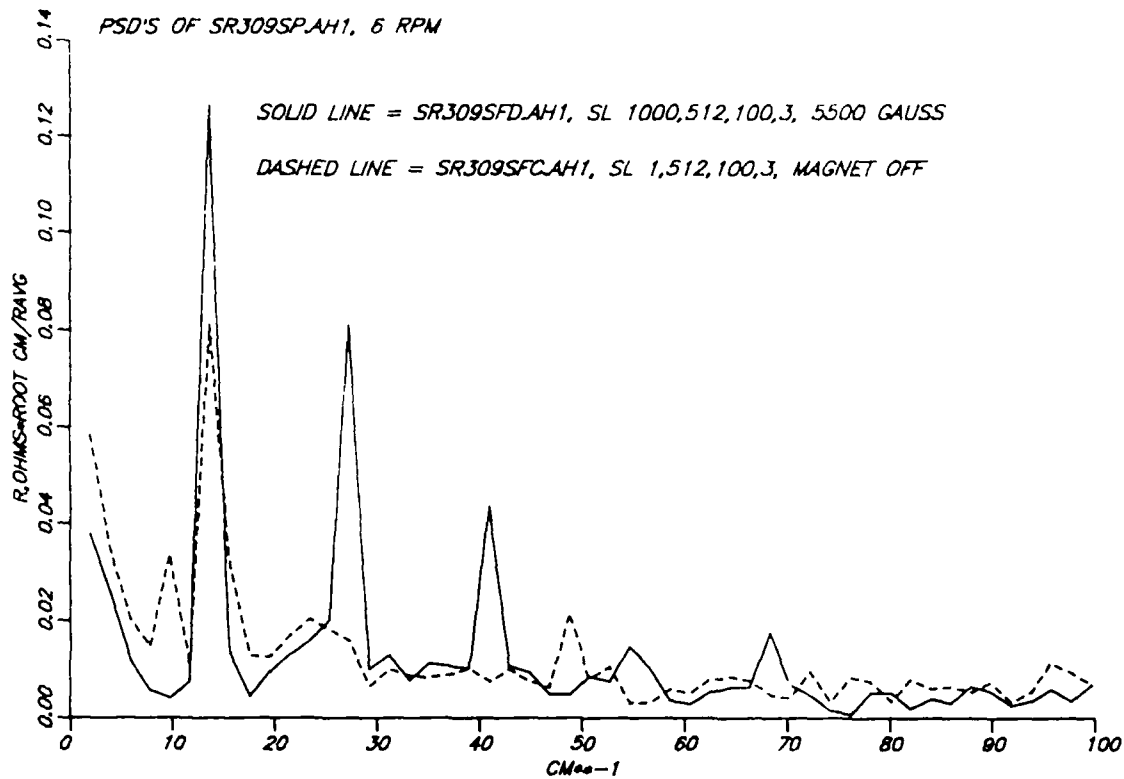


Figure 26. Power spectral densities for the magnet-on and -off regions of the 6 rpm section of crystal Z309.

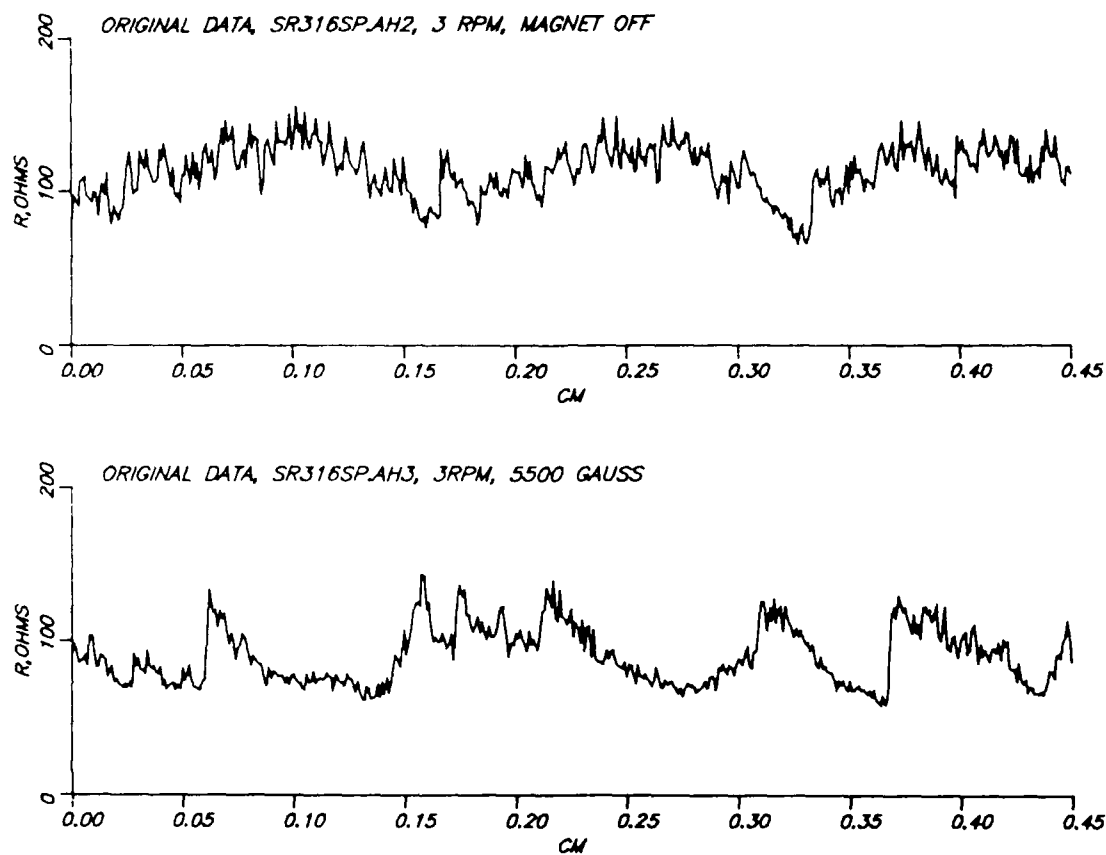


Figure 27. Spreading resistance data for the 3 rpm section of crystal Z316.

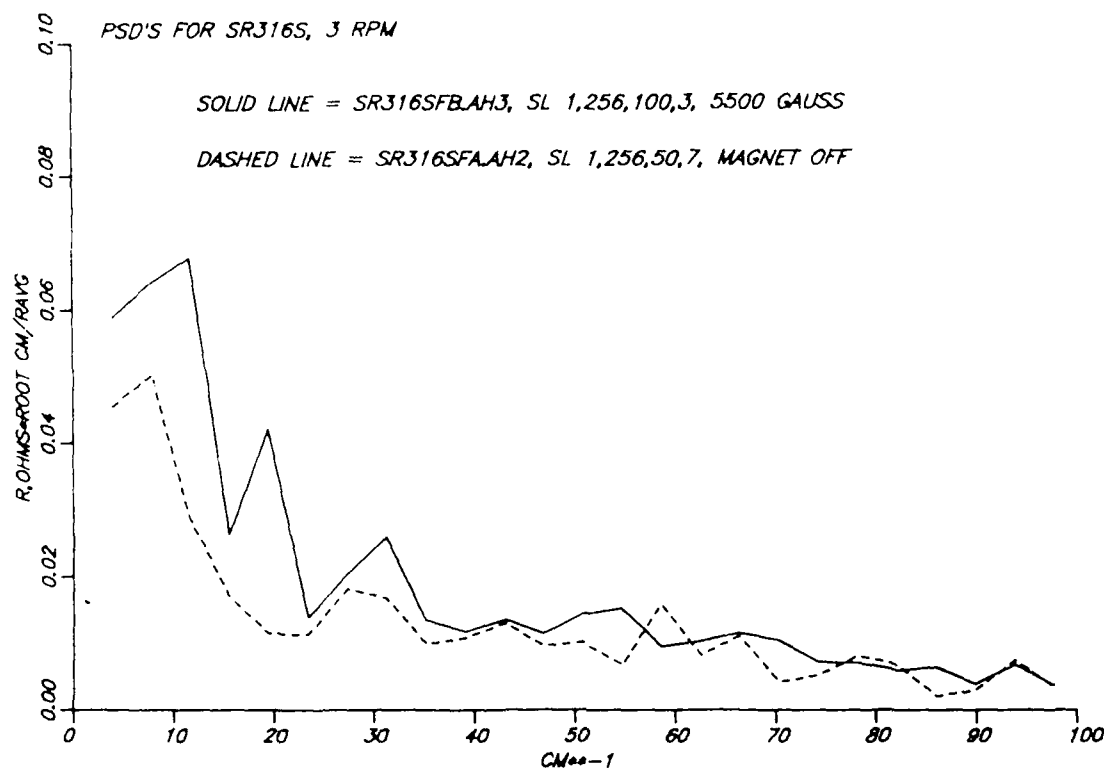


Figure 28. Power spectral densities of the magnet-on and -off regions of the 3 rpm section of crystal Z316.

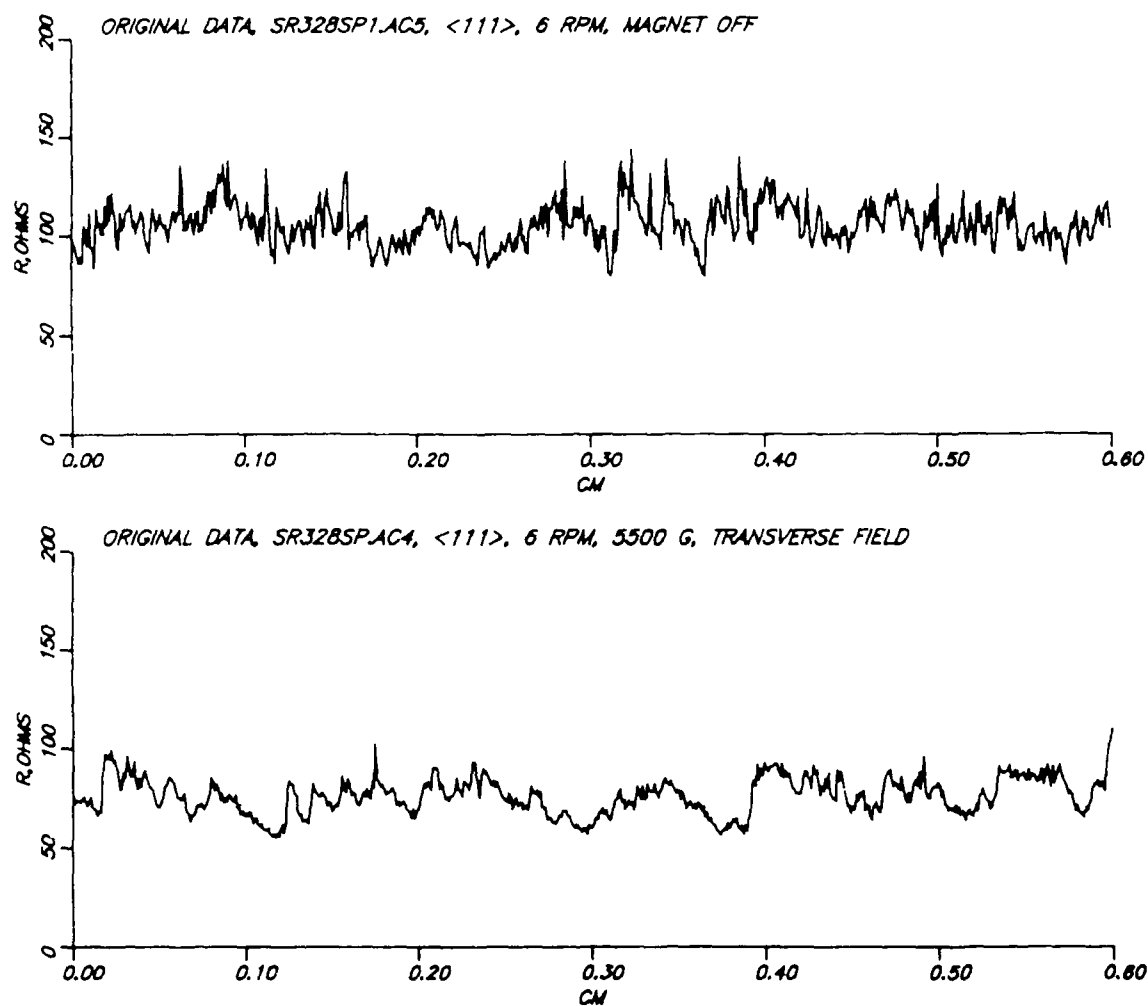


Figure 29. Spreading resistance for the 6 rpm section of crystal Z328<111>.

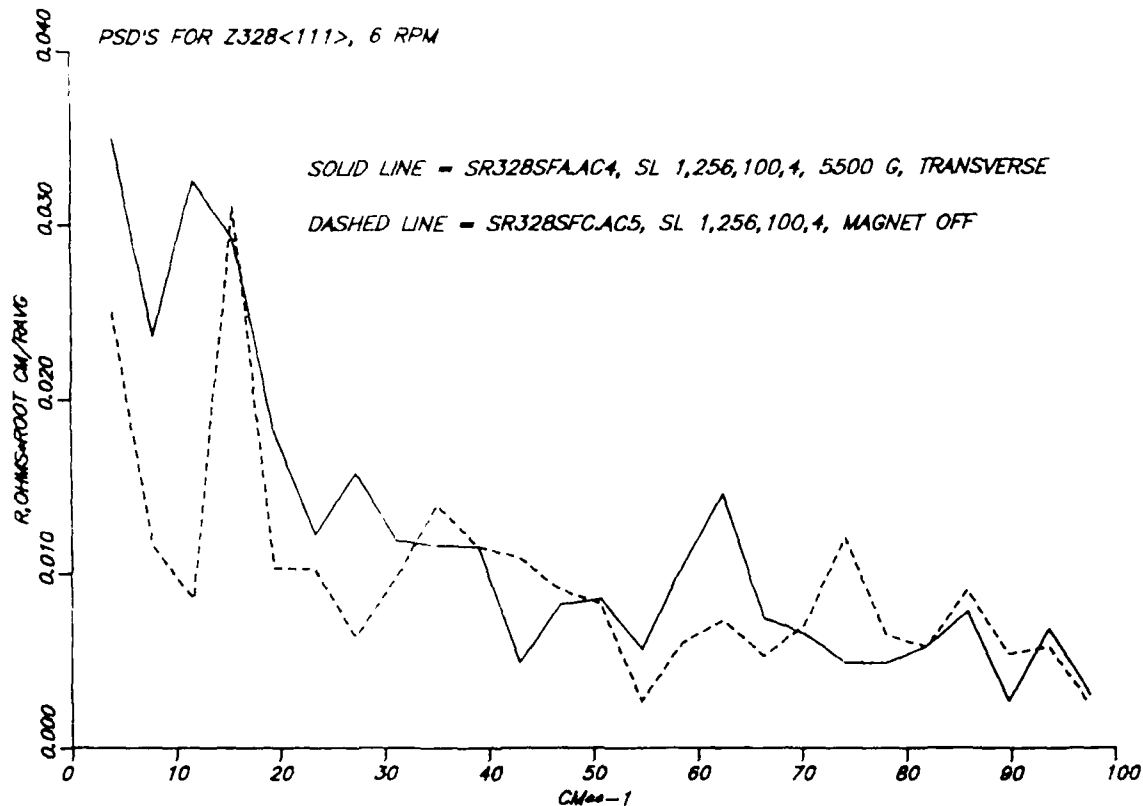


Figure 30. Power spectral densities for the magnet-on and -off regions of the 6 rpm section of crystal Z328<111>.

6 RPM, 4 mm/min, 5500 → 0 GAUSS

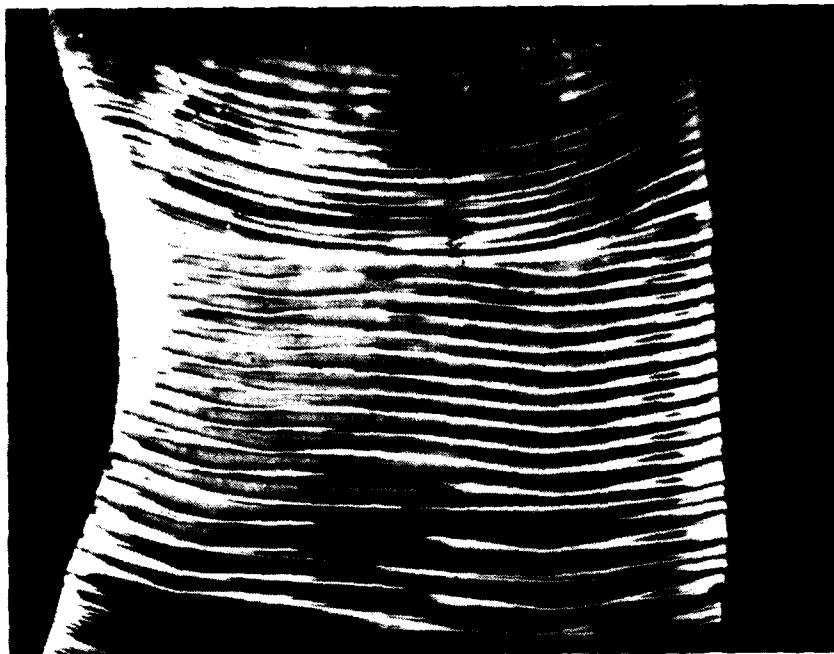


Figure 31. Striation etch pattern of the 6 rpm section of crystal Z328<111> from which the data of Figures 29 and 30 were obtained.

as much regularity as they do just after the field has been turned off. The return to steady state for the 6 rpm region of a $\langle 100 \rangle$ crystal (Z309) can be seen in Figure 19 to require about a dozen rotations. Unfortunately, crystal Z328 had to be terminated before this many rotations occurred.

The main reason for the change in rotational striae upon the application of the magnetic field is thought to be an alteration of the circulation patterns within the melt, perhaps due to the effective viscosity increase mentioned above. An increase in viscosity would reduce the Reynolds number and thus might bring the melt nearer to a laminar flow condition than it would be without the field. This would increase the diffusion boundary layer thickness as well and cause the increased dopant incorporation discussed above. Careful examination of the striation etch patterns in most of the photographs already presented show that differences in the "feathering" patterns arise when the magnetic field is applied. These may provide valuable clues to the oscillatory flows within the melt and thus should be the subject of future studies.

5. Alteration of Fine Striae

In addition to the rotational striations caused by the asymmetric rf energy input, there are other fluctuations in dopant concentration that occur on a much finer scale. Thus it is typical to find many fine striae located between the rotational striae. In earlier reports [1,2], the nature and origin of these fine striae have been discussed. They are likely due to local, or microscopic, variations in temperature, flow velocity, and dopant concentrations. They are often quite prominent in regions of "feathering" where local melt-back and regrowth are occurring. They are influenced by rotation of the crystal but are not dependent upon rotation for their existence. They should be very useful diagnostic indicators of fluid flow conditions, in the hands of a skilled hydrodynamicist.

The many striation etch patterns already shown suggest that when the magnetic field is on there are fewer fine striae. Certainly the change in visual appearance of the striation etch pattern represents some change in the character of the crystal. When we look at the spreading resistance data, however, we do not usually see a corresponding change in the high frequency components of the power spectral density, which should represent the higher spatial frequencies of the fine striae. For example, if the power spectral density data already shown for crystals Z309 and Z316 are extended into a higher frequency regime than was shown in Figures 24, 26, and 28, we do not find strong differences at the higher frequencies between the magnet-on and magnet-off conditions. Thus in Figures 32, 33, and 34 we do not detect any significant differences between the magnet-on and the magnet-off regions. These three comparisons have been made at a position halfway between the crystal axis and the edge of the crystal, because the striae are usually very well developed in this region. Often the striae patterns along the axis are disrupted by feathering patterns, as will be discussed more fully later. Nevertheless, for the on-axis scan of crystal Z309 in the 6 rpm section, we find some regular structure when the field is applied, as can be seen in Figure 35. In this case the striae corresponding to the 6 rpm rotation rate are clearly visible when the field is on and show up in the power spectral densities of Figure 36. At the higher frequencies corresponding to the fine striae, there is now a distinct difference in the power spectral densities, as seen in Figure 37. We find this same distinction in the on-axis scan on crystal Z328<111> given in Figure 38.

At this point, we do not have a complete picture of the behavior of the fine striae, nor of their origins. If the Reynolds number of the fluid melt has been decreased by the magnetic field, then one would expect that any turbulence in the

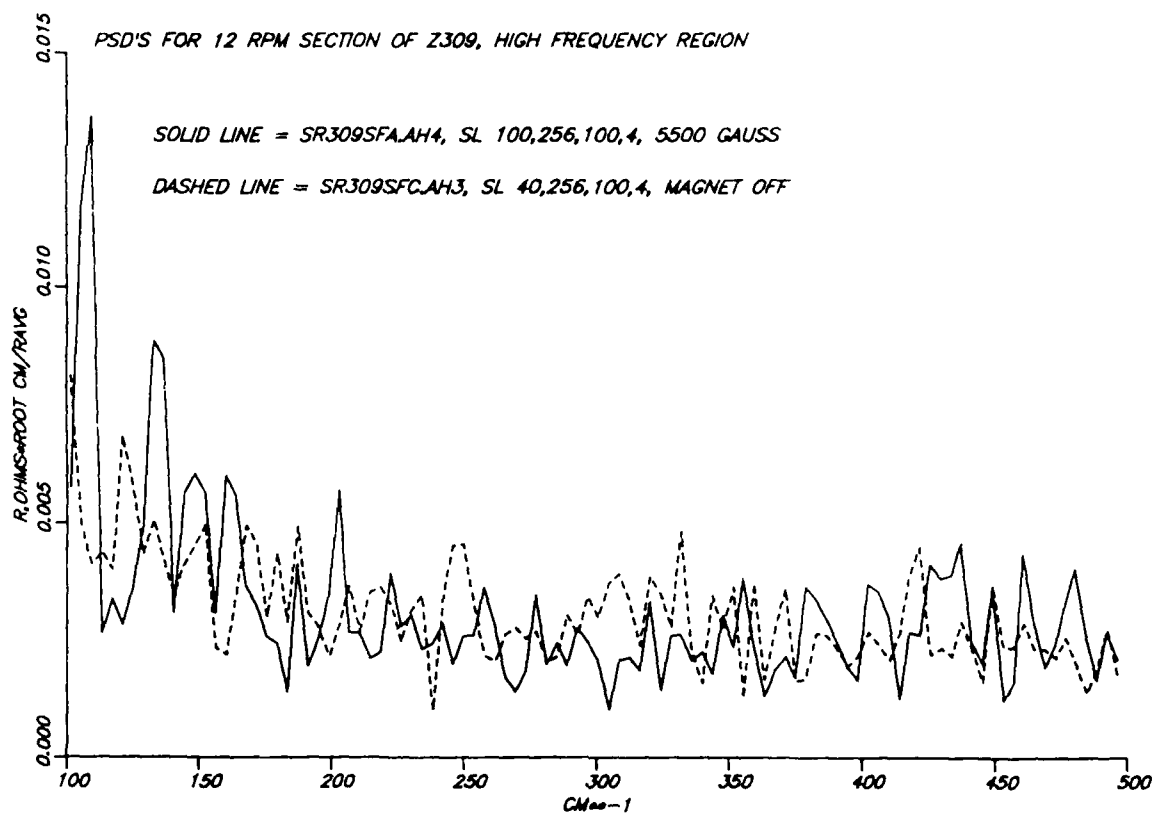


Figure 32. High frequency range of power spectral densities for the 12 rpm section of crystal Z309.

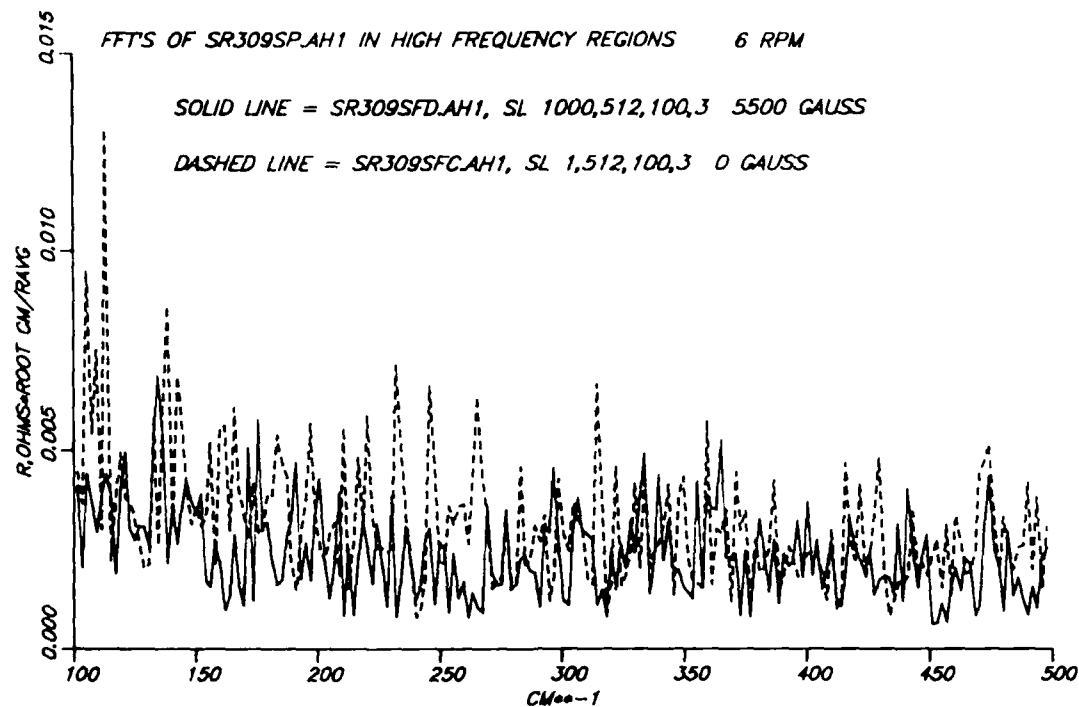


Figure 33. High frequency range of power spectral densities for the 6 rpm section of crystal Z309.

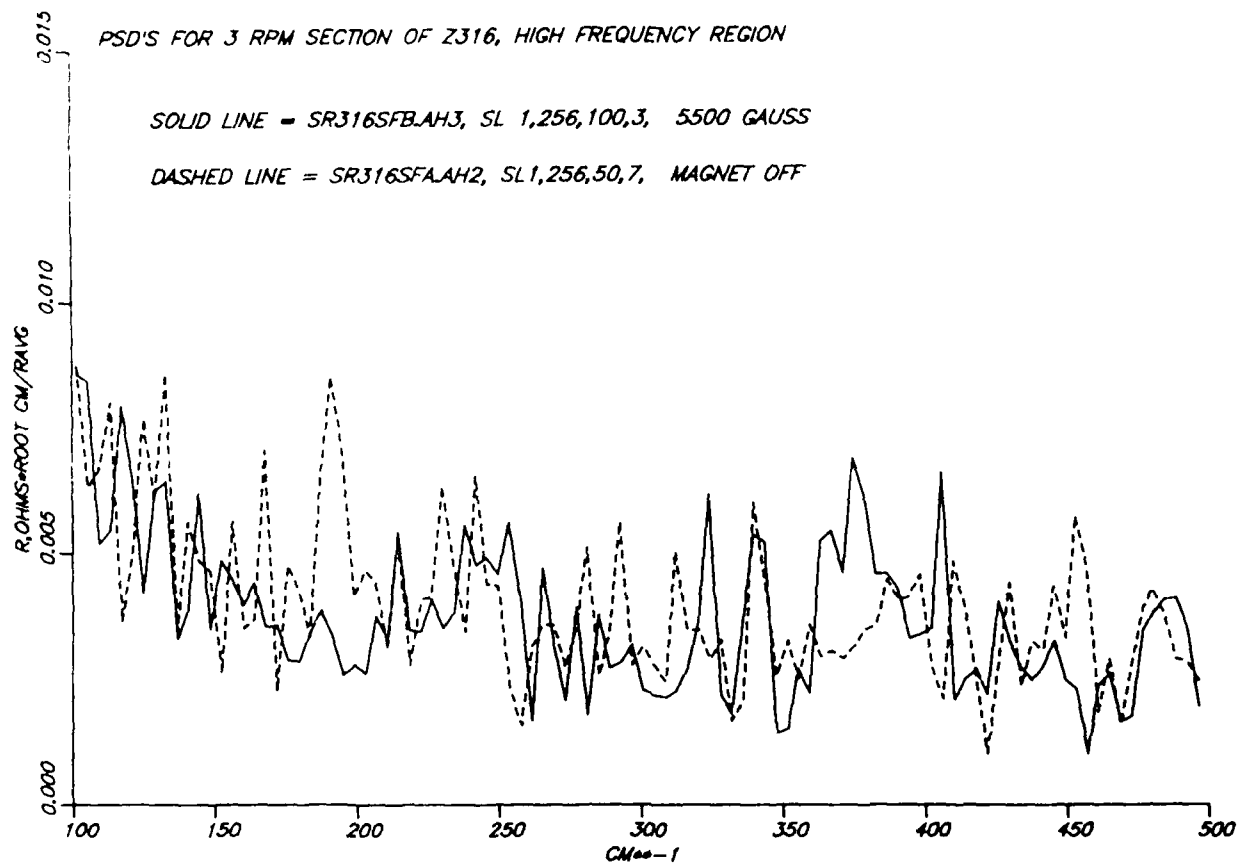


Figure 34. High frequency range of power spectral densities for the 3 rpm section of crystal Z316.

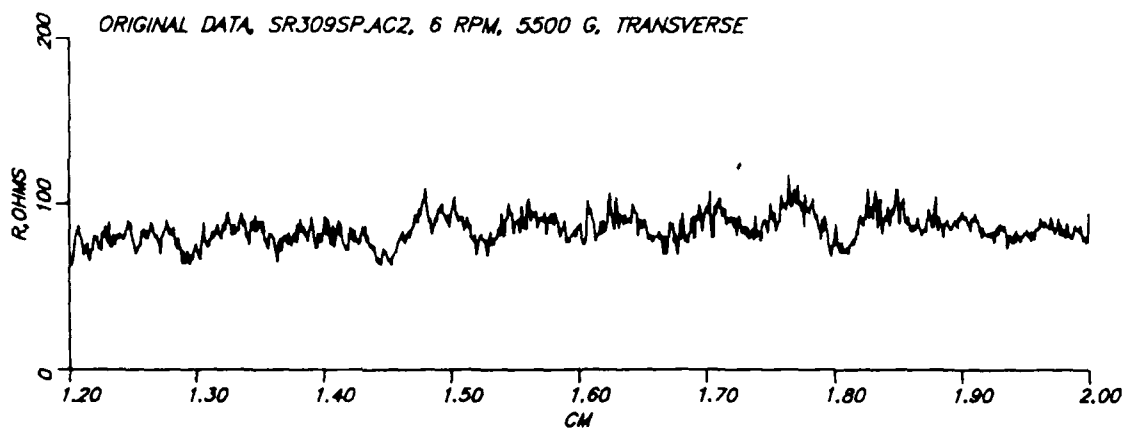
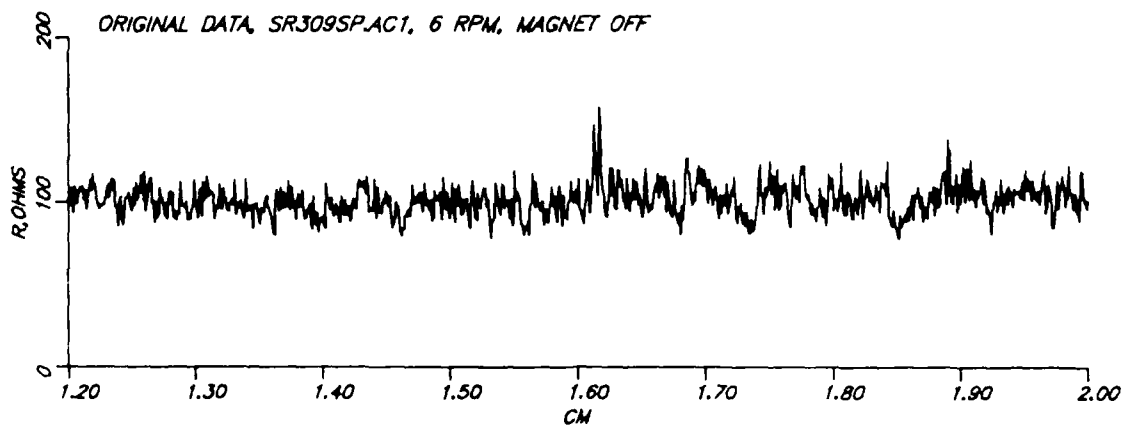


Figure 35. Spreading resistance data from on-axis scans of the 6 rpm section of crystal Z309.

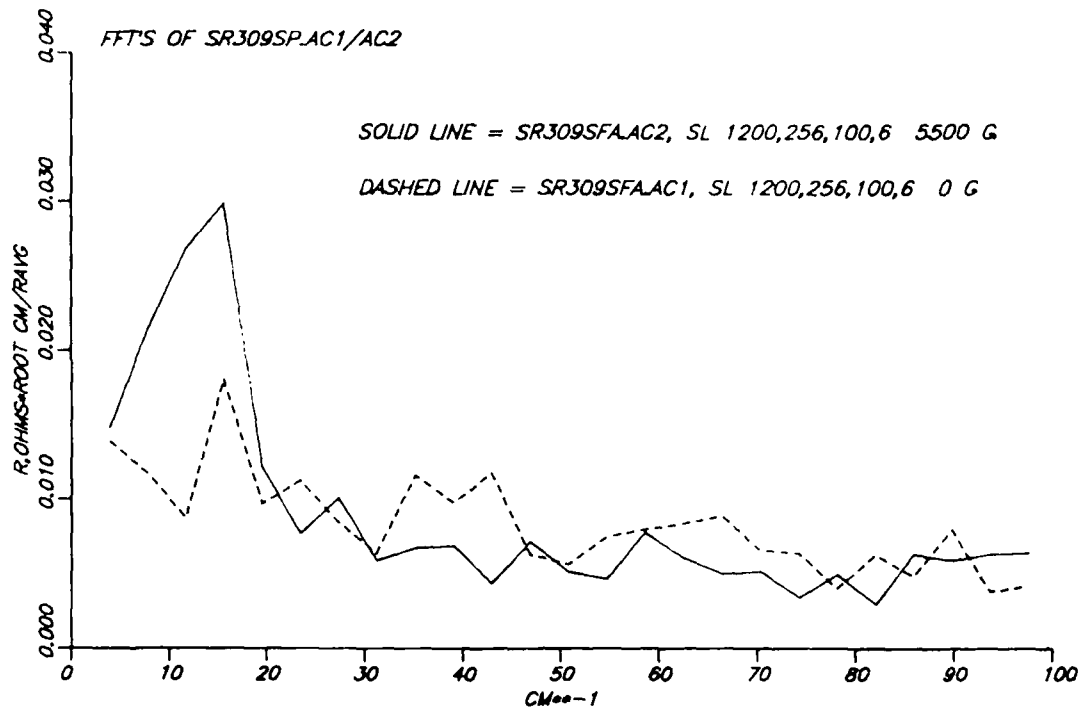


Figure 36. Power spectral densities for on-axis scans of the 6 rpm section of crystal Z309.

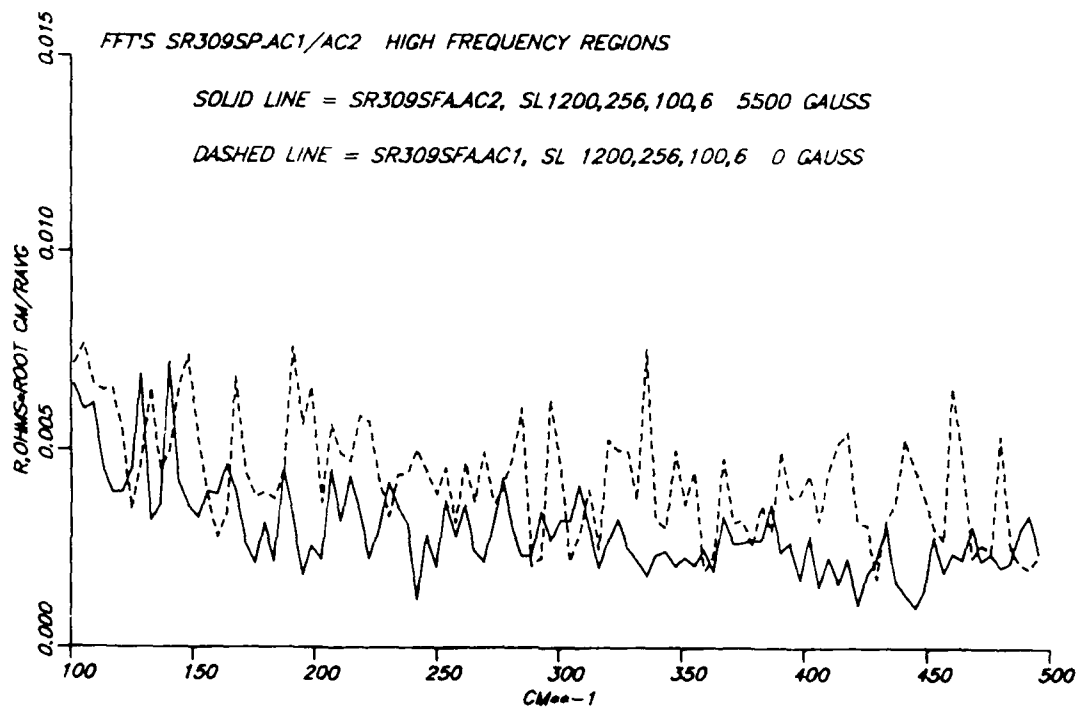


Figure 37. High frequency range of the power spectral densities of the on-axis scans in the 6 rpm section of crystal Z309.

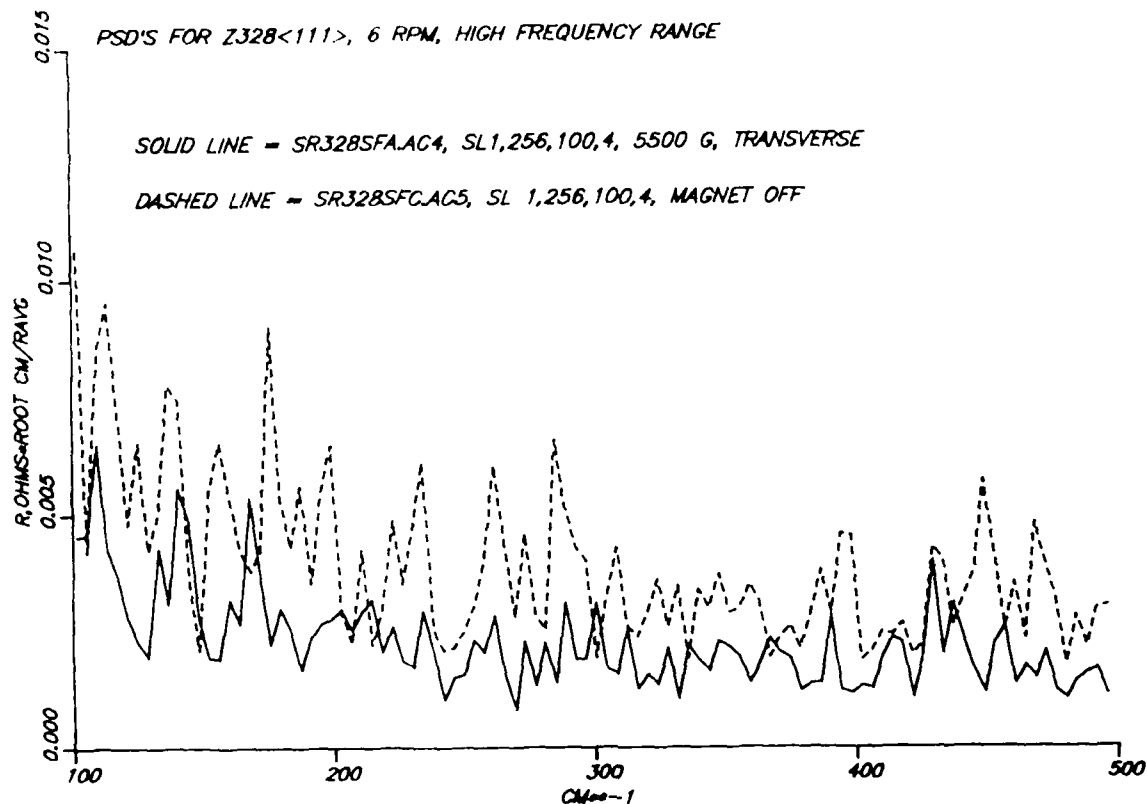


Figure 38. High frequency range of the power spectral densities of the on-axis scans in the 6 rpm region of crystal Z328 111 .

flow would also decrease, with a consequent reduction of the fluctuations in the microscopic growth rate. If temperature fluctuations have also been reduced by the field, as has been demonstrated in CZ growth [10,11], then one would expect the fine striae to be affected. If, on the other hand, some of the fine striae are due to concentration differences caused by non-uniform addition of undoped silicon to the circulating melt from the feed stock, then it is not so obvious what the effect of the field might be, because any reduction in turbulence will decrease the mixing of the melt region needed to homogenize the solute concentration.

For a good example of the visual appearance of striation etch patterns that suggest a reduction in fine striae with the application of the field, we can look at end cross sections of the crystal pieces which have been prepared for use in striation etching. These end faces have the same orientation as would the face of a wafer cut from the boule, although in this case the ends have not been polished. Nevertheless, they show interesting etch patterns. Figure 39 is from the 4 rpm section of crystal Z319 grown in the absence of a field. The pattern seen here typifies the dopant distribution in conventional float zone crystals and is a combination of both rotational and fine striae. When a 3100 G transverse field is present, this pattern changes to the one in Figure 40 in which the fine scale fluctuations appear to be greatly reduced in contrast to the minor effects seen in the spreading resistance data. However, more work needs to be done before the implications of the etch patterns and the results from spreading resistance can be reconciled.

14223-4

CRYSTAL Z319

4 RPM, 0 GAUSS

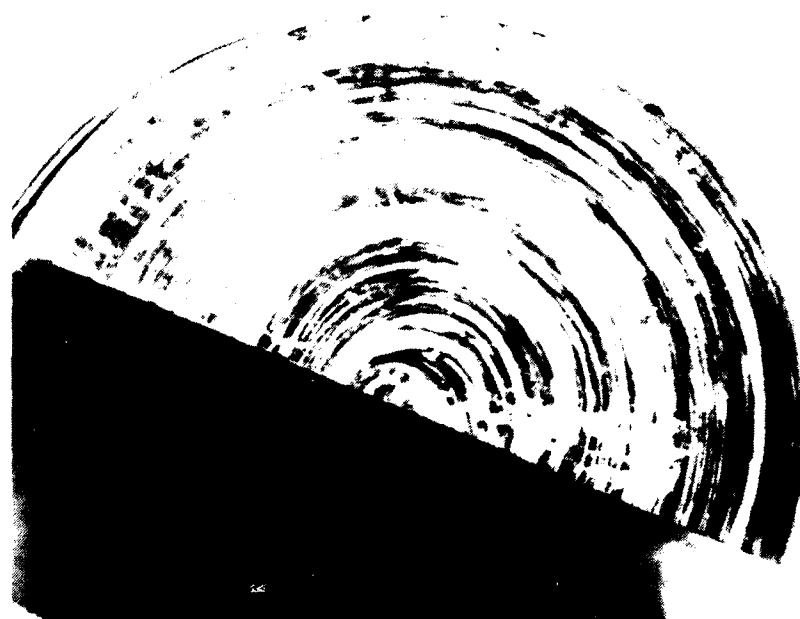


Figure 39. Striation etch pattern on an end surface from the 4 rpm section of crystal Z319, grown with the magnet off.

14223-1

CRYSTAL Z319

4 RPM, 3100 GAUSS



Figure 40. Striation etch pattern on an end surface of the 4 rpm section of crystal Z319 grown in a 3100 G transverse field.

B. NON-ROTATING CRYSTALS IN A TRANSVERSE FIELD

Many of the features already discussed for rotating crystals are also observed for non-rotating crystals, for example, the increase in dopant concentration when the field is applied, and alterations of the fine striae patterns. As would be expected, there are no rotational striae when there is no rotation. However, there are definitely some low frequency fluctuations, the nature of which is not yet clear, that impart many of the characteristics of slow rotation to the physical appearance of the crystals. The presence of transverse magnetic fields of several kilogauss intensity has produced effects which we believe have not been observed before and which should provide interesting challenges to those trying to model the float zone process. It is expected that the experimental opportunities afforded by the new magnet system, especially with non-rotating crystals, will advance the understanding of the float zone process and could well lead to methods for reducing dopant fluctuations. One interesting side benefit of the strong transverse magnetic fields is an apparent stabilization of the position of the growth axis for a non-rotating crystal, which might make possible the growth of detector-grade crystals without rotation. This behavior is in sharp contrast to that found with strong axial fields which may even have a destabilizing effect causing the axis to wander, as will be discussed later.

1. Crystal Morphology

Trial growths runs to establish techniques for controlling the non-rotating sections of crystals suggested that the shape of the non-rotating sections was slightly distorted from the normal circular cross section. Since it is commonly observed that when rotation ceases the crystal tends to wander almost randomly and often will not remain centered in the growth coil, these early observations were not considered unusual. However,

we decided to grow a long section in a 5500 G transverse field and then to reorient the crystal by 90 degrees relative to the field direction. The crystal that resulted proved to be the key to producing results never before seen, to the best of our knowledge. The novel feature of this crystal was the elliptical shape that it assumed as it grew and the apparent long term stability of this configuration. The major axis of the ellipse was oriented along the field direction and random wandering of the crystal was suppressed. When the seed was rotated by 90 degrees in the magnetic field, the growth was restabilized with the major axis of the elliptical cross section again oriented along the field direction. This run produced crystal Z321 with the interesting shape already shown in Figure 3. Subsequently we have grown four other crystals with this same configuration and have observed the stability of the melt zone in each one. Figure 41 shows crystal Z322, the second of these four crystals grown without rotation. As yet, the explanation of the elliptical cross section is not clear, but it likely is associated with the fact that the Lorentz force appears only for melt flowing in directions perpendicular to the field. Thus, circulation currents normal to the field direction are affected but those parallel to the field are not inhibited. The melt can now be thought of, perhaps, as a fluid with a non-isotropic viscosity. We will return to this issue later.

2. Growth Interface Shape

The exterior of the non-rotating sections of crystal Z322 exhibited the unexpected shape described above. When one looks at the striation etch patterns on cross sections prepared parallel and normal to the field direction, it becomes apparent that complex flow is occurring within the elliptically shaped melt volume. The details of this flow are still not well characterized but we will describe such results as are now available.

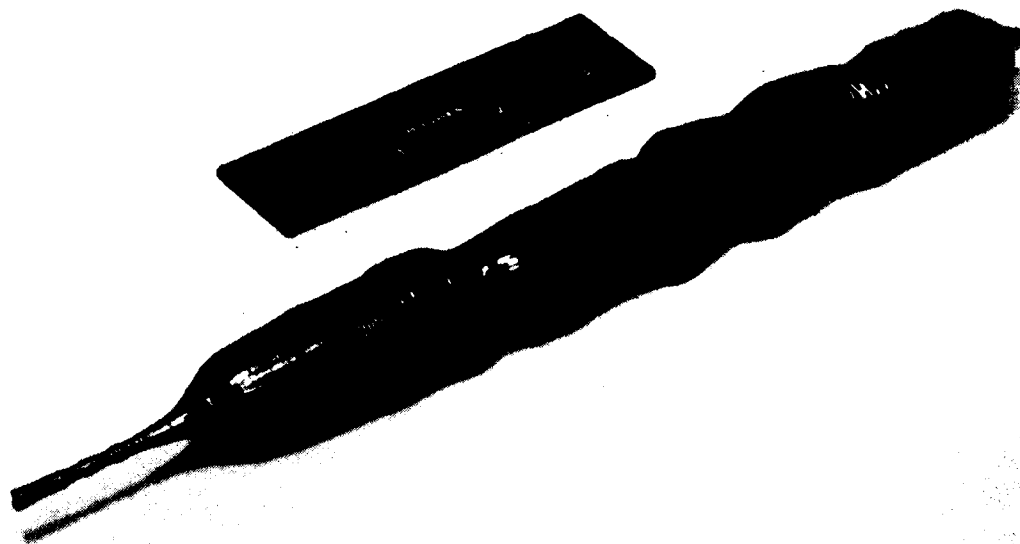


Figure 41. Crystal Z322 grown with no rotation in a 5500 G transverse field.

When the etched surface is parallel to the field direction, the striations are quite straight, implying a flat or nearly planar interface, in appearance not unlike those previously shown for the crystals grown with rotation. However, for sections cut normal to the field direction, the interface is strongly concave, similar to the rotating crystals when the magnet is off. Thus for the non-rotating sections in a transverse field, we have an interface shape which is cylindrical, rather than the nearly flat or the spherically curved surfaces normally found in FZ crystals.

Figure 42 shows the striation etch pattern in the transition region that occurred when the field was applied to the non-rotating portion of crystal Z322. The edge of the crystal is subjected to strong melt-back and the interface seems to flatten, similarly to what was seen in Figures 19 and 20. However, if we look at the striation etch pattern in the region of the 90 degree rotation, then we can see that, normal to the field, the interface shows considerable curvature. Figure 43 shows this transition region in crystal Z322 where the seed was rotated through a quarter turn. In the lower half of the photograph the field is parallel to the etched surface and in the upper half it is perpendicular to this surface. A similar transition for crystal Z328<111>, going from the perpendicular to the parallel field orientation, can be seen in Figure 44. The complex etch pattern seen in the lower curved section indicates that a very complicated circulation is taking place with pronounced "feathering." Why this feathering is not seen in the other orientation is not yet understood. We will discuss the implications of these patterns below.

3. Striation Characteristics

As with the rotating crystals described earlier, one would also expect changes in the fine structure of the striation patterns for the non-rotating sections of crystals. Strong

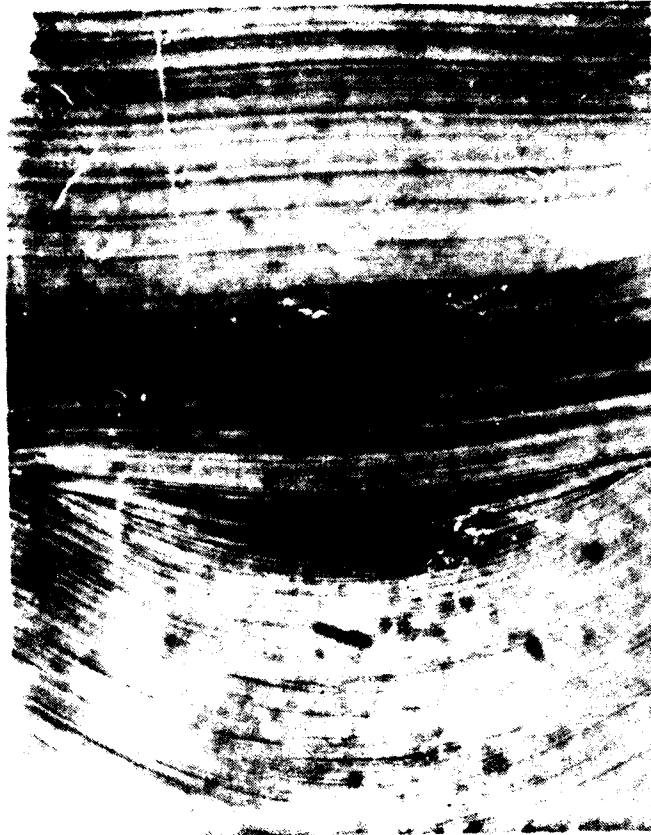


Figure 42. Striation etch pattern for non-rotating section of crystal Z322 showing the transition from 0 to 5500 gauss at 0 rpm.

14312-17

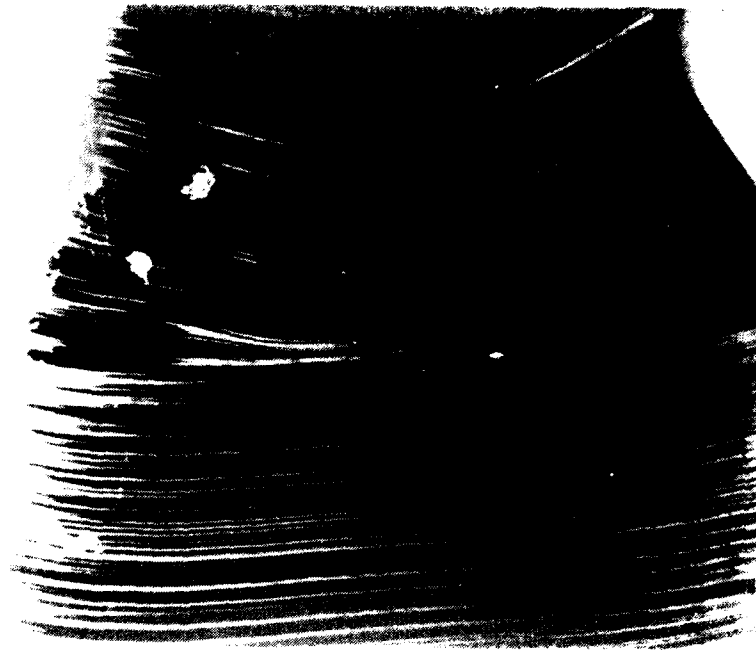


Figure 43. Striation etch pattern of the 90-degree rotation for crystal Z322 grown at 5500 G without rotation.



Figure 44. Striation etch pattern at the 90-degree rotation for crystal Z328 111 grown at 5500 G without rotation.

rotational striae ought to be absent and there should be distinct differences in the fine striae for the magnet-on and magnet-off conditions. Again, the visual appearance of the striation etch patterns indicates these expected differences, as can be seen by comparing Figures 45 and 46 obtained from crystal Z322. These photographs have a magnification of approximately 50X and reveal obvious differences in the appearance of the fine striae. The spreading resistance data for these two sections are given in Figure 47 along with a scan taken at 2 rpm, to which we will refer later. A comparison of the non-rotating sections shows the distinct shift in the resistance level that typically occurs when the field is applied, along with a higher fluctuation level when the magnet is off, but no obvious differences in the apparent frequency content of the two scans. The power spectral densities in this particular comparison, see Figure 48, indicate that the fluctuations in the magnet-on region are indeed less than those in the magnet-off region but only over a portion of the frequency spectrum. In an earlier crystal, Z292, grown in the tilted solenoid at about 900 G, the power spectral densities in the non-rotating sections also showed differences over a limited spectral range, as was noted previously for the data given in Figures 16 and 17. For crystal Z292 in the frequency range from about 20 to 50 cm^{-1} and at the specific frequencies of about 60 and 120 cm^{-1} , the two spectra are different. At higher frequencies there are no appreciable differences. For crystal Z322, grown at 5500 G, the region of spectral difference occurs at a higher frequency, between about 100 and 300 cm^{-1} . At present we have not collected enough data to determine if there is a consistent field strength dependence for these spectral differences. It should be noted that, in Figures 17, 48 and 49, the actual power levels in the spectra are relatively low over the entire frequency range in comparison to those normally seen for rotating sections of crystals. Such

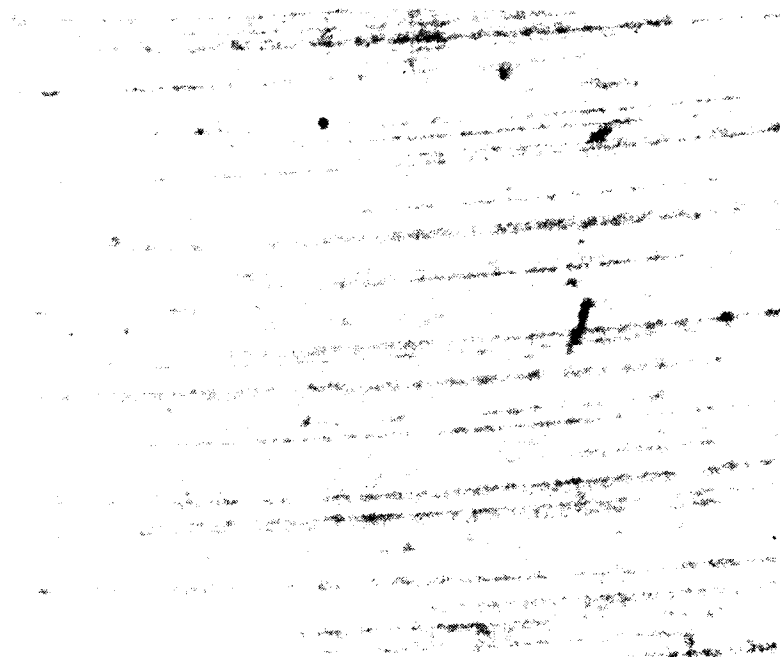


Figure 45. Striation etch pattern for non-rotating section of crystal Z322 grown with magnet off.

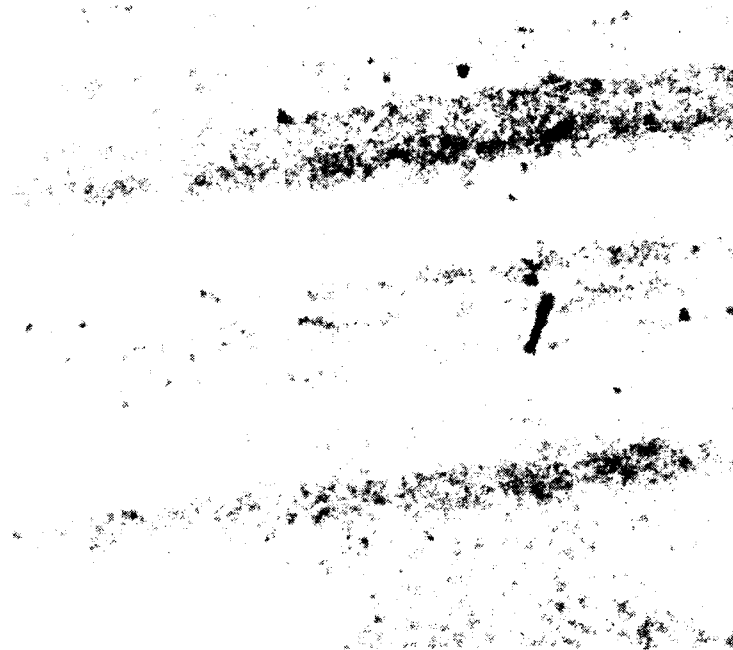


Figure 46. Striation etch pattern for non-rotating section of crystal Z322 grown in a 5500 G transverse field.

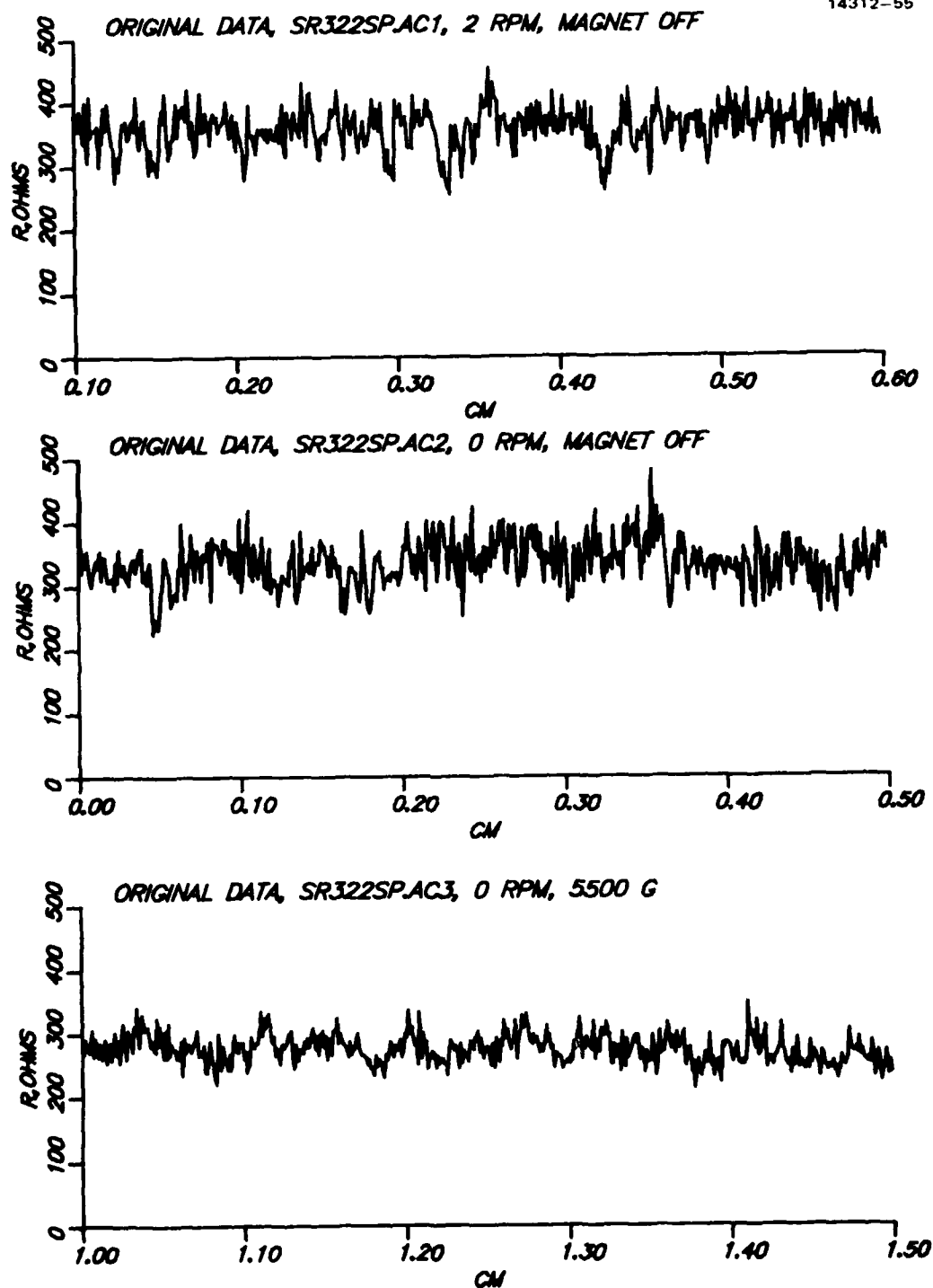


Figure 47. Spreading resistance data for various regions of crystal Z322.

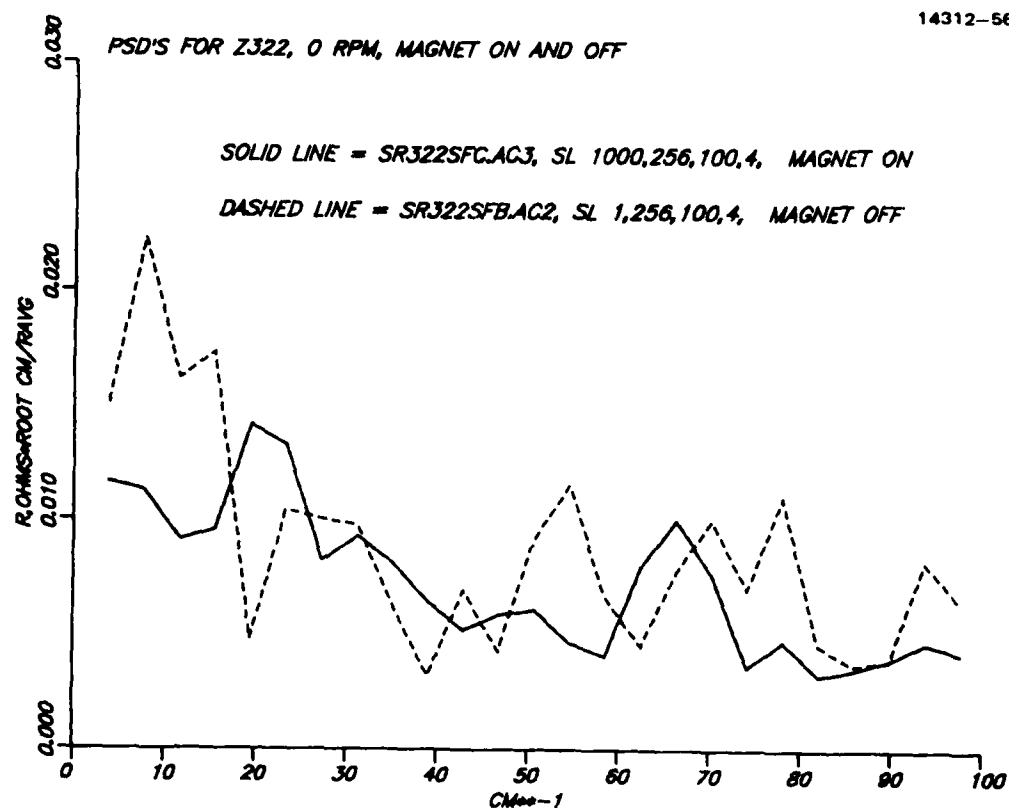


Figure 48. Power spectral densities for the non-rotating section of crystal Z322, low frequency range.

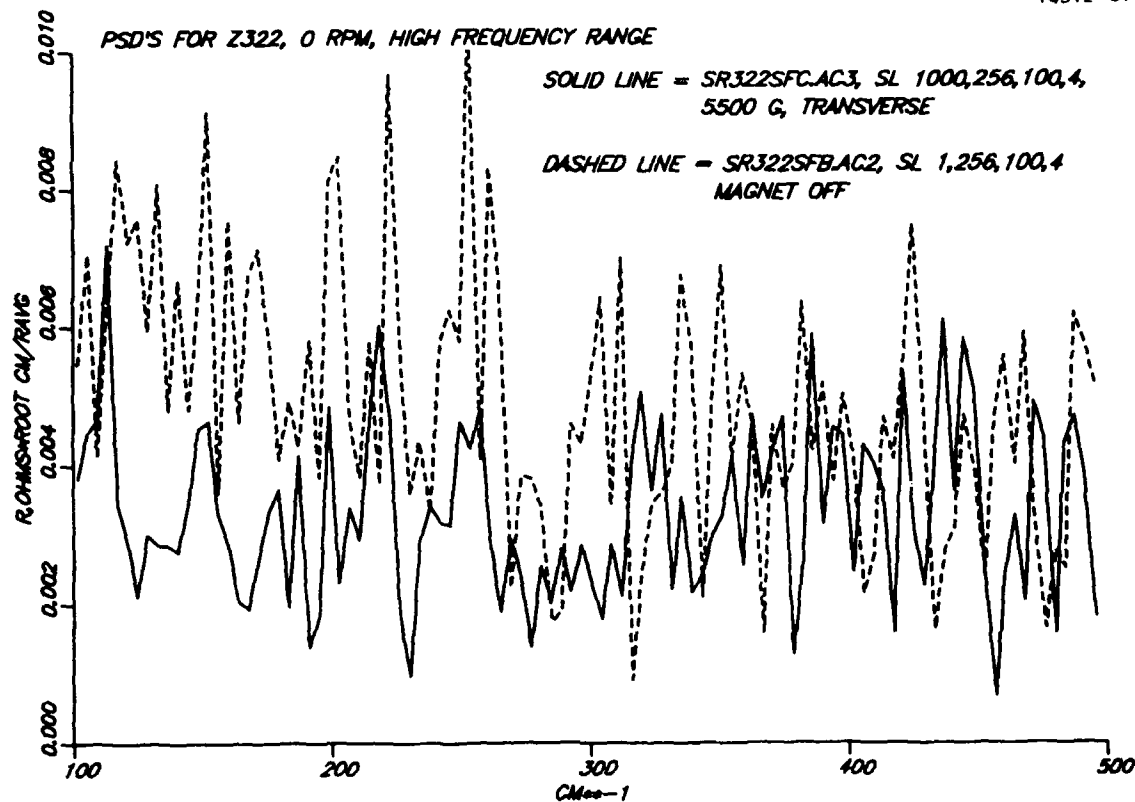


Figure 49. Power spectral densities for the non-rotating section of crystal Z322, high frequency range.

non-rotating crystal sections need to be explored more fully because they may yield characterizations of the turbulence spectra of the melt flow that have been previously unavailable [14].

We have only one end section pattern, similar to those of Figures 39 and 40, for a non-rotating section with the field on. This pattern shows, in Figure 50, a reduction in the number of fine striae as well as the elliptical cross section typical of the transverse field condition with no crystal rotation. This pattern strongly suggests that an oscillatory flow is present, as will be discussed below.

Because the crystal is not rotating, one would expect only fine striae to be present in the etch patterns. It is apparent from Figures 42, 43, and especially 44 that in addition to the fine striae the patterns contain a low frequency structure whose nature is not yet understood. It is postulated that this structure, with its relatively long periods of 20 to 30 sec, may represent low frequency oscillations in the melt following a pattern similar to those discussed by Schwabe and co-workers [15,16], and Chun and Wuest [17-21] for oscillatory Marangoni flow. While it appears that, for our experimental set-up, Marangoni flow is not important compared to the flow driven by the electrodynamic force [12], oscillatory instabilities may well be present and their frequency would be influenced by the "viscosity effect" of the magnetic field.

To ascertain if the low frequency oscillation was being driven by the slow rotation of the feed rod commonly used to prevent uneven melting of the feed material, we grew sections of crystal Z322 with no seed rotation and with the top feed rod stationary or rotating at a nominal rate of 1.5 rpm, a commonly used value in our experiments. The spreading resistance data for scans in these two regions are given in Figure 51. The power spectral densities for these regions show distinct

AD-A155 730

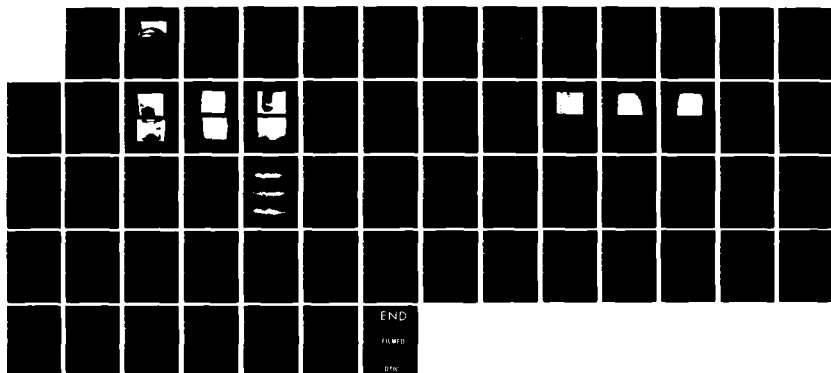
STRIATION FREE DOPED SILICON(U) HUGHES RESEARCH LABS
MALIBU CA G D ROBERTSON DEC 84 AFMAL-TR-84-4156
F33615-81-C-5065

272

UNCLASSIFIED

F/G 20/2

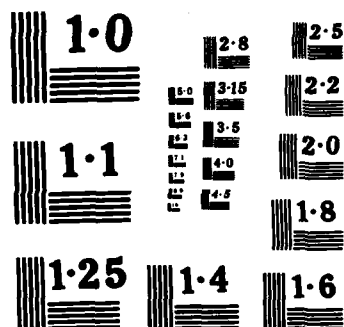
NL



END

FILMED

DTN



NATIONAL BUREAU OF STANDARDS
MICROCOPY RESOLUTION TEST CHART



Figure 50. Striation etch pattern of an end surface from a non-rotating section of crystal 2322 grown with a 5500 G transverse field.

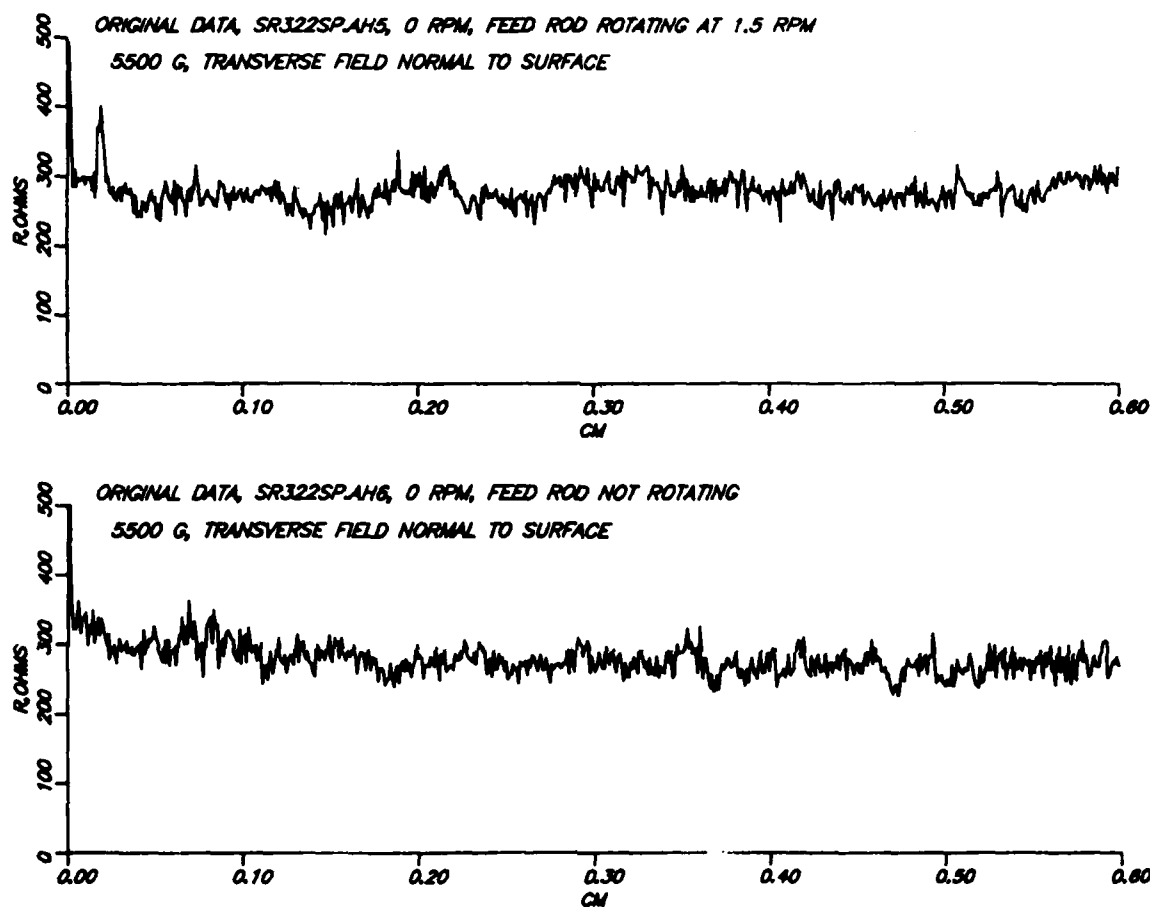


Figure 51. Spreading resistance data for the non-rotating section of crystal Z322 for different feed rod rotations.

differences in the low frequency range, as can be seen in Figure 52. Above a frequency of 50 cm^{-1} , there are no observable differences in the spectra. The scans for Figure 51 were taken in an axial direction at a position half way between the edge and the crystal axis, in a region that often shows strong striae. If the scans are taken along the growth axis, then for these same sections of the crystal we see somewhat different behavior. Figure 53 shows the spreading resistance data for the on-axis scans. In this case, the power spectral densities are different over the entire frequency range, as presented in Figures 54 and 55. As yet we have not acquired enough data of the type represented by Figures 51 through 55 to understand all the implications of the results or to be able to sort out cause and effect relationships. The low frequencies that appear to be enhanced when the feed rod is rotating could be caused by some characteristic of the feed rod itself or they may be related to vibrational frequencies set up in the furnace when the top shaft is rotating. More experiments are needed to resolve such issues. We have given these data here as another illustration of the power of the FFT spectral analysis technique to reveal differences in spreading resistance data which would perhaps escape visual comparisons. We believe that Figure 5-34 is an excellent example of data in which the oscillation at the frequency of 4 cm^{-1} , corresponding to the 1.5 rotation rate, would not otherwise be detected. Use of this method of data analysis, especially for non-rotating crystals, should help unravel the causes of low frequency oscillations which in rotating crystals are normally masked by stronger striae.

4. Boundary Layer Thickness Changes

As with the rotating crystals discussed earlier, we also see an increase in dopant concentration when the magnetic field is applied which we attribute to an increase in boundary layer thickness. A good example comes from the data already shown in

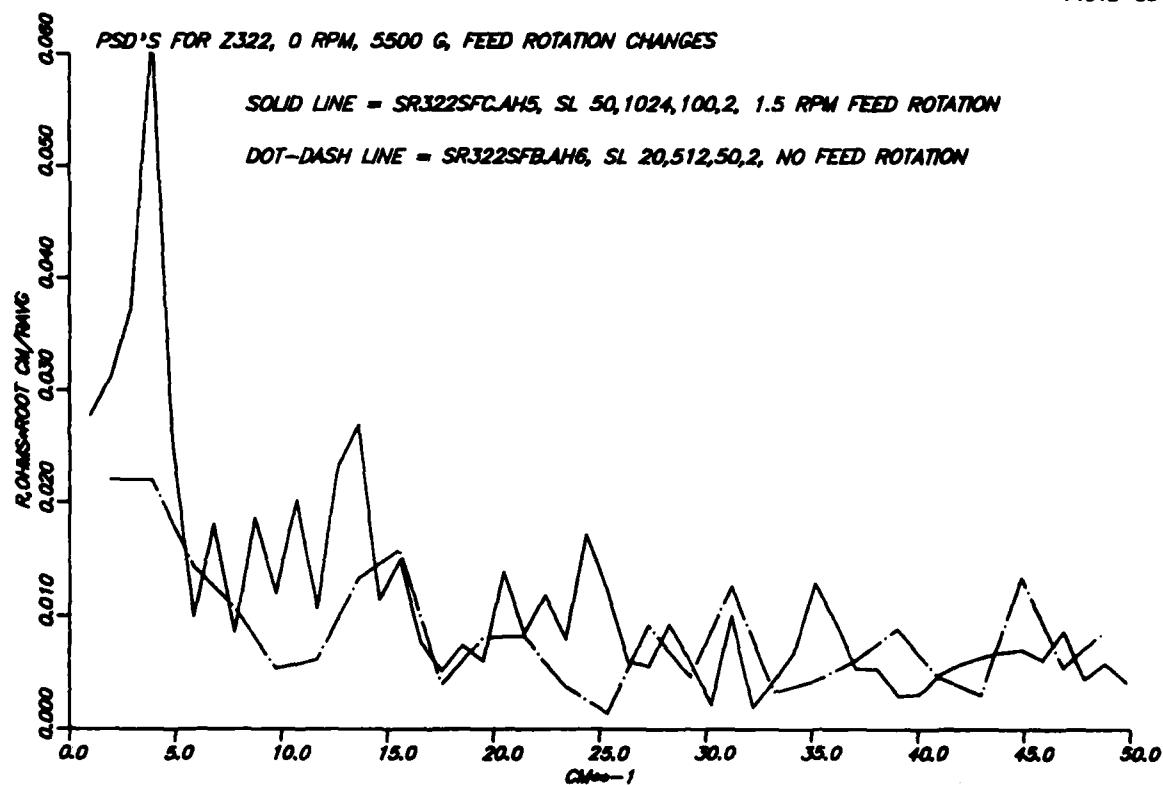


Figure 52. Power spectral densities for the non-rotating section of crystal Z322 with different feed rod rotations.

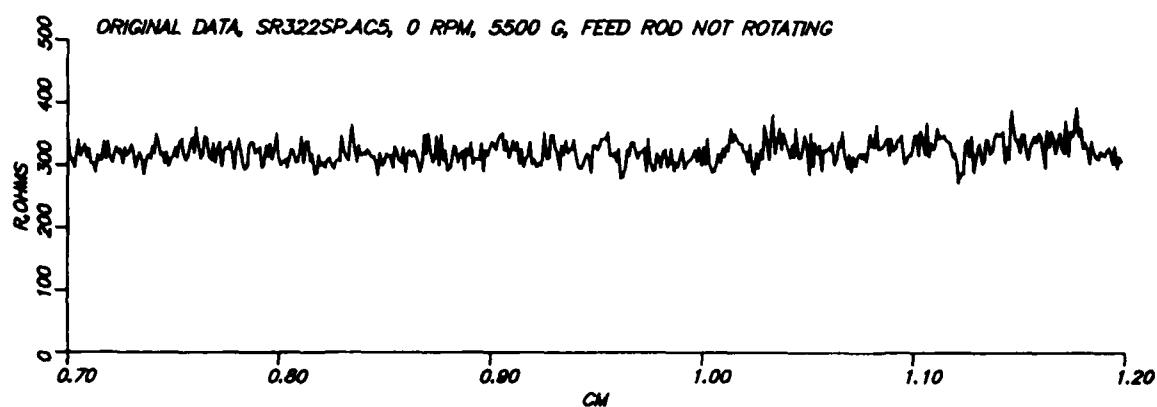
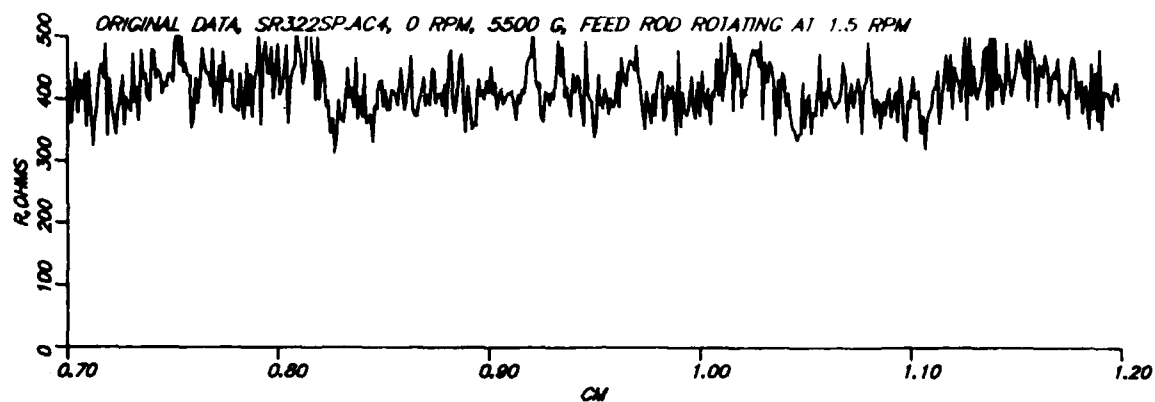


Figure 53. Spreading resistance data along the axis of the non-rotating section of crystal Z322 for different feed rod rotations.

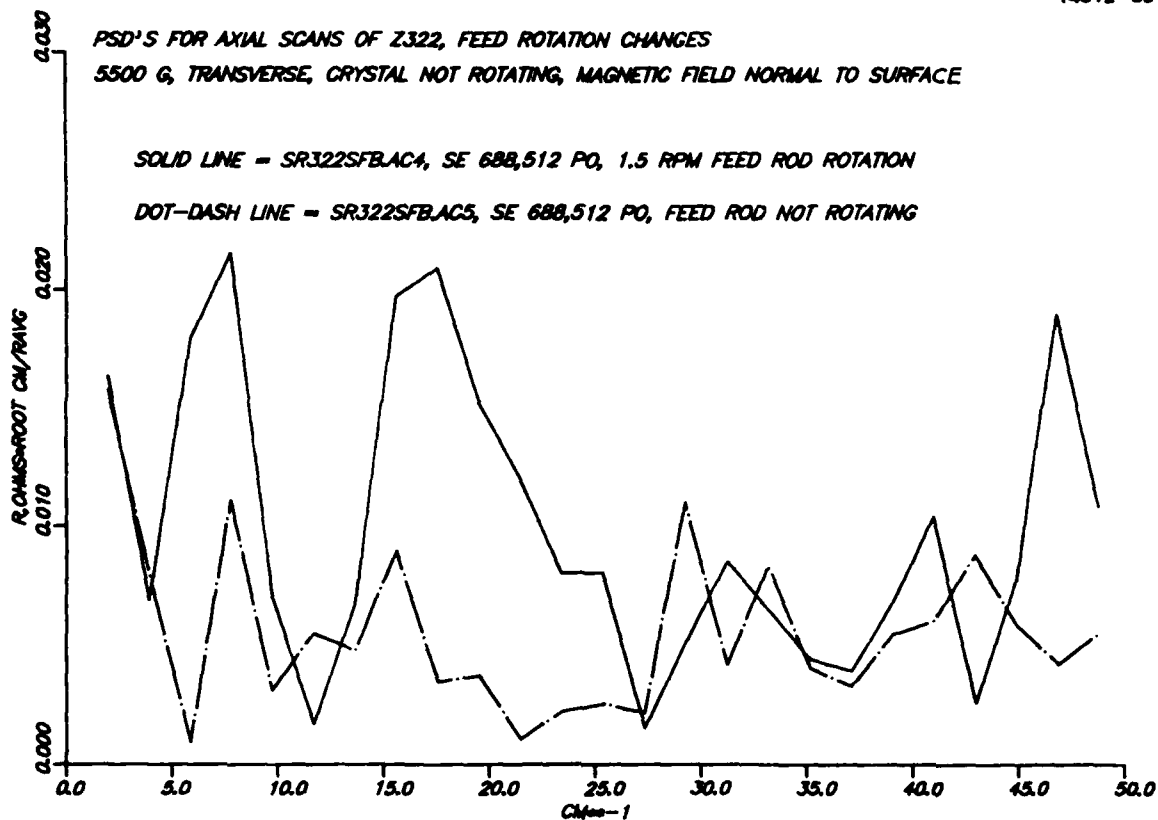


Figure 54. Low frequency range power spectral density for the on-axis scan of crystal Z322 for different feed rod rotations.

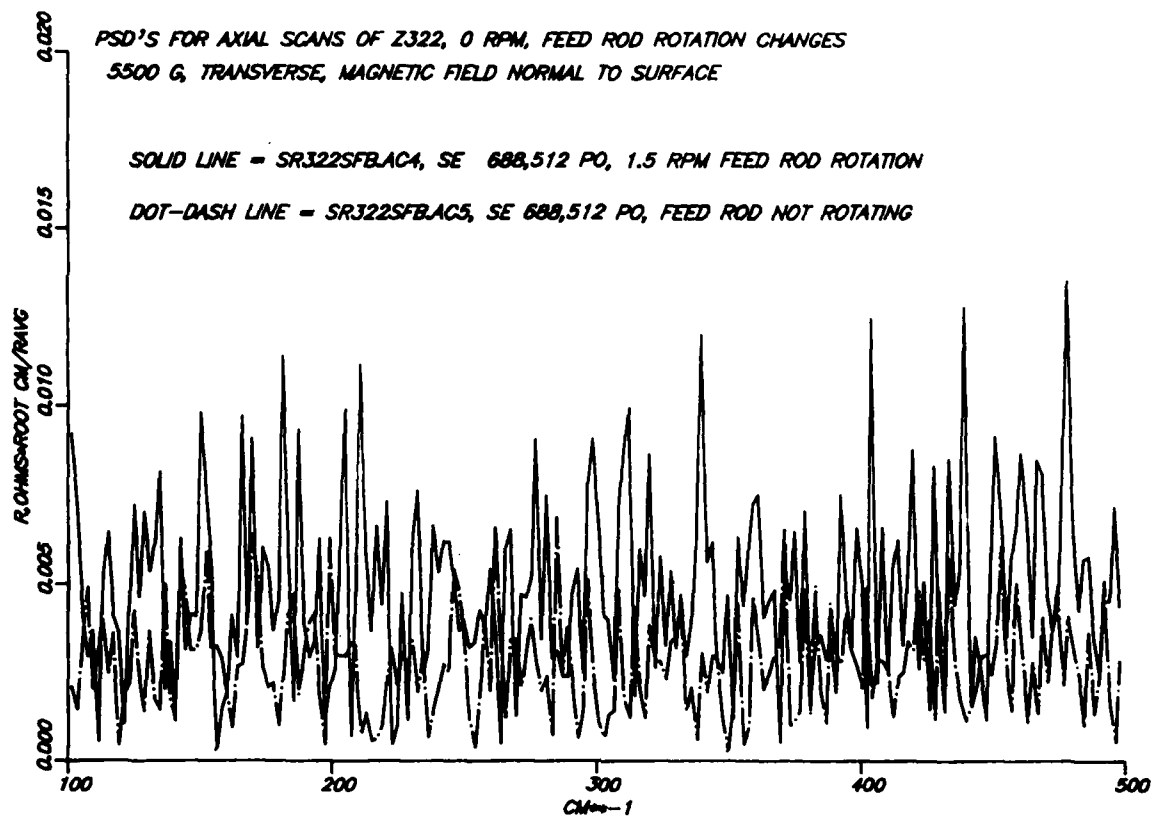


Figure 55. High frequency range of power spectral densities for the on-axis scan of crystal Z322 for different feed rod rotations.

Figure 47 for crystal Z322. Here one can see a decrease in average spreading resistance in going from 2 rpm to 0 rpm with the magnet off, as would be expected, and a further decrease when the field is applied to the 0 rpm section. In Table 6, the average values of the spreading resistance calculated from the data stored in the computer confirm the levels shifts easily seen in Figure 47. Thus the magnetic field appears to increase the boundary layer thickness even when the crystal is not rotating. This observation is compatible with the "viscosity increase" discussed above, although the actual explanation may be more complicated.

The fluctuation levels in the data, as indicated by the relative standard deviation, show a small improvement when the field is applied to the non-rotating section, but the resulting level of fluctuation is no less than that found in the 2 rpm section when the field is off. These data are consistent with the results from other crystals indicating that the presence of a strong transverse magnetic field does not remove growth striae but only seems to alter their character.

Table 6. Resistance and Fluctuation
Level Changes for the
Sections of Crystal Z322.

14312-49

FILE NAME	POINT NOS.	R, AV. Ω	SD Ω	REL SD %	RPM	MAGNET CONDITION
SR322SP.AC1	100-600	358.3	31.36	8.75	2	OFF
SR322SP.AC2	1-500	333.1	36.36	10.92	0	OFF
SR322SP.AC3	1000-1600	272.4	22.92	8.41	0	ON

C. CRYSTALS GROWN IN AN AXIAL FIELD

The first crystal grown with the external magnet system used an axial field orientation because this configuration appeared easiest for the crystal grower while trying to master the techniques needed for the relocated rf work coil. This crystal (Z311) was relatively easy to grow in a field of 3200 G. The magnet configuration was then shifted to the transverse configuration for what was expected to be very rewarding experiments. As seen in the previous section, interesting results were indeed achieved with the 12 crystals grown in strong transverse magnetic fields. Toward the end of the experimental program, the magnet was returned to the axial field configuration and four more crystals were grown for analysis along with three crystals for delivery to the Sponsor. These have provided surprising results which for the first time hold the promise for substantially reduced dopant fluctuations. For convenience of presentation, we have focussed the discussion on the three key issues of dopant distribution, fluctuation reductions, and crystal growth behavior. These will also serve to highlight the important differences between axial and transverse field orientations.

1. Dopant Distribution

As noted earlier in Tables 2 and 4, the dopant concentration increases when a strong transverse field is applied. This increase appears over the entire growth surface and we attribute this effect to a general thickening of the boundary layer caused by restricted flow in the melt. An analogous effect does not occur upon application of a strong axial field. Rather, there appear to be localized changes in boundary layer thickness caused by a change in the circulation flow pattern within the melt zone. This flow modification leads to a phenomenon which has many of the characteristics of "core" formation, seen when facet growth is possible [22], and because

of this similarity in properties we will refer to this behavior as "coring" even though we do not believe the mechanism is in any way related to faceting. The presence of a core was seen but not recognized as significant in the striation etch patterns for crystal Z311, the first one grown in the strong field of the external magnet system. When additional axial field crystals were analyzed, the presence of the core was found to be a general characteristic of these crystals and was present at all rotation rates from 0 to 12 rpm, the present limits of our furnace. The dopant concentration in the core has been consistently higher than in the off-core regions and often results in a very colorful striation etch pattern. We have taken several radial spreading resistance scans across crystal diameters in these regions and find significant results. Figures 56 and 57 show typical variations in dopant concentration, as revealed by these spreading resistance scans taken across diameters in both rotating and non-rotating sections grown in various field strengths. The distance along the abscissa is about 2 cm for each scan. The ordinate scale of resistance amplitude is logarithmic to allow comparisons of the relative changes contained in the various sets of data. Each scan has a different absolute resistance, the actual value depending upon the dopant added by the crystal grower. Since some of the resistances overlap, the curves have been arbitrarily displaced in the figures for ease of viewing. No attempt was made to achieve the same dopant concentration in each crystal, although most crystals fall in the range from mid 10^{16} to mid 10^{17} Ga/cm³, since this doping level leads to good striation etch patterns. These data do not show a consistent trend towards more dopant in the core with a higher field strength; but the reduction in fluctuation level with increased field strength is obvious and will be discussed below.

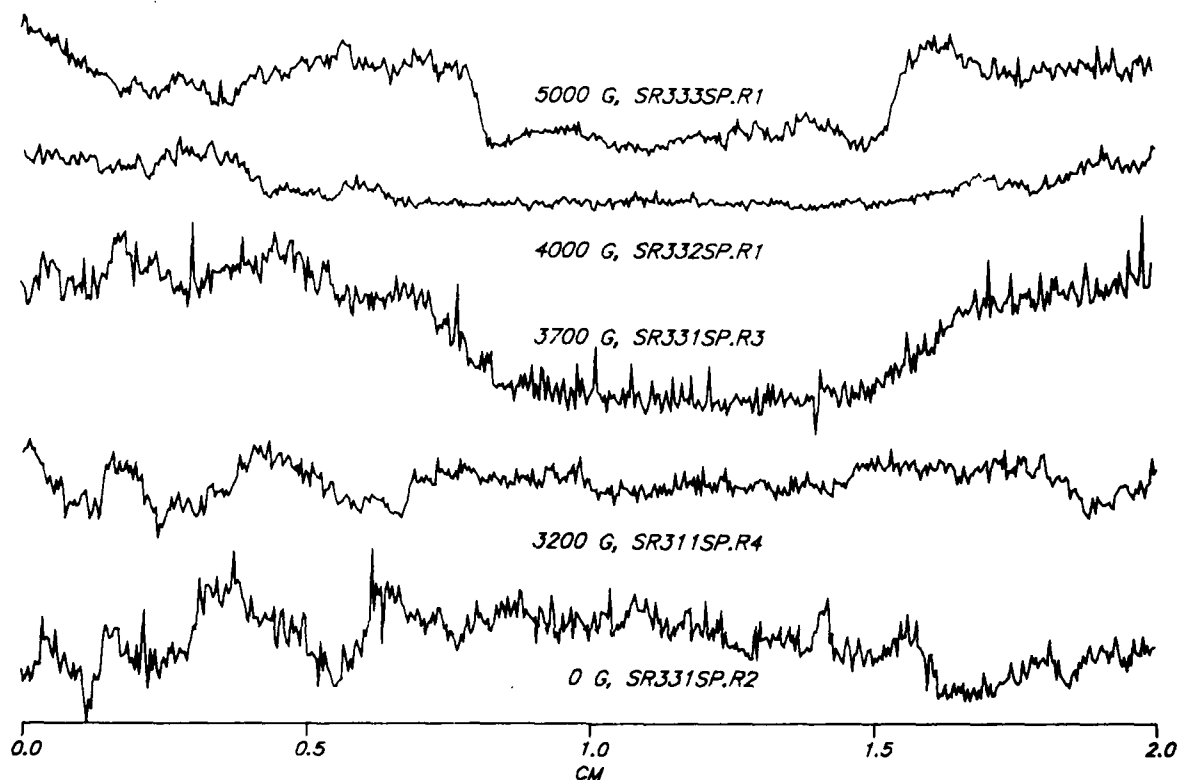


Figure 56. Spreading resistance across the diameter of crystal sections grown at 12 rpm with different axial field strengths.

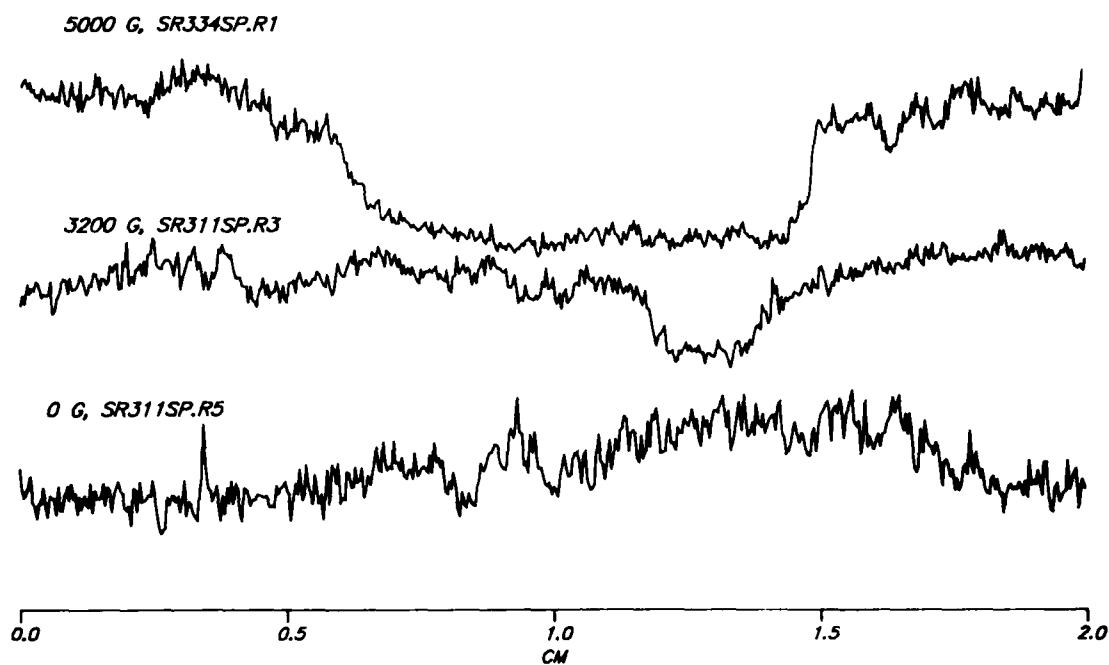
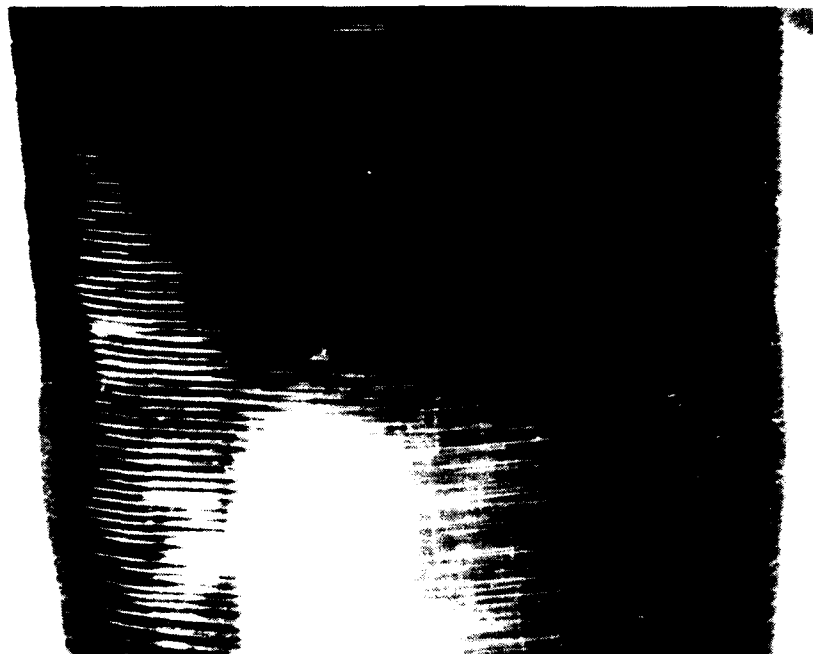


Figure 57. Radial spreading resistance scans for non-rotating crystals in an axial field. The formation of the well defined core is apparent at 5000 G.

The striation etch patterns for typical regions covered in Figures 56 and 57 are presented in Figures 58, 59, and 60. As with the transverse field, there is a flattening of the interface when the field is applied. The appearance of the core is not as obvious in the rotating sections as it is in the non-rotating section of Figure 60. In the actual sample from crystal Z334, the contrast between the core and the outer part of the crystal is further enhanced by a strong color difference. The most striking feature in the photograph, Figure 60(b), is the absence of fine striae in the core. We will discuss this further below. The orientation of the fine striae as they approach the core region indicates to us that the growth interface is relatively flat and therefore the temperature profile is also flat across most of the crystal diameter, even for the non-rotating section. Thus the increase in dopant concentration found in the core regions must be due to an increase in the diffusion boundary layer thickness. For the axial fields, the thickness change can be as large as a factor of 2 to 3. This is in sharp contrast to the transverse field case where changes did not exceed 40% for the data in Tables 3 and 5. Thus we find substantial thickening of the boundary layer in the center of the crystal but not at the edges when an axial field is applied. This suggests that the toroidal flow driven by the electrodynamic force is inhibited, certainly along the crystal axis. This reduced flow allows an increase in the diffusion boundary layer by a factor of 2 to 3.

For low Prandtl number fluids, the temperature profile is not strongly dependent upon fluid convection but is dominated by conductive heat flow. Nevertheless, convection does play a role in determining the interface shape. The flow of heated fluid down along the growth axis, driven by the electrodynamic forces acting on the surface layer in the necked down region of the melt, carries additional energy to the center of the growth

14312-36



(a) Magnet off

14312-38



(b) 3700 G axial field

Figure 58. Striation etch pattern for the
12 rpm sections of crystal Z331.

14312-40



(a) Crystal Z332, 0 to 4000 G transition

14312-42



(b) Crystal Z333, 0 to 5000 G transition

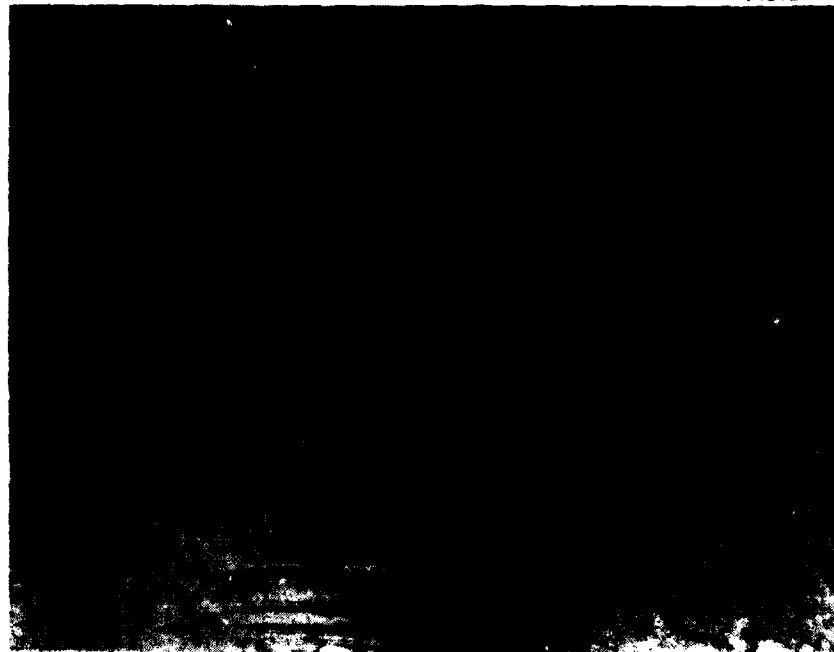
Figure 59. Striation etch pattern of the 12 rpm sections of crystals grown in an axial magnetic field.

14312-44



(a) Transition from 12 rpm and magnet off to 0 rpm and 5000 G axial field (4X).

14312-43



(b) Enlargement (25X) of boundary between core region on the right and the off-core region showing continuity of striations across the boundary.

Figure 60. Striation etch pattern of the non-rotating sections of crystal Z334.

surface. This added energy raises the temperature along the axis and is the reason for the curved interface. Rotation of the crystal induces an inertial force that enhances radial flow and thus often mitigates the effect of the flow along the axis. It is not unusual to see the interface flatten as the rotation rate is increased, as has been noted in earlier programs on dopant striations [1,2]. We believe that the restriction of flow by the magnetic field, in both transverse and axial configurations, produces the same effect as rotation in reducing the flow of hot melt along the growth axis. This effect is sufficient to cause the interface flattening invariably seen when a magnetic field is applied.

2. FLUCTUATION REDUCTIONS

In contrast to the transverse field, which altered the striae but did not substantially reduce them, the axial field has shown very encouraging signs of allowing the elimination of striae, at least over portions of the crystal. The appearance of the core region in Figure 60 suggests that striae have been greatly reduced, as compared to all other striation etch patterns that we have previously seen for gallium-doped silicon. Spreading resistance data confirm that the appearance is not misleading. In the core region of crystal Z334, grown without rotation, we have found the lowest fluctuation levels that we know about for Si:Ga material. In Figure 61, we have plotted several spreading resistance scans for various typical crystal growth conditions. Again a logarithmic ordinate is used to allow comparisons among different resistance levels. It is seen that the only specimen with a lower fluctuation than the core region of crystal Z334 is the neutron transmission doped (NTD) silicon wafer which is the most uniformly doped float zone silicon wafer that we have. For the NTD sample, at least two orders of magnitude more donors were added than were present in the high purity float zone starting crystal, thus almost

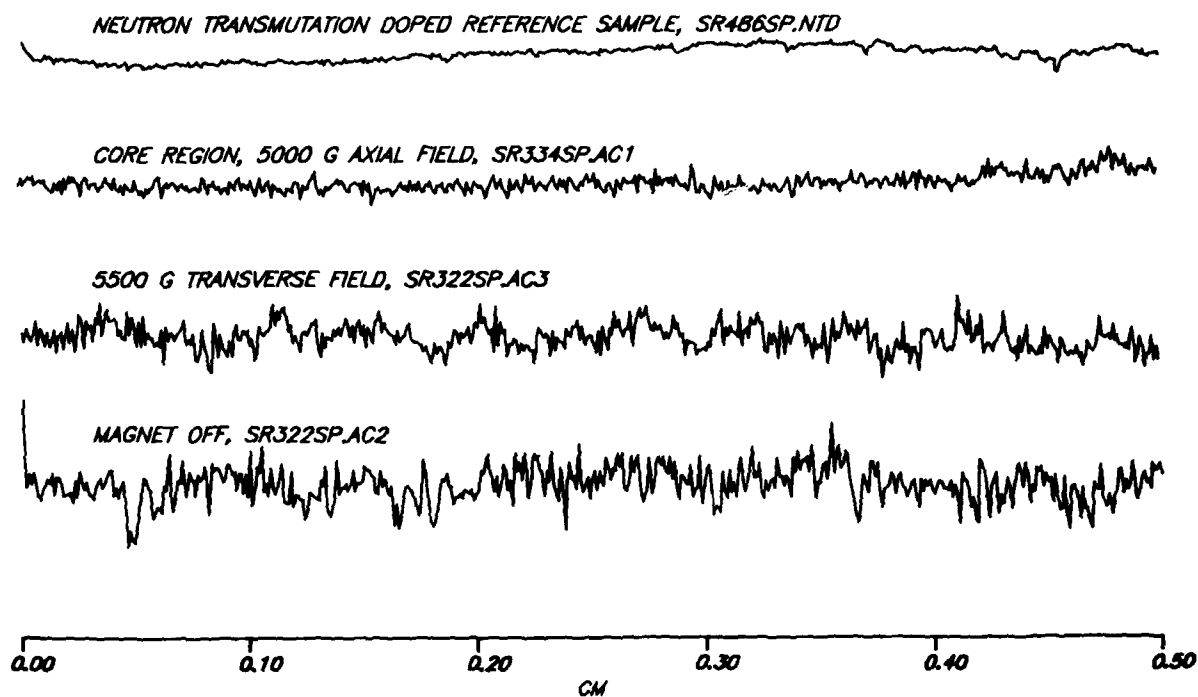


Figure 61. On-axis spreading resistance fluctuations for non-rotating crystal sections.

completely masking any original nonuniformity that may have existed. In Table 7, the relative standard deviations, calculated by the computer from the spreading resistance data, are compared for crystal sections grown under a variety of conditions. It is apparent that the core regions of crystals grown with a 5000 G axial field have lower fluctuations than the very best region seen in any of the transverse field crystals (SR322SP.AC3). Outside of the core, however, crystal Z334 is no better than average.

With the transverse field crystals, etch patterns like those in Figures 19 and 20 suggested to us that fluctuations might be reduced between the rotational striae. If one were to grow crystals at a low rotation rate and a high growth rate, then the rotational striae would be widely spaced and the intervening regions might be good for the fabrication of very uniform detector arrays. Figures 27 and 40 illustrate this type of region. As noted earlier this expectation did not materialize because the regions between the rotational striae were still subject to considerable small scale fluctuations. This was borne out in many different samples which often showed the strong saw-tooth shaped dopant distributions already seen in Figures 23 and 25. To determine what would happen in an axial field, we grew several sections at 3 rpm. Striation etch patterns for such regions grown at different field strengths are given in Figures 62, 63, and 64 and typical spreading resistance data are shown in Figure 65. The power spectral densities for these two scans are given in Figure 66, where the dopant fluctuation at the rotational frequency is seen to be enhanced by the field. It is apparent that at low rpm, considerable large scale dopant fluctuations still occur, even in the presence of a strong magnetic field. These may be related to the low frequency oscillations noted earlier in the non-rotating flows in the strong transverse fields. Thus we might conclude,

Table 7. Fluctuation Levels for Recent Crystals.

14312-52

FIELD STRENGTH G	FIELD ORIENTATION	CRYSTAL ROTATION RATE rpm	SCAN NUMBER	TYPE OF SCAN	SCAN LOCATION RELATIVE TO CORE	RELATIVE STANDARD DEVIATION %
0	—	12	SR333S.R2	RADIAL	—	6.92
3700	AXIAL	12	SR331S.R3	RADIAL	IN	8.08
3700	AXIAL	12	SR331S.R3	RADIAL	OUT	12.32
5000	AXIAL	12	SR333S.R1	RADIAL	IN	5.98
4000	AXIAL	12	SR332S.R1	RADIAL	IN	3.34
0	—	0	SR311S.R5	RADIAL	—	11.60
0	—	0	SR322S.AC2	AXIAL	—	11.24
3200	AXIAL	0	SR311S.R3	RADIAL	IN	9.79
5500	TRANSVERSE	0	SR322S.AC3	AXIAL	—	7.69
5000	AXIAL	0	SR334S.AE1	AXIAL	OUT	6.31
5000	AXIAL	0	SR334S.AC1	AXIAL	IN	3.54
NDT STANDARD			SR486S.NTD	RADIAL	—	1.59

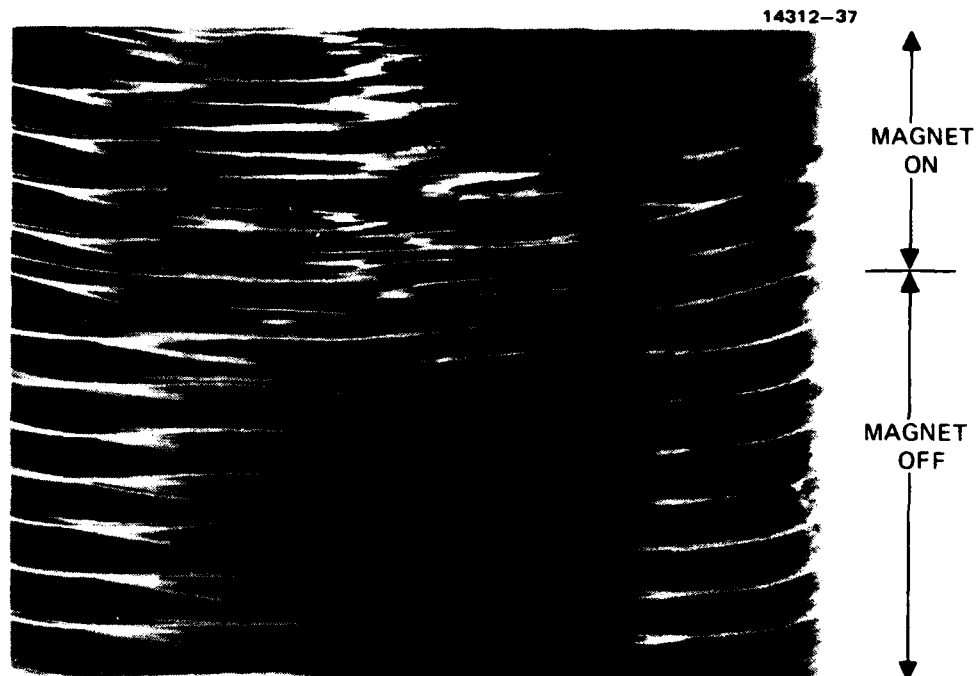


Figure 62. Striation etch pattern for the 3 rpm section of crystal Z331 showing the transition from magnet off to a 3700 G axial field.

14312-39

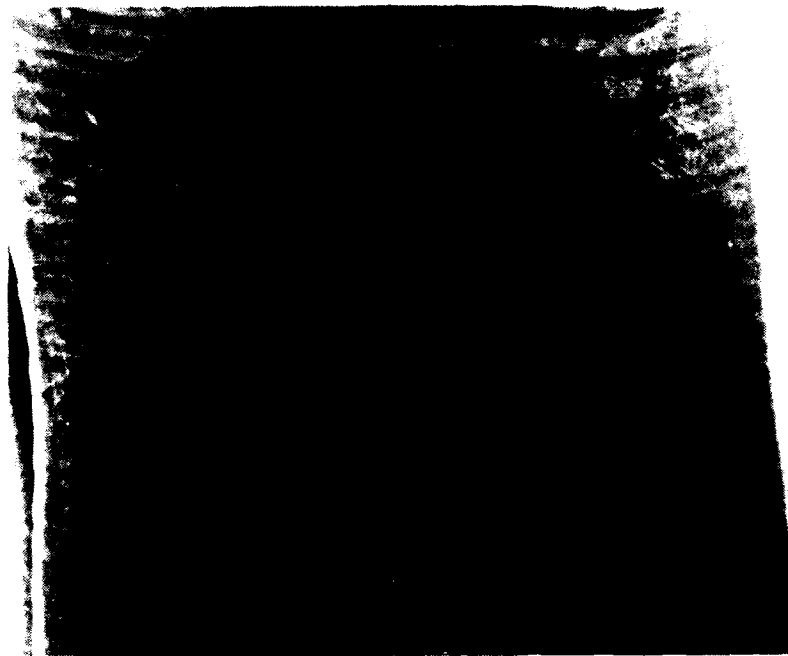


Figure 63. Striation etch pattern for the 3 rpm section of crystal Z332 grown in a 4000 G axial field.

14312-41



Figure 64. Striation etch pattern of the
3 rpm section of crystal Z333
grown in a 5000 G axial field.

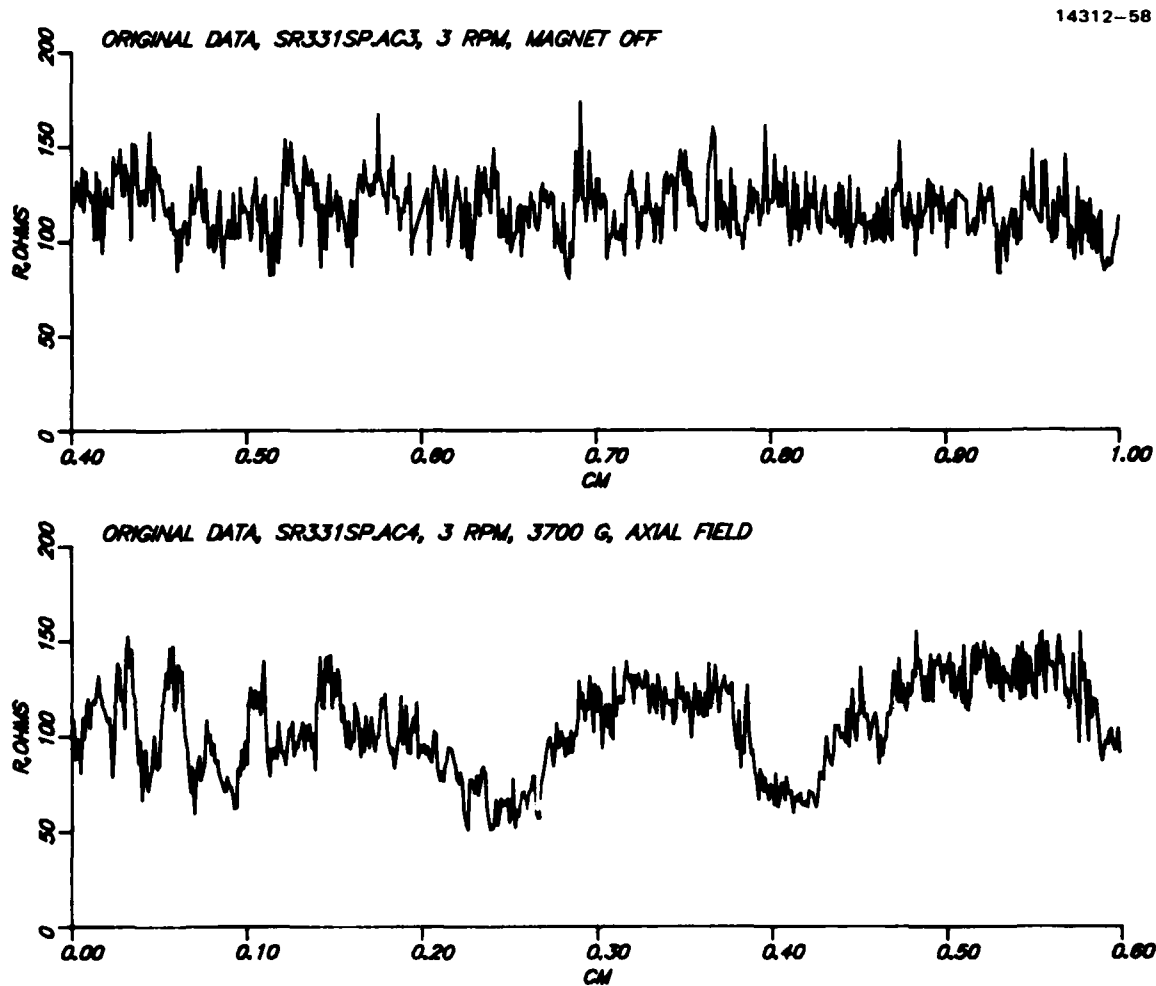


Figure 65. Spreading resistance for on-axis scans of the 3 rpm section of crystal Z331.

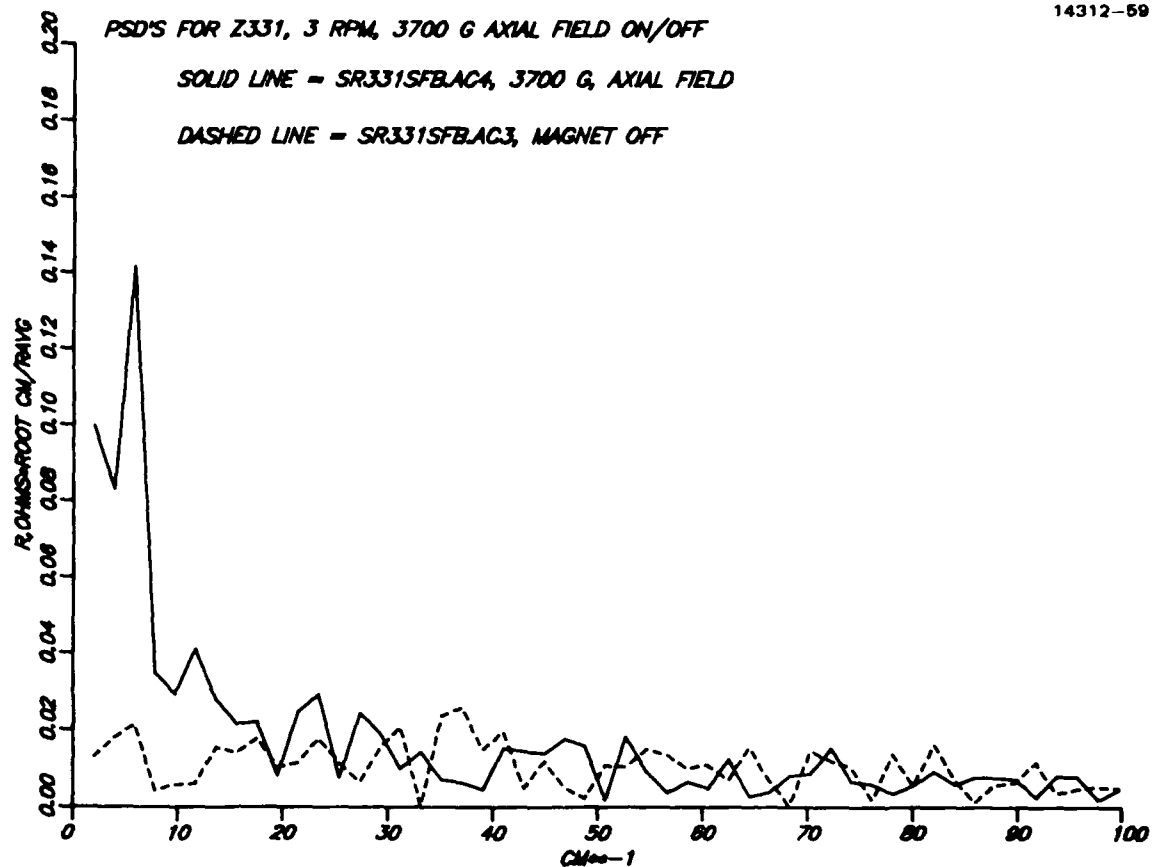


Figure 66. Power spectral densities for the on-axis scans of the 3 rpm section of crystal Z331.

on the basis of present data, that the answer to the reduction of fluctuations lies not in low rotation but in no rotation at all. However, we have obtained radial scans in regions of rotation that are remarkably uniform, at least over limited distances, presumably because the spreading resistance probe is tracing a path in between the rotational striae. An example of this is shown in Figure 67 for the 12 rpm section of crystal Z332. In Figure 68, the on-axis scan for this region shows a remarkable uniformity in between the rotational striae. Thus it is conceivable that wafers cut from a crystal grown in an axial field, even with rotation, might provide exceptional dopant uniformity in regions of limited extent. Data with the characteristics seen in Figure 68 have not been observed before in any of our previous work with doped float zone silicon

At the present, we hypothesize that the exceptional uniformity found in the centers of both rotating and non-rotating crystals is caused by a localized thickening of the boundary layer. In the axial field configuration, all radial flow is subject to the Lorentz force and therefore the toroidal circulation currents driven by the electrodynamic forces will not be as turbulent as when the magnetic field is absent. In the presence of the field, it is likely that the flow down along the centerline (the growth axis) of the crystal will be reduced, leading to the formation of a "stagnation" region in which the boundary layer will be considerably thickened and will not transmit fluctuations as easily to the growth interface as during normal growth. The encouraging results from the axial field experiments indicate the need for more careful study of the conditions leading to the "coring" phenomenon and the means for controlling it.

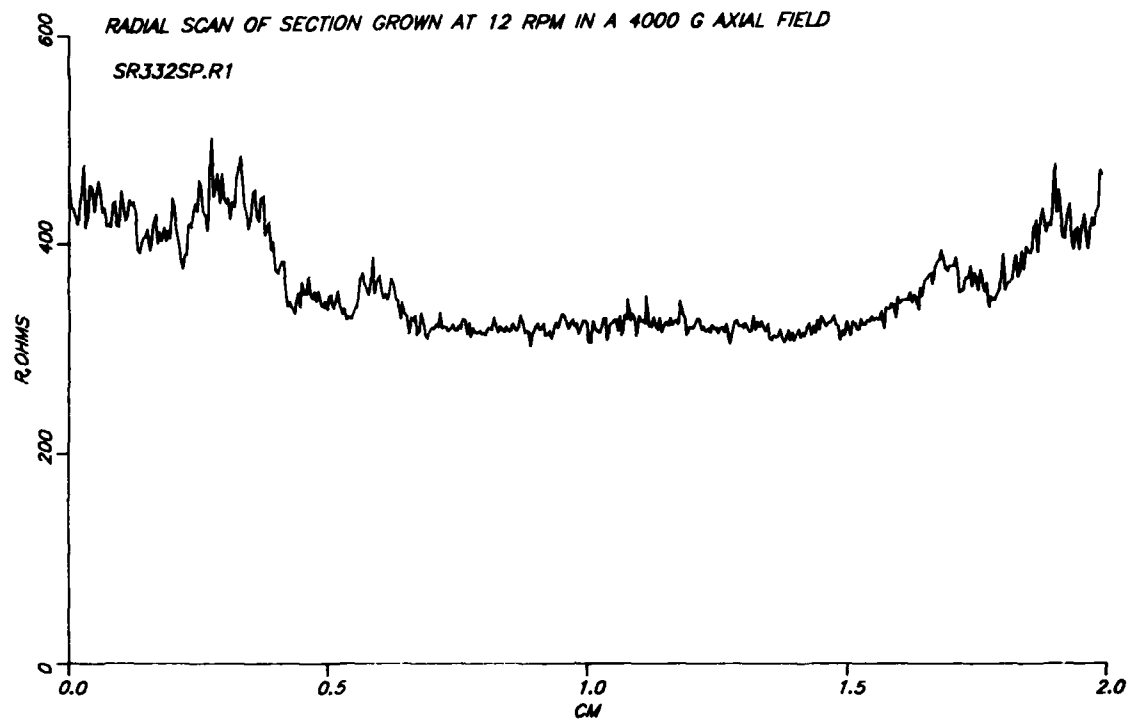


Figure 67. Spreading resistance across the diameter of a section grown at 12 rpm in a 4000 G axial field.

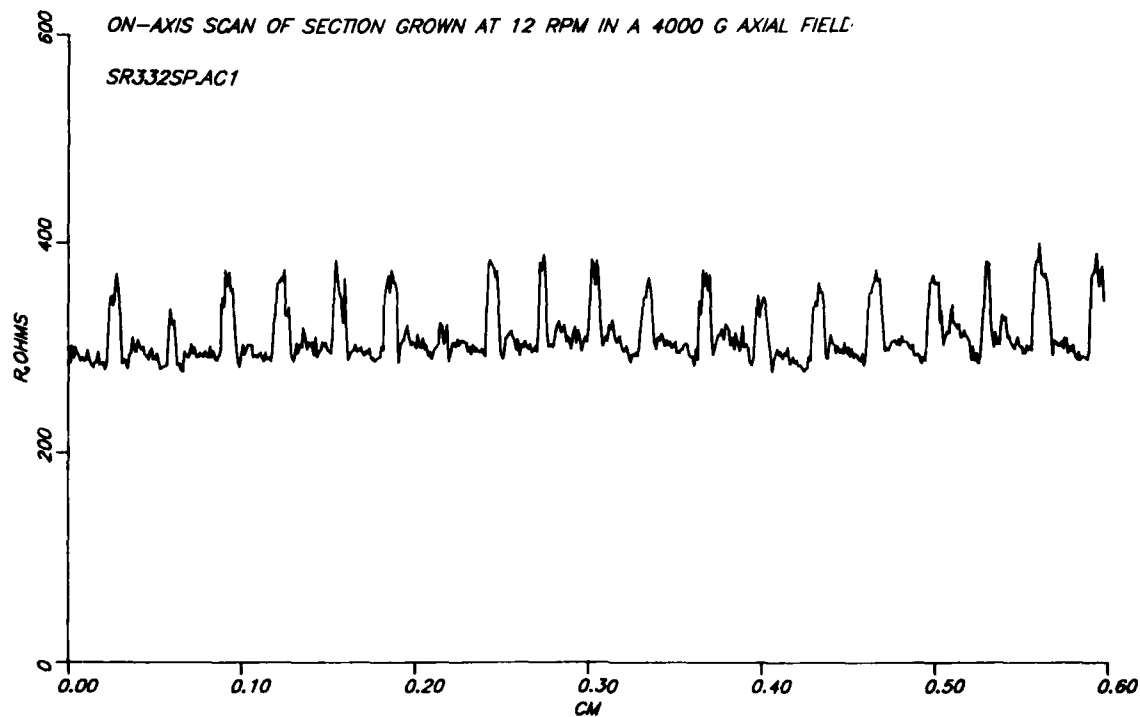


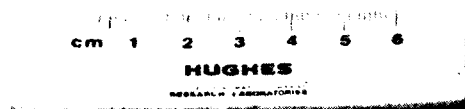
Figure 68. Spreading resistance for an on-axis scan of the 12 rpm region of crystal Z332 grown with a 4000 G axial field.

3. GROWTH BEHAVIOR

The results seen above, especially for the non-rotating crystal sections, indicate the direction for future work in reducing dopant fluctuations. Unfortunately, the growth conditions which now appear to promise substantial improvement in uniformity are the very ones that are the hardest to control. With an axial field we have had great difficulty in growing crystals at rotation rates of 3 rpm or less. As mentioned earlier, the application of a transverse field seems to have a stabilizing effect on a non-rotating crystal. Long sections of non-rotating crystal were grown at 5500 G with no difficulty. At present it seems that the axial field has a destabilizing effect on crystal growth. We have no explanation for this effect as yet and have not grown enough crystals to establish exactly what is occurring. Every attempt to grow a low or zero rpm section at field strengths above 3200 G has produced extreme wandering of the crystal about the growth axis. In Figure 69 are photographs of the external shape of three recent crystals in which portions of the crystals were grown at rotation rates of 3 rpm or less. In each case there was severe wandering of the crystal that necessitated drastic corrective measures by the crystal grower to avoid spilling of the melt. In growing crystal Z331, for which we have no photograph, the crystal began to wander when the rotation rate was reduced from 12 to 3 rpm in the presence of a 3700 G field. When the rotation rate was further reduced to zero, the interface began to tilt. This tilting happened so quickly and unexpectedly that the grower had no opportunity to apply corrective measures and the melt spilled. In the subsequent crystals shown in Figure 69, he was alert to the dangers of rotation rate reduction and was able to keep the crystals growing, though not in a configuration that was of much later use. However, crystal Z334 yielded a section about 25 mm long from which the valuable information on the

M16189

14312-45



(a) Crystal Z332, 4000 G

M16187

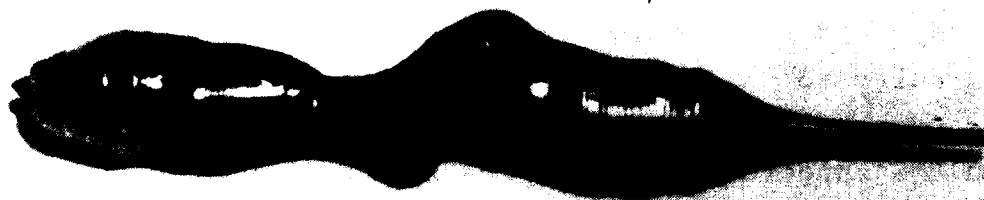
14312-46



(b) Crystal Z333, 5000 G

M16207

14312-47



(c) Crystal Z334, 5000 G

Figure 69. Crystals grown in a strong axial field showing severe wandering about the growth axis.

uniform core region was obtained. The three crystal subsequently produced for delivery were grown in a 5000 G field at 12 rpm. Even under this condition there was a tendency for the crystal to wander about the growth axis.

At this time we do not have sufficient data to generalize about the observed instability in the axial field growth. It is apparent that if one wishes to capitalize on the low fluctuation levels in the core regions of non-rotating crystals, then techniques must be established to prevent the crystal wandering or interface tilting that has been observed. It may even be that some combination of transverse and axial fields, such as that produced by the tilted solenoid magnet, would be suitable. Further work in this direction seems warranted.

SECTION V

CONCLUSIONS

At the beginning of this program, the only experience available on the effects of a magnetic field on float zoning was our own work with the transverse permanent magnet [2] and the axial field work of de Leon, et al.[8], both done with relatively weak fields. After considerable work in this program with electromagnets at field strengths up to 2000 G, it became apparent that reductions in the striations of float zone silicon, if they could be achieved at all, would require field strengths in excess of 2000 G. Working at this higher field strength level has required the development of new growth techniques and equipment to allow float zone growth in the presence of both transverse and axial fields at levels up to 5000 G. We have been successful in this development effort and the experimental results have produced two major findings.

From the standpoint of dopant uniformity, the more important of these is the demonstration of nearly striation free regions of crystal grown in a 5000 g axial field. While our understanding of the conditions governing such striation free regions is far from complete, it is apparent that an approach of high promise is now available. The desirable region occurs in the center of the crystal as a core of increased dopant concentration having fluctuation levels approaching those of neutron transmutation doped samples, the best standard of striation free silicon that is known. Means for controlling the major dopant concentration in the core and for extending the size of the core while still maintaining its good characteristics remain to be worked out in further experimental programs.

The other significant finding is that the transverse field provides a unique tool for investigating the physics of the float zone process. In this regard it may prove valuable in

defining the hydrodynamic conditions that we believe are responsible for the uniform core produced in strong axial fields. With the strong transverse field we have seen effects on crystal morphology that have not been reported previously. These should be of great interest to hydrodynamicists studying crystal growth. The coupling of the experimental techniques provided by this program with a theoretical study of the mass and energy transport phenomena occurring during crystal growth in a magnetic field ought to produce a deeper understanding of the float zone process. With this understanding will come detector grade silicon of greatly improved dopant uniformity. Such material will be of prime importance to the very low background detector technology now emerging from other government and industry sponsored programs.

SECTION VI

RECOMMENDATIONS FOR FUTURE WORK

It is now apparent that growth of float zone crystals in the presence of strong magnetic fields leads to very interesting results. Prospects for obtaining more uniformly doped detector-grade silicon by the use of a strong axial magnetic field are very good and we will outline below some of the steps believed necessary to capitalize on this potential. The use of strong transverse fields, while presently not attractive, per se, for reducing striations, appears to offer unique experimental opportunities for studying the physics of the float zone process. The understanding which would result from experiments designed to elucidate the energy and mass transport occurring in the melt zone should also improve the control over the growth in an axial field. Thus we see a two-pronged effort for the future in which the existing growth apparatus, with its strong field capabilities, is used to attack both practical and theoretical aspects of float zone growth. The objective in any future work, as was the case in the program just concluded, would be to reduce as much as possible the unwanted dopant fluctuations in detector-grade silicon. Excellent progress has been made during the past year in developing a new growth method essential to the pursuit of this objective. However, there remain the tasks of extending the techniques to larger crystal diameters, developing reliable methods for controlling the dopant at preset levels, expanding the low fluctuation region to include a larger fraction of the crystal volume, and developing a stable growth method for non-rotating crystals in a strong axial magnetic field.

To carry out these tasks, we currently envision a program structured to include the following elements:

Increased Crystal Diameter: More rf power is needed to grow larger crystals. The present furnace power supply, with an input rating of 35kW has limited growth to diameters no larger than 30 mm. This unit should be replaced by one with an input power of at least 75 kW to permit growth of 52 mm diameter crystals. The present furnace arrangement with the quartz tube growth section is capable of handling the additional rf power.

Stabilization of Non-rotating Crystal Growth: New experimental approaches must be developed. Possibilities are inhomogeneous magnetic fields, perhaps even a return to the tilted solenoid configuration or some other combination of axial and transverse orientations. With guidance from the theoretical modelling studies, other options such as coil design modifications and the use of cooling rings or heat shields should be considered.

Control of Homogeneous Core Region: More growth experience is needed to establish the parameters controlling both the size and dopant concentration of the core. We anticipate that as the crystal diameter is increased, the axial magnetic field needed to maintain a stagnation region of useful size will also increase. Therefore additions to the magnet system will be required. These will probably take the form of larger coils with 120 to 150 turns each instead of the 88 turns now being used. The increased turns will require a doubling of the dc voltage presently used. This can be most easily accomplished by acquiring a second power supply, identical to the present one, and using one supply for each coil, in place of the series arrangement now used. By this technique we should be able, at minimum expense, to create axial fields in excess of 8000 G.

Study of Float Zone Growth Physics: As an essential ingredient in the above tasks, we need a better understanding of the physical processes occurring during crystal growth. Valuable inputs can come from modelling studies of the float zone process, especially if they include results from experiments designed to take advantage of the unique opportunities afforded by the magnetic field to perturb the flows within the melt volume. Some exploratory work with IR&D funds has already shown the feasibility of measuring temperature fluctuations in the melt. These can be coupled with the

spreading resistance analysis techniques employed in the present work to characterize the turbulent fluctuations that cause the fine striations. A joint effort with a university research group interested in float zone theory is seen as a practical way in which to maximize the returns from the unique experimental facility that has evolved during the present program.

Experience on the present program strongly suggests that any future programs ought to be planned with a time schedule that is compatible with the nature of the experimental work. The growth and analysis of even one crystal can easily extend over a several month period. If the results are subsequently reviewed and analyzed by a theoretical group, then the next growth iteration is even further delayed. It seems to us that the most effective way to proceed under these circumstances is to plan a program that extends over a long period at a relatively low average support level but which in fact will be pursued in separated periods of concentrated activity consisting, sequentially, of a small set of crystal growth runs, sample preparation, sample measurements, analysis, application of theory to define the next set of growth runs, and modification of theory to fit the latest results. Since these activities involve several different groups of investigators, no one area will be continuously engaged on the program, with the possible exception of the modelling activity after the program has produced the first results. We believe that such a program, extending over a three year period, would be most effective in developing the methods to produce truly "striation free" silicon.

REFERENCES

1. H. Kimura et al., Advanced Silicon Material Development for LADIR, Final Report, AFWAL-TR-81-4021, Dec. 1981
2. H. Kimura et al., J. Cryst. Growth 62 (1983) 523
3. G. D. Robertson, H. Kimura, and G. C. Valley, Striation Free Doped Silicon, USAF Contract No. F33615-81-c-5065, Interim Report No. 1, August 1982
4. Ibid, Interim Report No. 2, July 1984
5. H. P. Utech and M. C. Flemings, J. Appl. Phys. 37 (1966) 2021
6. H. A. Chedzey and D. T. J. Hurley, Nature 210 (1966) 933
7. S. Sen et al., J. Cryst. Growth 43 (1978) 526
8. N. de Leon, J. Guldborg, and J. Salling, J. Cryst. Growth 55 (1981) 406
9. K. Hoshi et al., Extended Abstracts, 157th Electrochemistry Society Meeting 80-1 (1980) 811
10. K. Hoshikawa, Jap. J. Appl. Phys. 21 (1982) L545
11. J. Osaka et al., Jap. J. Appl. Phys. 23 (1984) L195
12. A. Muhlbauer, W. Erdmann, and W. Keller, J. Cryst. Growth 64 (1983) 529
13. G. M. Harriot, PhD Thesis, Chemical Engineering Dept., MIT, 1983
14. R. A. Brown, MIT, private communication
15. D. Schwabe et al., J. Cryst. Growth 43 (1978) 305
16. D. Schwabe and A. Scharmann, J. Cryst. Growth 46 (1979) 125
17. C.-H. Chun and W. Wuest, Acta Astronautica 6 (1979) 1073

18. ----, Proc. 3rd European Symp. on Material Sci. in Space, Grenoble, 24-27 April 1979, Paper V.3, p 283
19. ----, Adv. Space Res. 1 (1981) 17
20. ----, Acta Astronautica 9 (1982) 225
21. C.-H. Chun, J. Cryst. Growth 48 (1980) 600
22. A. F. Witt, M. Lichtensteiger, and H. C. Gatos, J. Electrochem. Soc. 121 (1974) 787

APPENDIX A

MAGNETIC FIELD INTERACTIONS

In support of the crystal growth experiments we have initiated a small study of the effects of a magnetic field applied externally to float-zone silicon. Since liquid silicon is a highly conductive fluid, and since we are interested in fluctuations that vary slowly compared to electromagnetic waves, ordinary magnetohydrodynamics is applicable. Application of an external magnetic field in a conducting fluid causes two well-known effects: an increased stiffness perpendicular to the field lines and an increased energy dissipation due to Joule heating. Application of a magnetic field also allows other modes of oscillation. Evaluation of the impact of an applied field on the thermal instabilities present in float-zone silicon requires knowledge of the relative strengths of effects in silicon.

A. DIMENSIONAL ANALYSIS OF FLOW

The relative size of separate physical effects in fluids is most easily evaluated by using dimensional analysis and calculating various dimensionless numbers. This has been done for float-zone silicon. Table A-1 summarizes the properties of float-zone silicon that are needed to calculate the dimensionless numbers. Table A-2 lists values of typical parameters, and Table A-3 summarizes the dimensionless numbers.

Each line in Table A-3 yields certain key information. The Bond number of 0.14 in line 1 indicates that surface tension dominates buoyancy. The Hartmann number of 39 in line 3 is large enough, according to Chandrasekhar's [A-6] calculations, to significantly increase the critical Rayleigh number for instability. One would infer that the critical Marangoni number for surface tension driven flow would also increase with an applied external field, but no analysis of this has been found yet. The fact that the Marangoni number calculated for a temperature gradient of $50^{\circ}\text{K}/\text{cm}$ in line 4 exceeds the critical Marangoni number indicates that surface tension instabilities occur. Likewise, from line 6 the fluid may be subject to

Table A-1. Summary of Si Properties

		Reference
density	$\rho = 2.5 \text{ g/cm}^3$	A-1, A-2
viscosity	$\mu = 8.8 \cdot 10^{-3} \text{ poise } (\text{g/cm}^3) \text{ cm}^2/\text{s}$	A-1
kinematic visc.	$\nu = 3.5 \cdot 10^{-3} \text{ stokes } - \text{ cm}^2/\text{s}$	A1, A-2
coeff of heat cond.	$k = 0.077 \text{ cal}/(\text{cm}^\circ\text{K}) = 3.2 \cdot 10^6 \text{ erg}/(\text{cm}^\circ\text{K})$	A-1
thermometric cond.	$\kappa = 0.15 \text{ cm}^2/\text{s}$ (used $\text{Pr} = \frac{C_v \mu}{\kappa} = .023$)	A-1
melting point	$T_m = 1410^\circ\text{C}$	A-2
el. conductivity	$\sigma = 1.29 \cdot 10^4 \text{ ohm}^{-1} \text{ cm}^{-1} (1450^\circ\text{C})$ $= 1.16 \cdot 10^{16} \text{ s}^{-1}$	A-2, A-3
diffusion coeff.	$D = 7 \cdot 10^{-4} \text{ cm}^2/\text{s}$	
thermal exp coeff.	$\alpha = 2.5 \cdot 10^{-5} \text{ }^\circ\text{K}^{-1}$	A-4
melt/vapor surf tension	$\gamma = 720 \text{ dyne/cm}$	A-1, A-5
surf. tens gradient	$\partial\gamma/\partial T = 0.43 \text{ dyne/cm}^\circ\text{K}$	A-1
magnetic diffusivity	$\eta = 6.2 \cdot 10^3 \text{ cm}^2/\text{s}$	A-6

Table A-2. Typical Values for Float-Zone Silicon

L	$= 1 \text{ cm}$	horizontal length scale
h	$= 1 \text{ cm}$	vertical length scale
$\partial T/\partial h$	$= 50^\circ\text{K/cm}$	vertical temperature gradient
ΔT	$= 5^\circ\text{K/cm}$	horizontal temperature difference from surface to center
H	$= 1000 \text{ gauss}$	
Ω	$= 12 \text{ rpm} = 1.3 \text{ rad/s}$	

Table A-3. Summary of Dimensionless Numbers

<u>Name</u>	<u>Formula</u>	<u>Size</u>	<u>Critical Value</u>	<u>Physical Meaning</u>	<u>Reference</u>
Bond	$Bo = \frac{\rho g L^2}{ \gamma }$	0.14		gravitational potential energy surface tension energy	A-4
Hartmann	$H = \frac{B_0 L}{c} \sqrt{\frac{\sigma}{\mu}}$	39		magnetic "viscosity" normal viscosity	A-6, A-3
Magnetic Reynolds	$Rm = \frac{4\pi\sigma L^2 \Omega}{c^2}$	$2.2 \cdot 10^{-4}$		diffusion of field lines field lines frozen in fluid	A-3
Marangoni	$Ma = \frac{ \partial\gamma/\partial T h (\partial T / \partial h)}{\mu \kappa}$	$1.6 \cdot 10^4$		surface tension driven convection viscous dissipation	A-7, A-8
Prandtl	$Pr = \frac{\nu}{\kappa}$.023		momentum diffusion thermal diffusion	A-7
Rayleigh	$Ra = \frac{g \alpha \partial T / \partial h h^4}{\kappa \nu}$	2300	1700	vertical stability of a layer of fluid	A-6
Reynolds	$Re = \frac{Pr^2 \Omega}{\mu}$	360	2000	inertial viscous forces	A-6, A-9
Taylor	$T = \left(\frac{2 \Omega L^2}{\nu} \right)^2$	9100		rotational version of Re	A-6
Centrifugal Field Grashof	$Gr_z = \frac{\rho \Omega^2 \alpha \Delta T r^3}{\nu^2}$	27		horizontal stability of fluid with temperature gradient in centrifugal field	A-4

Rayleigh instability for temperature gradients greater than about $40^{\circ}\text{K}/\text{cm}$. The small Reynolds number in line 7 indicates that no ordinary turbulence will be present. The Taylor number (line 8) is also well within the range found by Chandrasekhar to increase critical Rayleigh numbers. The effect of rotation on Marangoni flow has been studied recently by Chun [A-4], indicating that for our conditions the effects of rotation on Marangoni flow is not significant to the extent of inducing appreciable changes in the flow pattern. Forced convection due to crystal rotation, however, does interact with Marangoni flow near the growth interfacial boundary layer to cause disruptions in the striae (feathering).

The preceding dimensional analysis suggests that Marangoni convection is the dominant instability mechanism and that the next key task is to determine the effect of an applied magnetic field on Marangoni convection.

Another plausible flow mechanism which is neglected is the flow induced by the electrodynamic force from the rf field. Since the magnitude of the electrodynamic force is not known quantitatively, it is not possible at present to assess whether the Marangoni or the rf stirring flow is the dominant flow. Our results, however, are consistent with those of Chun [A-4] for the Marangoni flow. The striae pattern, as well as the frequency of the fine striae, and be explained by the model proposed and observed by Chun [A-10].

B. INFLUENCE OF MAGNETIC FIELD ON FLOW PATTERNS

The detailed motion of small-scale fluctuations in float-zone silicon has not been calculated to our knowledge, so it does not appear possible to make a direct calculation of many magnetic field effects. It does appear feasible, however, to calculate the magnetic-field effects on a variety of simple flow patterns in order to improve our understanding of what geometrics and strengths cause what effects. Below are several illustrative calculations, modified for float-zone silicon, and the application of calculations to understand the effects of the magnetic field. In the discussions which follow, detailed mathematical derivations are omitted, since these are available in the references.

1. Hartmann Flows

a. Channel Flow

Consider flow between two infinite plane plates driven by a pressure gradient dp/dx parallel to the plates. In the absence of a magnetic field, the velocity, V_x , parallel to the plates is given by

$$V_x = \frac{1}{2} \frac{dp}{dx} \frac{L^2}{\nu} \left(1 - \frac{z^2}{L^2} \right), \quad (A-1)$$

where $2L$ is the separation of the plates, z is the distance from the center plane between the plates, and ν is the kinematic viscosity. In the presence of a magnetic field, B_0 , across the channel the velocity becomes^{A-11}

$$V_x = \frac{1}{2} \frac{dp}{dx} \frac{L^2}{\nu} 2 \left[\frac{\cosh Q^{1/2} - \cosh (Q^{1/2} z/L)}{Q^{1/2} \sinh Q^{1/2}} \right], \quad (A-2)$$

where $Q^{1/2}$ is the Hartmann number, defined by

$$Q^{1/2} = \left[\frac{\sigma B_0^2 L}{\mu c^2} \right]^{1/2}, \quad (A-3)$$

where σ is the conductivity, μ is the viscosity and c is the speed of light. The effect of the magnetic field is to slow the flow down. Figure A-1 shows a plot of the peak velocity from Equation A-2 as a function of $Q^{1/2}$, and as a function of B_0 in liquid silicon with $L=1$ cm. Note that a field of 500 gauss is sufficient to decrease the peak velocity by a factor of 10.

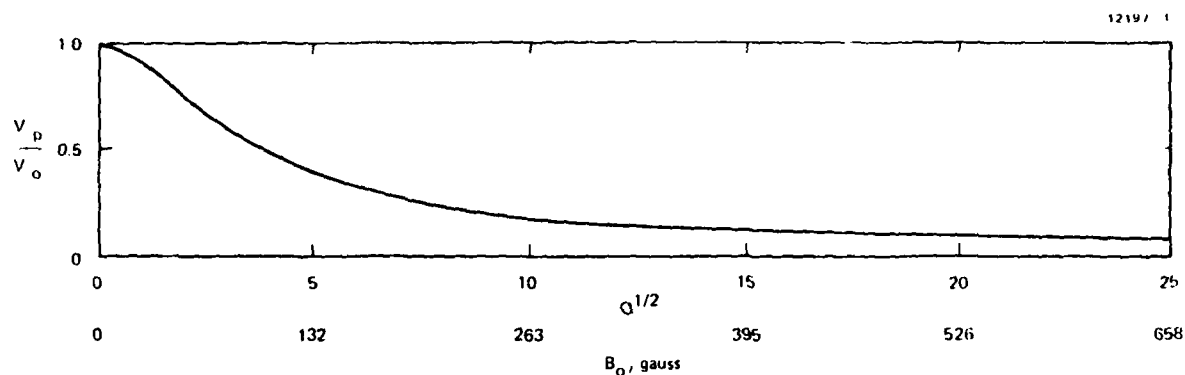


Figure A-1. Channel flow with a transverse magnetic field. Peak velocity, V_p , divided by $V_0 \equiv 1 dp/2 dx L^2/\nu$ (V_0 = peak velocity with no field), is plotted as a function of Hartmann number, and as a function of magnetic field in liquid silicon.

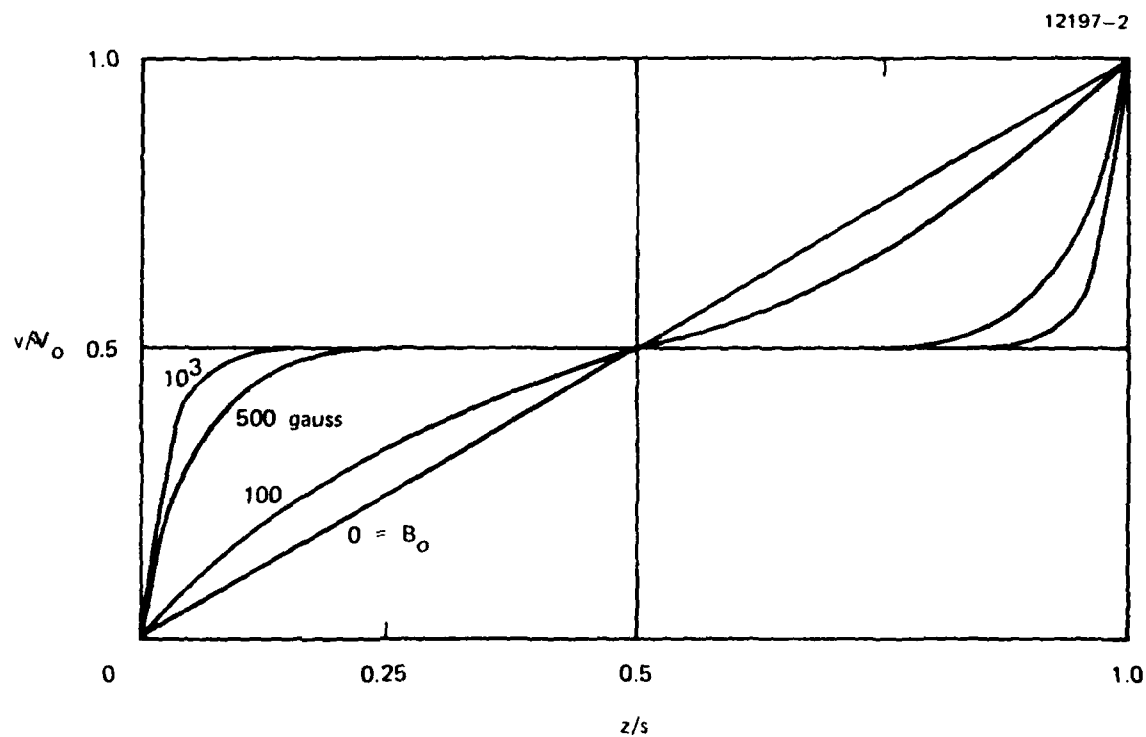


Figure A-2. Shear flow with a transverse magnetic field. Velocity, v , in the flow divided by velocity of wall V_0 , is plotted as a function of distance across the channel z/s .

b. Shear Flow

Consider fluid between two infinite plates, one of which moves at a velocity, V_0 . Without a magnetic field, the flow pattern is a linear shear,

$$v = V_0 z/s , \quad (A-4)$$

where s is the separation of the plates. With a magnetic field perpendicular to the flow, the velocity becomes^{A-3}

$$v/V_0 = \frac{1}{2} + \frac{\sinh(Q^{1/2}z/s) - \sinh Q^{1/2}(1-z/s)}{2 \sinh Q^{1/2}} . \quad (A-5)$$

Figure A-2 shows the flow velocity as a function of z/s for $B_0 = 0, 100, 500$, and 1000 gauss. Note that unlike the Channel flow the magnetic field cannot stop the motion in this case. In order to decrease the total flow across the field, however, the shear is localized into thin layers near the walls; thus, the shear near the walls is actually increased due to the magnetic field.

2. Convective Instability

a. Horizontal Magnetic Field, No Viscous Effects

Consider a conducting fluid of infinite horizontal extent, heated from below. This situation, as seen in a boiling pot of water, is absolutely unstable. If a horizontal magnetic field is applied to the fluid, the effect is analogous to a horizontal tension added to the fluid. Whether or not the magnetic field stabilizes fluctuations in such a fluid depends on the horizontal scale of the fluctuations. In the absence of dissipative effects, balancing the restoring force of the magnetic tension against the buoyant force of a heated fluid element yields^{A-2}

$$\rho \alpha \beta g \geq \frac{B_0^2}{\lambda^2}, \quad (A-6)$$

where ρ is the density, α is the thermal expansion coefficient, $\beta = dT/dZ$ is the vertical temperature gradient, g is the acceleration due to gravity, B_0 is the magnetic field strength, and λ is the length scale of the instability. For the parameters listed in Tables A1 and A2, Equation (A-6) implies that fluctuations are stable up to about 900 cm in length. This result would seem to indicate a tremendous stabilizing effect of a horizontal magnetic field on vertical convection. Unfortunately, inclusion of dissipative effects modifies this estimate substantially, as shown in the next section.

b. Horizontal Magnetic Field With Dissipative Effects

A dissipative fluid allows distorted magnetic field lines to slip back through the fluid so that the stabilizing effect of the field is not nearly as great as in a non-dissipative fluid. This is reflected in the smallest length scale of unstable motion, which becomes^{A-12}

$$\lambda^2 \sim \frac{\pi \kappa B_0^2}{\eta \rho \beta \alpha g}, \quad (A-7)$$

where κ is the thermal diffusivity and η is the magnetic diffusivity. Equation (A-7) yields (for parameters from Tables A1 and A2)

$$\lambda \text{ (cm)} \sim 8 \cdot 10^{-3} B_0 \text{ (gauss)} ;$$

i.e., fluctuations less than 8 cm are stable or are damped out in a 1000-gauss field.

c. Vertical Field

The case of Rayleigh instability in the presence of a vertical and a diagonal magnetic field has been extensively analyzed by Chandrasekhar.^{A-6} Figure A-3, which is illustrative of his results, shows that the critical Rayleigh number jumps by about a factor of 10 for a Hartmann number squared (Q) and equal to 1500 ($B_0 = 1000$ gauss in silicon). The estimated Rayleigh number in Table A-3, based on a vertical temperature gradient of 50°K/cm , is 2300. Application of a vertical magnetic field of 1000 gauss to the float-zone silicon means that temperature gradients as high as 200°K/cm would not produce Rayleigh instability. Gradients significantly higher than 50°K/cm appear unlikely however, so the increase in critical Rayleigh number with application of a vertical magnetic field is probably of limited relevance to reducing buoyant fluctuations in the float-zone silicon.

3. Effect of Magnetic Field on Surface Tension Driven Instability

Consider a horizontal interface between two liquids (e.g, silicon and the surrounding atmosphere). Following Pearson,^{A-13} the equation for the surface tension change due to temperature variations across the interface is given by

$$\rho v \frac{\partial^2 v}{\partial z^2} = \left(- \frac{\partial \gamma}{\partial T} \nabla_{\perp}^2 T \right), \quad (\text{A-8})$$

where x and y are in the plane at the surface and z is perpendicular, v is the velocity perpendicular to the surface, $(-\partial\gamma/\partial T)$ is the temperature coefficient of the surface tension, and $\nabla_{\perp}^2 = \partial^2/\partial x^2 + \partial^2/\partial y^2$. The equation for the temperature is^{A-13}

$$-\kappa \nabla^2 T = \beta V, \quad (\text{A-9})$$

where $\beta = \partial T/\partial z$. If a constant magnetic field, B_0 , is added parallel to the interface in the y direction, Equation (A-8) becomes

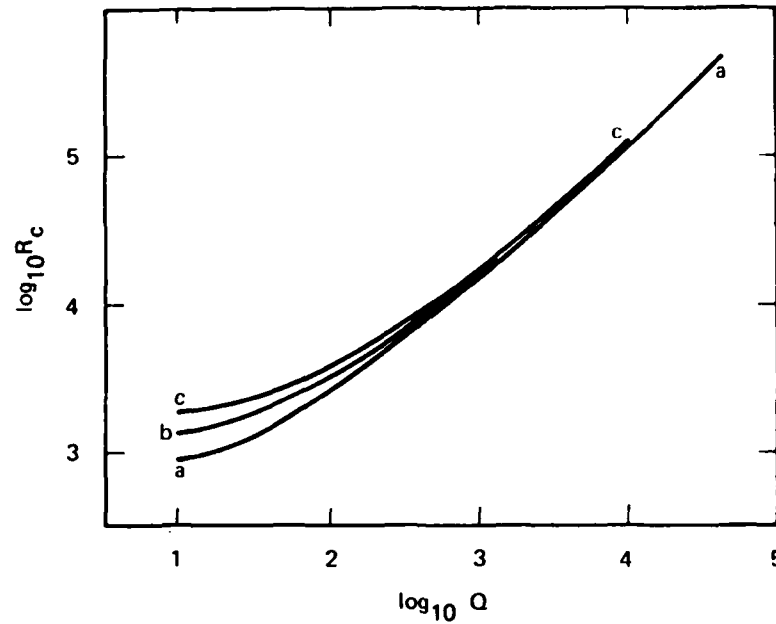


Figure A-3. The variation of the critical Rayleigh number, R_c , for the onset of instability as a function of Q for the three cases: (i) both bounding surface free (curve labeled aa); (ii) one bounding surface free and the other rigid (curve labeled b); and (iii) both bounding surfaces rigid (curve labeled cc).

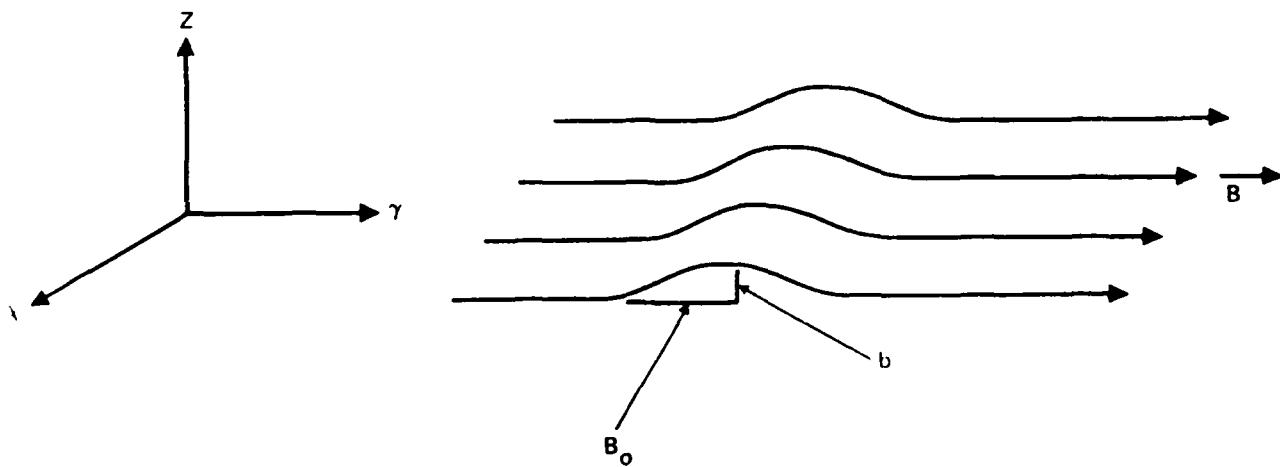


Figure A-4. Geometry of surface distortion with magnetic field.

$$\rho v \frac{\partial^2 v}{\partial z^2} + \frac{1}{4\pi} B_0 \cdot \nabla b = \left(- \frac{\partial \gamma}{\partial} v_{\perp}^2 T \right), \quad (A-10)$$

where b is the perturbation in the field due to a distortion of the surface, as shown in Figure A-4. The magnetic field perturbation can be related to the velocity, v , through Maxwell's equation,^{A-3}

$$B_0 \cdot \nabla v + \eta \nabla^2 b = 0. \quad (A-11)$$

Combining Equations (A-9), (A-10) and (A-11) yields a relation for the magnetic field strength required for the magnetic tension to balance the decrease in surface tension. Thus

$$B_0^2 = \frac{4\pi(\partial\gamma/\partial T)\beta\eta}{\kappa}, \quad (A-12)$$

and

$$B_0 = 3300 \text{ gauss}$$

for parameters in Table A-1 and $\beta = 50^\circ\text{K/cm}$. It should be noted that this magnetic field will stabilize only those fluctuations whose wavevector has a component along B_0 . There is no effect on fluctuations with wavevectors perpendicular to B_0 because $B_0 \cdot \nabla \rightarrow 0$ in this case.

4. Other Instabilities

Chandrasekhar^{A-6} discusses a number of other instabilities in the presence of a magnetic field. These include the Rayleigh-Taylor and Kelvin-Helmholtz instabilities for two layers of fluid of different densities, instability of Couette flow inside two concentric cylinders rotating at different rates, and capillary instability of a liquid jet. These results, while interesting, appear to be of limited usefulness in this study because float-zone silicon does not appear to undergo any of these instabilities.

That is, the critical number for these instabilities evaluated for float-zone silicon lies below the unstable transition, or the basic conditions necessary for instability are not present in float-zone silicon. These calculations do, however, illustrate that the magnetic field can act like surface tension in reducing instability. For instance, in the Rayleigh-Taylor instability a horizontal magnetic field acts like a surface tension, T_{eff} , of the form,^{A-6}

$$T_{\text{eff}} = \frac{B^2}{2\pi k} \cos^2 \theta, \quad (\text{A-13})$$

where k is the wavevector of the instability and θ is the angle between k and B . If $k = 2\pi/1\text{cm}$, and $\theta = 0$, then a field of 1000 gauss is equivalent to a surface tension of $2.5 \cdot 10^4$ dyne/cm, compared to 720 dyne/cm in Si. It should be noted, of course, that for disturbances that have wavevectors perpendicular to B , $T_{\text{eff}} = 0$, and the field has no effect.

The calculations on capillary instability are equally instructive in that they show the effect of dissipation on field strengths required for stability. Without dissipation, Chandrasekhar finds that field strengths of

$$B > \left(\frac{2\pi\gamma}{R} \right)^{1/2} \quad (\text{A-14})$$

"will stabilize the jet for varicose deformations of all wavelengths" (p. 545). (γ is the surface tension and R is the radius of the fluid.) For $\gamma = 720$ dyne/cm and $R = 1$ cm this yields $B = 67$ gauss. Inclusion of dissipation yields

$$B^2 > 80\pi\eta \left(\frac{\rho\gamma}{R^3} \right)^{1/2}, \quad (\text{A-15})$$

or $B > 8000$ -gauss. Incidentally, if we use Equation (A-14) with $(\partial\gamma/\partial T)\Delta T$ replacing γ , we obtain $B > 3400$ gauss for $\Delta T = 50^\circ\text{K}$. This last result should be interpreted only as dimensional analysis.

5. Discussion

Several interim conclusions can be extracted from the preceding sections. First, in terms of Hartmann flow, the difference between fields of 100 and 500 gauss is great, while the added effect of going from 500 to 1000 gauss is not great. Second, a field of 1000 gauss should have the effect of stopping most of the flow across the field, but we should expect larger shears at the liquid-solid interface and we should expect to lose some of the stabilizing effects of rotation. Third, a vertical field may be more useful for suppressing Marangoni convection since in this case the field lines have a component in the surface of the silicon on all sides of the float zone. Fourth, there is some indication that fields over 2000 gauss may be required to compete with surface tension.

Two additional calculations may prove instructive. First, the simple Marangoni instability calculations of Pearson^{A-13} should be generalized to include a magnetic field. This would indicate the accuracy of the simple result of $B > 3300$ gauss given by Equation (A-12). Second, the effect of a magnetic field on a more realistic flow for float-zone silicon should be calculated. Hill's spherical vortex^{A-14} is one simple flow that could be used, since it appears similar to some of the computer-calculated flows for the float-zone geometry.^{A-4}

REFERENCES

- A-1 C.E. Chang and W.R. Wilcox, J. Crys. Growth, 28, 8-12 (1975).
- A-2 V.M. Glazov, S.N. Chizhevskaya, and N.N. Glazova, Liquid Semiconductors (Plenum Press, New York, 1969).
- A-3 J.D. Jackson, Classical Electrodynamics (Wiley, New York, 1962).
- A-4 Ch.-H. Chun, J. Crys. Growth, 48, 600-610 (1980).
- A-5 W. Keller and A. Muhlbauer, Floating-Zone Silicon (Dekker, New York, 1981).
- A-6 S. Chandrasekhar, Hydrodynamic and Hydromagnetic Stability (Oxford University Press, London, 1961).
- A-7 N. Kobayashi, Comp. Meth. in Appl. Mech. Eng. 23, 21-33 (1980).
- A-8 D. Schwabe and A. Scharmann, J. Crys. Growth, 46, 125-131 (1979).
- A-9 J.O. Hinze, Turbulence, (McGraw Hill, New York, 1975), p. 76.
- A-10 C.-H. Chun and W. Wuest, Act. Astronautics, 6, 1072-1082 (1979).
- A-11 N.G. Van Kampen and B.U. Felderhof, Theoretical Methods in Plasma Physics (North-Holland, Amsterdam, 1967).
- A-12 T.G. Cowling, Magnetohydrodynamics (Interscience, New York, 1957), pp. 56-76.
- A-13 J.R.A. Pearson, On convection cells induced by surface tensions, J. Fluid Mech. 4, 489-500 (1958).
- A-14 G.K. Batchelor, Fluid Dynamics (Cambridge University Press, London, 1970), p. 526.

APPENDIX B

DATA PROCESSING PROCEDURES

Introduction of computer-based data collection and processing techniques into the spreading resistance measurements has made possible a more quantitative and less subjective treatment of experimental results. In this appendix we will explain the terminology employed and the methods of analyzing the results of spreading resistance measurements on polished surfaces that are oriented parallel to the growth axis of the crystals.

A. DATA FILE DESIGNATIONS

Because several spreading resistance scans can be taken on one sample, we need a way of keeping track of each scan as well as the specimen from which it was obtained. The system adopted to identify each data record has proved workable although it is probably not the most efficient that could be generated. The principal deficiency that we see now is that there is not a good way for keying each individual scan to a specific region of the crystal without a carefully prepared map. Perhaps there is no alternative to the present system, but it has been inconvenient at times to have to consult a crystal map to correlate the spreading resistance data with a particular set of growth conditions. It would also be convenient if we could store and then recall files by selected criteria such as magnetic field strength, rotation rate, or growth rate. The best that we have been able to do so far is to identify the crystal, the type of scan, and the approximate position of the scan relative to the growth axis.

The scan identification method used in this report is arranged as follows: The file is identified as a spreading resistance file by the letters "SR." These are followed by the crystal number that was assigned by the grower. If the

spreading resistance data were obtained by the double probe method then the crystal number is followed by a "D"; and if by a single probe only, then by an "S." A further designation in the file name is used to identify a file from which all extraneous or incorrect points in the original data have been eliminated. These "bad" points often arise from dirt or scratches on the sample surface and if not excised from the data record would severely perturb the FFT analyses. To avoid such problems we have provisions in the computer program allowing removal of these bad points before beginning the FFT analysis. Thus, before each analysis, we generate a file of "original" data, free from bad points, to serve as the basis for all subsequent FFT analyses on that data set. A file reworked in this manner is indicated by a "P" in the file name. If the data file is the result of an FFT operation on a "P" file then the letter "F" is used to identify such files which are differentiated from each other by a number or letter assigned when they were generated. The sum of the above designations uses up the allotted spaces in the file name.

A three-character extension to the file name is available to indicate the direction and position of the scan relative to the growth axis. If the scan parallels the axis, then an "A" is used for the first character. If the scan is perpendicular to the axis and is thus in a radial direction, then an "R" is used. The second character of the extension designates the position on the sample for the axial scans. The designating letters are "C" for scans taken along the axis (center), "H" for those positioned half-way between the axis and the edge of the crystal, and "E" for scans near the edge. The numeral which follows the two letters in the extension is just the record of the sequence in which the scans were made. This sequence has meaning only to the operator of the spreading resistance apparatus who records this sequence in a notebook on a map of

the crystal for future reference. Typical file names are as follows:

SR285SF4.AE1. This file is the fourth FFT generated from data obtained with a single probe information about the scan and the growth conditions it covers must be obtained from records kept by the person making the scan.

SR292DP.AH3. This file contains the corrected original data taken with a double probe in the third axial scan of crystal Z292 at a position half-way between the axis and the edge. Further information must be obtained from log books.

B. GRAPHICAL PRESENTATION OF DATA

In the graphs shown throughout this report, the axes for the plots are those which are natural to the collection of the spreading resistance data and not necessarily those that would be chosen for analyzing the growth behavior. The abscissa in the original data plots is distance, in centimeters, and the ordinate is resistance as recorded by the spreading resistance probe. These units are retained for convenience when the FFT spectra are calculated even though we would prefer to have answers in the form of temporal frequencies rather than spatial frequencies. Conversion from reciprocal centimeters to reciprocal seconds is readily done using the specific growth rate for each crystal. The ordinate, expressed in the units "ohms times root centimeter per ohms average," is used primarily to indicate the fractional power per "frequency" interval, normalized by the average resistance, RAVG. The units themselves are not of any fundamental importance. The division by the average resistance of the data set provides a normalization which is convenient when comparing data from samples with differing resistivities.

The spatial resolution available from a data set is dependent upon the spacing of the original data points. We have worked with single probes at point spacings of 5, 10, and 20 μm

and double probes at 20 μm only. To work at the 5- μm spacing requires careful monitoring of the probe footprints and frequent reconditioning of the probe tips. At the 5- μm spacing, the data give a spatial frequency of 1000 reciprocal centimeters, which corresponds to a temporal frequency of 6.7 Hz at the usual growth rate of 4 mm/min (10 inches/hr). This appears to be the practical upper frequency limit for this method of fluctuation analysis.

C. PROCESSING OF SPREADING RESISTANCE DATA

With the aid of the computer we are able to perform several different operations on the data collected by the Solid State Measurements Inc. Model ASR 210 spreading resistance apparatus. The objective of these operations is to improve the interpretation of the data by providing quantitative measures of features which are associated with the crystal growth, but which may not be obvious in the raw data. The basic manipulation of the data is to use a Fourier transform to shift from the spatial to the frequency domain. In this manner one can identify temporal frequencies in which an unusual amount of power is concentrated. Such concentrations should be related to the dynamics of the crystallization process. For the clearly recognizable rotational frequencies (e.g., Figure 12), the FFT spectrum does not provide much additional insight. Its main value lies rather in the analysis of less obvious features, such as those presented in Figure 17.

In addition to the FFT analysis, the computer program will calculate the mean (arithmetic average) and standard deviation of any subset of data points in a file. We have found this feature of great value in identifying shifts in the doping level which are not always easily determined by visual inspection of the "noisy-looking" data. As yet we do not have a full appreciation of the origin and significance of the high

frequency fluctuations which seem always to be present. We expect that with more experience in working with such data we will gain better insights and appreciation for the information content of these spreading resistance files.

One of the obvious problems associated with the analysis of the FFT power spectral density plots is that there is always a noise-like component present that may mask the information being sought about flow-generated fluctuations in the melt. At this time we have no unique means to separate the "noise" from the "information." It may even be the case that the "noise" is the only information. However, to minimize the contribution to the FFT spectra of truly random events, we have adopted a method of averaging the spectra to reduce the impact of the random fluctuations.

For example, each of the curves plotted in Figure 17 has been generated by the following averaging process which has proved to be very useful. A region of spreading resistance data representing a constant growth condition is selected for an FFT operation; the resulting spectrum for this subset of data is stored in the computer. The number of points in the subset is some multiple of two, such as 128, 256, 512 or 1024, the size of the subset being dependent upon the size of the original data set. The computer then selects a new subset that has been shifted by a preselected number of points from the first subset and that contains the same number of points. Another FFT spectrum is taken and added to the first one. This operation is repeated as many times as is desired. The maximum number of spectra contributing to the average is limited by the size of the original data set. The individual FFT spectra thus obtained are then averaged by the computer to obtain an overall FFT spectrum which retains the frequency components characteristic of the data set and suppresses the random noise components. This method is referred to as a "SLiding average" and is

indicated by the letters "SL" in the file description. For example, file SR292SFJ.AE5 in Figure 17 has the description "SL 1,512,100,4" to indicate that the region contributing to the spectrum started at point 1 of the original data set, that 512 points were used in each FFT operation, that each successive subset of points was 100 points farther into the set than the previous subset, and that 4 such subsets contributed to the average. Thus the averaged spectrum started at point 1 and covered the original data out to point 812. In this fashion we have been able to treat a region with a point count that was not an exact multiple of two and have also reduced the influence of random (non-periodic) events.

If, on the other hand, the region of interest happens to be of such a size that an FFT operation on 512 or 1024 points is appropriate, we can then select that region out of the original data set for the generation of the FFT spectrum. In this case the descriptor is "SE" to indicate a SElected region for the operation. For example, in Figure 15, the dashed curve, file SR285SF7.AH1, starts on point 488 of the original data set and goes for the next 512 points. The "PO" indicates that the "POwer spectrum" operation was performed on this data subset. While this operation was often used early in our data processing, we have come to use the sliding average method much more frequently. It seems to give spectra that are not so cluttered with "spikes" and should thus improve our chances of detecting any frequencies characteristic of the melt behavior.

In the FFT treatment of the data we have the further option of selecting a "normal" window which truncates the data abruptly at the limits of the region chosen or we can employ a "hanning" window* which provides an apodization that reduces the amplitude of the data gracefully to zero at each end of the region selected for analysis. The hanning window reduces the high frequency components associated with the abrupt end truncations, but only does so at the sacrifice of some of the resolution given by the normal FFT spectrum. We have experimented with both methods on several different types of spreading resistance input data and have yet to see a clear-cut advantage of one method over the other. We expect to continue such comparisons in the future with any new types of data that may be collected. The data in Figures 15 and 17, as well as the other processed data in this report, are all obtained by the use of the normal window.

* The Measurement of Power Spectra, R. B. Blackman and J. W. Tukey, (Dover Publ. Inc., NY, 1959) p. 14.

END

FILMED

7-85

DTIC